analytical chemistry

ACS AUTHORCHOICE

pubs.acs.org/ac

Review

Chemical Analysis of Single Cells and Organelles

Keke Hu,[§] Tho D. K. Nguyen,[§] Stefania Rabasco,[§] Pieter E. Oomen,[§] and Andrew G. Ewing*

Cite This: *Anal. Chem.* 2021, 93, 41−71

Read Online

ACCESS | Metrics & More | Article Recommendations

CONTENTS

The chemical analysis of single cells and organelles is getting increased attention owing to their essential role in life science, clinical diagnostics, drug development, etc. Recent years have witnessed the emergence of innovative analytical methods with high sensitivity and spatial-temporal resolution that allowed qualitative and quantitative analysis to be carried out at single-cell and subcellular levels. This Review focuses on four major areas of analytical methods including electrochemical analysis, super-resolution microscopy, mass spectrometry imaging, and microfluidics. Each method has its own unique advantages, yet the increase in integration between them has enabled the achievement of both structural and functional information relating single cells and organelles. The development of new techniques, methods, and relevant applications in these fields during the last two years is summarized in this Review.

ELECTROCHEMICAL ANALYSIS OF SINGLE CELLS AND ORGANELLES

Developments of new techniques and various types of electrodes have offered the feasibility of electrochemical analysis at single-cell and single organelle levels with high sensitivity and selectivity. This section will cover the new applications mainly including single-cell amperometry (SCA), intracellular electrochemical analysis, vesicle impact electrochemical cytometry (VIEC), enzymatic biosensors, and electrochemiluminescence (ECL)-based systems for cell analysis.

Single-Cell Amperometry and Intracellular Electrochemical Analysis. SCA and intracellular VIEC (IVIEC) have been applied to measurements of different species at the

Special Issue: Fundamental and Applied Reviews in Analytical Chemistry 2021

Published: December 7, 2020

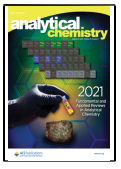

https://dx.doi.org/10.1021/acs.analchem.0c04361
Anal. Chem. 2021, 93, 41−71

single-cell level. Here, we will summarize recent developments of SCA and intracellular electrochemical analysis of neurotransmitters from endocrine cells and neurons, reactive oxygen and nitrogen species (ROS/RNS), and nicotinamide adenine dinucleotide (NADH).

Exocytosis is one of the most important processes for cell-to-cell communication in endocrine cells and neurons, the malfunction of which is implicated in neurodegenerative diseases and memory disorders. By positioning a micro/nano electrode adjacent to a cell surface, discrete exocytotic release events can be recorded, a technique termed single-cell amperometry (SCA) that allows quantification of the number of released molecules ($N_{molecules}$) and dynamic information on single cells.[1] With SCA, He and Ewing monitored the exocytosis of individual adrenal chromaffin cells triggered by stimulating the cells with a 30 s 30 mM K^+ solution including different counterions (i.e., Cl^-, Br^-, NO_3^-, ClO_4^-, or SCN^-).[2] They found that the exocytotic process was regulated by K^+ stimulation with different counterions in a manner that corresponds with the Hofmeister series, showing that the behavior of the membrane fusion pore during exocytosis is dependent on the counter-anions in solution. Gu et al. compared the measurement of exocytosis from single pheochromocytoma (PC12) cells between carbon fiber disk microelectrodes and nanotip conical-shape carbon fiber microelectrodes with SCA.[3] Spikes obtained with nanotip electrodes were slightly higher and narrower than those obtained with disk electrodes. The calculated pore−electrode distances for disk electrodes and nanotip electrodes are 239 and 215 nm, and the fusion pore sizes are 11.5 and 18.2 nm, respectively. These data showed that nanotip electrodes can be used to quantify molecules released during exocytosis and for quantitative comparison between exocytosis and vesicular content in IVIEC. Tang et al. used carbon fiber nanoelectrodes (CFNEs) to monitor exocytotic events occurring inside single dopaminergic synapses.[4] They showed that the natural product, harpagide, managed to enhance synaptic DA release and restore DA release at normal levels from injured neurons in a Parkinson's disease model by inhibiting ROS-induced phosphorylation and aggregation of α-synuclein.

IVIEC is another technique that enables quantification of vesicular content in the intracellular environment.[5] Roberts et al. combined carbon-fiber nanoelectrodes with fast-scan cyclic voltammetry (FSCV) to distinguish norepinephrine and epinephrine-containing vesicles inside chromaffin cells with IVIEC.[6] They found that a much higher amount of catecholamine was stored in vesicles containing epinephrine, and this offers the possibility to classify intracellular vesicles according to catecholamine content.

By combining SCA and IVIEC, the fraction of release can be calculated by dividing the amount of transmitters released from the vesicle over vesicular content. The effect of pharmaceutical treatment on the fraction of release has been studied by Ewing's group, offering new insights into regulatory mechanisms of neurotransmission and the formation of plasticity. Zhu et al. applied SCA and IVIEC to study the effects of cocaine and methylphenidate on exocytosis and the fraction of release.[7] They found that both drugs led to a decrease of vesicular catecholamine content and exocytotic catecholamine release but show opposite influences on the cognition and fraction of release, indicating that the fraction of release might be related to cognition. Taleat et al. evaluated the effects of nanomolar and micromolar concentrations of tamoxifen on exocytotic release and vesicle storage in cultured cells.[8] The data showed that high levels of tamoxifen triggered a significant decline of the amount of catecholamine released during exocytosis and the chemical content of the vesicles, while a low concentration of tamoxifen altered the $N_{molecules}$ during exocytosis in an opposite way, suggesting that tamoxifen treatment regulates exocytosis differentially at low and high concentrations. As the main energy source for cellular metabolism, ATP is also released with other transmitters during exocytosis. Majdi et al. studied the effects of ATP on catecholamine release and vesicular storage in chromaffin cells with SCA and IVIEC.[9] They found that the fraction of the catecholamine release increased with extracellular ATP. Further study indicated that the vesicular catecholamine content increased after treating cells and vesicles with suramin (a purinergic blocker) and ARL-67156 (an antagonist of ecto-ATPases) that inhibited ATP related enzymes and receptors. These results suggested that ATP is likely to modulate neurotransmission by the presynaptic regulation of the strength of partial fusion. Gu et al. combined electrochemical techniques with calcium imaging to investigate the effect of short-interval repetitive stimuli on both exocytosis and vesicular content in a model cell line.[10] They showed that the number of events and vesicular content decreases with repeated stimuli while the amount of neurotransmitter released increases. The resultant higher fraction of release suggested a possible connection between activity-induced plasticity and the fraction of release. Larsson et al. uncovered the partial release of vesicular octopamine from living *Drosophila* larval neuromuscular neuron.[11] The partial release in this neuronal system suggested the possibility that cells could adjust the chemical signaling via an open and closed fusion pore. These studies with SCA and IVIEC further confirmed the correlation between the fraction of transmitter release and plasticity regulation, deepening the understanding of initial plastic changes in learning and promoting drug development for diseases related to early plasticity.

Using SCA and IVIEC, Yue et al. investigated the effect of DJ-1 protein deficiency on vesicular transmitter storage and release during exocytosis.[12] The DJ-1 protein deficiency caused by PARK7 gene knockout in mice has no obvious effect on vesicular catecholamine content but significantly increases the duration of exocytotic events, especially the closing time of the fusion pore. Further studies suggested that DJ-1 protein might inhibit α-synuclein aggregation to regulate neurotransmission. This finding has uncovered a direct correlation between DJ-1 protein deficiency and vesicular chemical storage and release.

Reactive oxygen and nitrogen species (ROS/RNS) play a critical role in numerous life processes. These species can work together or independently to participate in physiological regulation including host immunity, cell signaling, redox regulation, etc. Electrochemistry offers a direct and label-free approach to detect the electroactive ROS/RNS. The development of small probes and new methodologies has pushed the limit of electrochemical measurement of ROS/RNS from single living cells to single organelles and vesicles.[13]

Hu et al. investigated the real-time dynamics of main ROS/RNS (including $NO^{\bullet}$, H_2O_2, $ONOO^-$, and NO_2^-) produced by large phagolysosomes inside IFN-γ/LPS-stimulated RAW 264.7 macrophages using a four-step chronoamperometric method with small platinized carbon nanoelectrodes.[14] The production rate of the four primary ROS/RNS in the individual phagolysosomes that were monitored was highly

https://dx.doi.org/10.1021/acs.analchem.0c04361
Anal. Chem. 2021, 93, 41−71

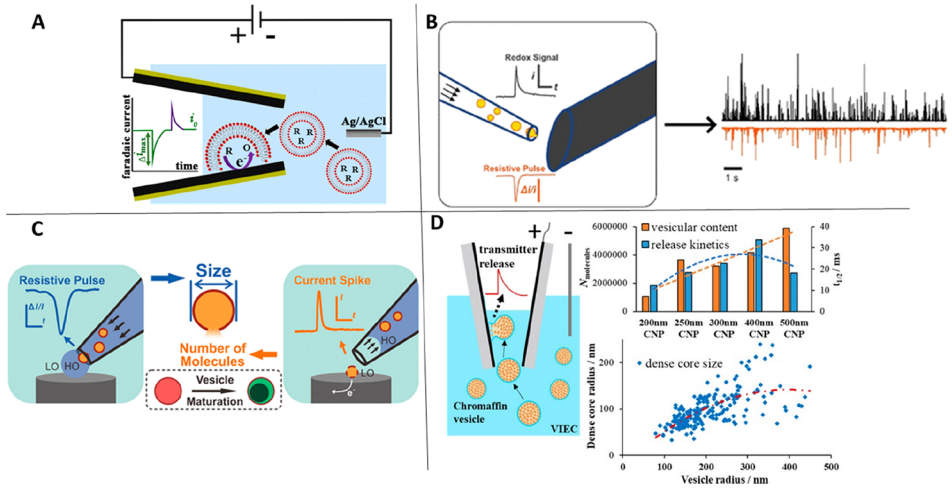

Figure 1. Different methods of VIEC measurements. (A) Schematic of "Electrochemical resistive-pulse sensing" with open CNPs to monitor both the translocation of the liposomes and the release of loaded dopamine. Reproduced from Pan, R.; Hu, K.; Jiang, D.; Samuni, U.; Mirkin, M. V. Electrochemical Resistive-Pulse Sensing. *J. Am. Chem. Soc.* **2019**, *141* (50), 19555−19559 (ref 27). Copyright 2019 American Chemical Society. (B) Schematic of resistive-pulse analysis at a nanopipette coupled with VIEC at a CFE close to the nanopipette orifice and representative amperometric traces. Reproduced from Barlow, S. T.; Zhang, B. Fast Detection of Single Liposomes Using a Combined Nanopore Microelectrode Sensor. *Anal. Chem.* **2020**, *92* (16), 11318−11324 (ref 28). Copyright 2020 American Chemical Society. (C) Schematic of the single vesicular catecholamine concentration measurement based on one-to-one matching of resistive pulse spikes with catecholamine release spikes of single chromaffin vesicles. Reproduced from Zhang, X. W.; Hatamie, A.; Ewing, A. G. Simultaneous Quantification of Vesicle Size and Catecholamine Content by Resistive Pulses in Nanopores and Vesicle Impact Electrochemical Cytometry. *J. Am. Chem. Soc.* **2020**, *142* (9), 4093−4097 (ref 29). https://pubs.acs.org/doi/10.1021/jacs.9b13221. Copyright 2020 American Chemical Society. (D) Schematic of VIEC with different-sized open CNPs, correlation of vesicular content and release kinetics with vesicle size, and TEM data on vesicle dimensions. Reproduced from Hu, K.; Jia, R.; Hatamie, A.; Long, K. L. V.; Mirkin, M. V.; Ewing, A. G. Correlating Molecule Count and Release Kinetics with Vesicular Size Using Open Carbon Nanopipettes. *J. Am. Chem. Soc.* **2020**, *142* (40), 16910−16914 (ref 30). https://pubs.acs.org/doi/10.1021/jacs.0c07169. Copyright 2020 American Chemical Society.

variable, indicating that the continuous production of ROS/RNS was stimulated by their rapid oxidation at the nanoelectrode tip to maintain sufficiently high ROS/RNS levels inside the phagolysosome. Later, Zhang et al. measured ROS/RNS effluxes from individual phagolysosomes with IVIEC at platinized nanowire electrodes (Pt-NWEs) with submillisecond resolution.[15] Both works confirmed the existence of ROS/RNS homeostasis and helped to unravel the complexity of phagocytosis. Pan et al. carried out electrochemical resistive-pulse experiments inside a RAW 264.7 macrophage cell with platinized open carbon nanopipettes (CNPs) to sample single vesicles and measure ROS/RNS contained inside them.[16] Wang et al. monitored ROS levels with platinum modified SiC@C NWEs during the in situ biosynthesis of ZnO quantum dots at single cancer cells.[17] Vaneev et al. recorded anticancer drug-induced ROS production inside a single cell using a platinized nanoelectrode with high sensitivity.[18] This method is available to measure ROS levels during chemotherapy in tumor-bearing mice in real time.

Other ROS at the single-cell or subcellular level were detected independently on the basis of Faradaic current or ionic current. Zhou et al. employed a single-atom catalyst (SAC)-based electrochemical sensor to detect NO in the live cellular environment.[19] Single nickel atoms anchored on N-doped hollow carbon spheres (Ni SAC/N−C) showed excellent electrocatalytic effects toward oxidation of NO released from endothelial cells. Ding et al. measured •OH at the subcellular level using 1-hexanethiol (HAT) modified tungsten nanoelectrodes.[20] The •OH level in Aβ1−40-treated RAW 264.7 murine macrophages (AD model cells) and the pharmacological effects of cordycepin on •OH generation were investigated. The results demonstrated that the cordycepin-mediated cytoprotection of macrophages was achieved through the regulation of the PI3K/Akt pathway activity and the introduction of heme oxygenase-1 (HO-1). H_2O_2 in the axon of a single neuron was measured with resistive analysis on the basis of acrylic acid polymerization in nanopipettes.[21] H_2O_2 was electrokinetically loaded into the pipette and reacted with ferrous ions to generate hydroperoxyl radicals that initiate the polymerization of acrylic acid. Capillary resistance decreased due to the polymerization of acrylic acid; then, the distribution of H_2O_2 in the axon was quantified by analyzing ionic current. Chen et al. coated a Au film onto the nanopipette inner wall followed by modification with HAT to form Au−S bonds to detect •OH around the mitochondria based on ionic current rectification.[22]

Glass nanopipette-based nanoITIES (interface between two immiscible electrolyte solutions) and nanopore electrodes were employed for electrochemical analysis of acetylcholine and NADH at single cells, respectively. Shen et al. demonstrated the in situ simultaneous measurements of the synaptic cholinergic transmitter concentration and release dynamics with nanoITIES electrodes and scanning electrochemical microscopy (SECM).[23] Ying et al. developed wireless asymmetric nanopore electrodes to detect redox metabolism in living cells.[24] They measured NADH concentrations as low as 1 pM, and this type of nanopore electrode is available to monitor real-time NADH in a living cell. By modifying conductive polymer (poly(3,4-ethylendioxythiophene), PEDOT)-coated carbon nanotubes (CNTs) onto a SiC@C nanowire surface, Jiang et al. selectively measured NADH released from mitochondria in single living cells.[25]

https://dx.doi.org/10.1021/acs.analchem.0c04361
Anal. Chem. 2021, 93, 41−71

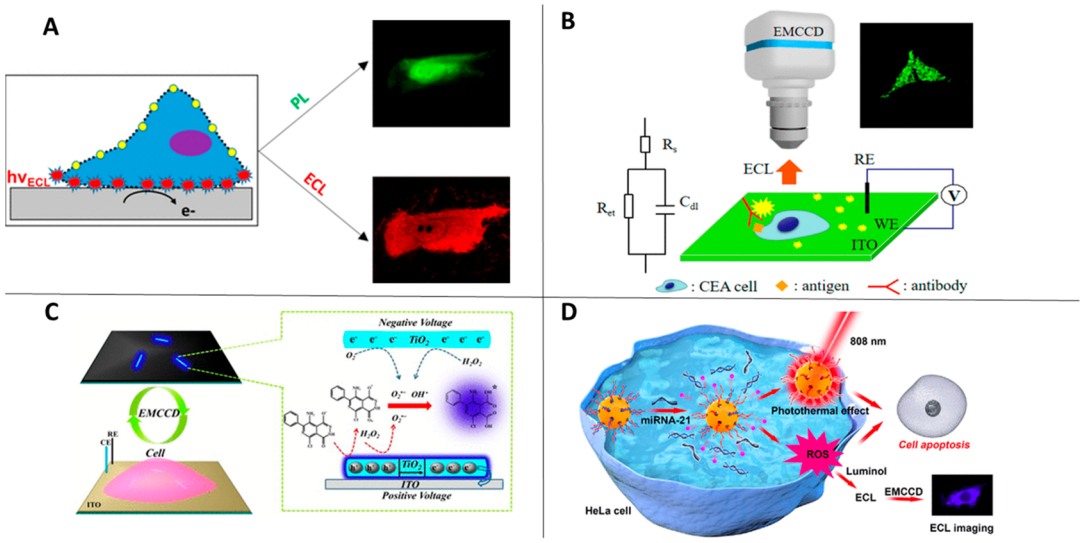

Figure 2. Electrochemiluminescence-based systems for cell analysis. (A) Schematic of the ECL imaging of the plasma membrane of single cells and representative images obtained with ECL and photoluminescence. Reproduced from Voci, S.; Goudeau, B.; Valenti, G.; Lesch, A.; Jović, M.; Rapino, S.; Paolucci, F.; Arbault, S.; Sojic, N. Surface-Confined Electrochemiluminescence Microscopy of Cell Membranes. *J. Am. Chem. Soc.* **2018**, *140* (44), 14753−14760 (ref 36). Copyright 2018 American Chemical Society. (B) Schematic of ECL-based capacitance microscopy to image the antigens on the cells. Reproduced from Zhang, J.; Jin, R.; Jiang, D.; Chen, H. Y. Electrochemiluminescence-Based Capacitance Microscopy for Label-Free Imaging of Antigens on the Cellular Plasma Membrane. *J. Am. Chem. Soc.* **2019**, *141* (26), 10294−10299 (ref 38). Copyright 2019 American Chemical Society. (C) Schematic of steady-state ECL at single semiconductive TiO_2 nanoparticles for sensing local H_2O_2 efflux from single living cells. Reproduced from Cui, C.; Chen, Y.; Jiang, D.; Chen, H. Y.; Zhang, J.; Zhu, J. J. Steady-State Electrochemiluminescence at Single Semiconductive Titanium Dioxide Nanoparticles for Local Sensing of Single Cells. *Anal. Chem.* **2019**, *91* (1), 1121−1125 (ref 40). Copyright 2019 American Chemical Society. (D) Schematic of the ECL detection of intracellular miRNA. ROS were released after miRNA recognition and visualized using luminol at the fluorine-doped tin oxide (FTO) electrode. Reproduced from Zhang, H.; Gao, W.; Liu, Y.; Sun, Y.; Jiang, Y.; Zhang, S. Electrochemiluminescence-Microscopy for MicroRNA Imaging in Single Cancer Cell Combined with Chemotherapy-Photothermal Therapy. *Anal. Chem.* **2019**, *91* (19), 12581−12586 (ref 43). Copyright 2019 American Chemical Society.

Vesicle Impact Electrochemical Cytometry. VIEC measurements have the advantage of eliminating interferences from other cellular organelles since vesicles are isolated from the cells or glands before measurement, which is beneficial for studies of the pharmaceutical effect on vesicle opening and rupture.[26] VIEC can also be used to quantify the number of neurotransmitters originally stored inside single vesicles. In the last two years, the applications of new methodologies have promoted VIEC studies to be transformed from mechanisms regarding vesicle opening and rupture to the correlation of molecule count and release dynamics with vesicular structure.

Using liposomes as a model system, Pan et al. carried out electrochemical resistive-pulse sensing to monitor both translocation of the liposomes and release of the loaded dopamine with open CNPs (Figure 1A).[27] Barlow and Zhang coupled resistive-pulse analysis at the nanopipette with a VIEC measurement at the carbon-fiber microelectrode (CFE) close to the nanopipette orifice to simultaneously collect the ionic current related to liposome size and redox signal of the loaded $Fe(CN)_6^{4-}$ released from the single liposomes (Figure 1B).[28] They showed that the leakage of the liposome contents occurred during translocation. Liposome disruption was shown to be regulated by the velocity of fluid flow in the nanopore and the nanopore geometry. With a similar method, Zhang et al. achieved one-to-one matching of resistive pulse spikes with catecholamine release spikes of single chromaffin vesicles (Figure 1C).[29] On the basis of this, single vesicular catecholamine concentrations were quantified, and a comparison between dense core vesicles and nondense core vesicles provided quantitative information about the vesicle maturation process. Very recently, Hu et al. controlled orifice sizes of open CNPs to group different sized vesicles and quantified the corresponding vesicular content and release kinetics (Figure 1D).[30] They showed that the vesicular content increases with vesicle size, and the vesicular release dynamics is limited by the vesicular dense core size. Also, small-size open CNPs are available for both sizing and counting molecules for vesicles in a living cell.

Enzymatic Biosensors. Enzymatic biosensors are applicable in measurements of both electroactive and nonelectroactive analytes with high specificity. Marquitan et al. built an electrochemical nanometer-sized sensor modified with a polymer/enzyme multilayer for glutamate (Glu) detection at the single-cell level.[31] Carbon nanoelectrodes were functionalized with an electroactive redox polymer/horseradish peroxidase (HRP) film, and on top of that was an ad hoc synthesized redox silent hydrophilic polymer matrix immobilized with Glu oxidase (GluOx). The oxidation of the analyte in the presence of O_2 produced H_2O_2 that would be reduced to water by HRP, and electrons were shuttled via the redox polymer matrix that wires the HRP to the electrode surface; thus, a current response proportional to the glutamate concentration was recorded. The Glu released from primary mouse astrocytes was detected by positioning the sensor in close proximity to the adherent cells. Yang et al. fabricated a Glu electrochemical biosensor and monitored the release of Glu under the effect of Aβ peptides.[32] They found that short-term incubation (30 min) of Aβ1−42 oligomers significantly enhanced the release of Glu followed by dramatic depletion after 300 min of treatment. Further study demonstrated that the vesicular Glu transporter 1 (VGLUT1) that is responsible for the transport of Glu into the synaptic vesicles displayed a

https://dx.doi.org/10.1021/acs.analchem.0c04361
Anal. Chem. 2021, 93, 41−71

similar trend, implying that VGLUT1 is closely related to the Aβ1−42-induced abnormalities in the Glu release. Wang et al. developed a gold nanoparticle (AuNP)-modified carbon fiber microelectrode with an ultrathin coating of GluOx to quantify glutamate molecules loaded inside single isolated synaptic vesicles.[33] They compared the release to the vesicle content and suggested a fractional release.

Marquitan et al. modified redox polymer/enzyme film onto HF etched carbon-based nanoelectrodes to detect glucose at the single-cell level.[34] The redox polymer matrix was synthesized by modifying a poly(1-vinylimidazole-*co*-acrylamide)-based backbone with the electron transfer mediator $[Os(bpy)_2Cl]^+$ (bpy = 2,20-bipyridine) followed by a polymer−analogue reaction that converted the amide groups within the acrylamide monomer into hydrazide groups. The hydrazide groups reacted readily with bifunctional epoxide-based cross-linkers premodified on the carbon surface. Glucose oxidase (GOx) was immobilized and electrically wired via the redox polymer in a sequential dip coating process. The nanometer-size polymer/enzyme modified electrodes were used to penetrate into single living NG108-15 cells, resulting in a positive and stable current response that correlated with the intracellular glucose concentration. Liao et al. fabricated a single nanowire glucose sensor by depositing Pt nanoparticles (Pt NPs) onto SiC@C nanowires followed by the immobilization of GOx for electrochemical detection of intracellular glucose.[35] Glucose was converted by GOx to H_2O_2 that was further oxidized by Pt NPs catalysis. This glucose nanowire sensor showed high sensitivity and spatial-temporal resolution.

Electrochemiluminescence-Based Systems for Cell Analysis. ECL-based sensing combines electrochemical and spectroscopic methods. In this part, the recent developments of the ECL-based system in the cell membrane imaging and the direct detection of extracellular and intracellular molecules will be introduced.

Voci et al. reported a surface-confined microscopy method based on electrochemiluminescence (ECL) that allowed imaging of the plasma membrane of single cells at the interface with an electrode (Figure 2A).[36] Compared with the classic wide-field fluorescence microscopy, they showed that the ECL emission was limited to the immediate vicinity of the electrode surface and only the basal membrane of the cell became luminescent. They obtained images with details that were not resolved by classic fluorescence microscopy. This is a dynamic technique that can provide information on transport properties through the cell membranes besides the specific labeling area. Liu et al. developed a potential-resolved ECL method and used it for the apoptosis diagnosis at the single-cell level.[37] In this research, Au@L012 and g-C3N4 as ECL probes were modified with epidermal growth factor (EGF) and peptide (PSBP) to recognize the epidermal growth factor receptor (EGFR) and phosphatidylserine (PS), respectively, on cell surfaces that correlate with the degree of cell apoptosis. With two well-separated ECL signals, this approach provided an accurate way to investigate apoptosis without interference that solely changes EGFR or PS. Zhang et al. established a method called ECL-based capacitance microscopy using a square wave voltage to carry out the label-free visualization of species on the electrode surfaces and cellular plasma membranes (Figure 2B).[38] The specific capacitance (Cs) in the region of the surface that bound nonconductive biospecies decreased, resulting in a relatively higher potential drop across the double layer (V_{dl}) in this region. Higher V_{dl} values in the binding regions induced brighter luminescence, which was distinguishable from the surrounding surface. In this way, the binding of species in those areas can be identified directly by the visualization of brighter ECL spots on the surface. In another work, Li et al. evaluated the fluctuation of cholesterol in plasma membrane at single cells during testosterone treatment using luminol ECL.[39]

ECL-based imaging was also employed for the visualization of H_2O_2 released from single living cells. Cui et al. obtained steady-state bright ECL at single semiconductive titanium dioxide (TiO_2) nanoparticles for sensing of local H_2O_2 efflux from single living cells (Figure 2C).[40] The steady-state adsorption of H_2O_2 due to the high affinity of oxygen vacancies on the surface of rutile TiO_2 nanoparticles facilitated the continuous electrochemical generation of superoxide (O_2^-) and $^{\bullet}OH$ by electrons and surface-trapped holes at the nanoparticles, resulting in constant ECL under physiological conditions. H_2O_2 efflux from single cells can be visualized through the steady-state luminescence correlated with the concentration of H_2O_2. Using the confined ECL of luminol, Zhang et al. detected the H_2O_2 ion in vertically ordered silica mesochannels (SMCs) and applied it into H_2O_2 efflux imaging from single living cells with high sensitivity and a detection range between 5 μM and 1 mM.[41] Chen et al. synthesized nitrogen doped hydrazide conjugated carbon dots (NHCDs) with strong anodic ECL at a low excitation potential and applied it into rapid cancer cell detection.[42] The doped nitrogen induced a shift of the highest occupied molecular orbital (HOMO) to the upper energy level, and the anodic ECL excitation potential of carbon dots was lowered. A 2.5-fold high ECL quantum efficiency was achieved compared with nondoped quantum dots. On the basis of this, a brief ECL biosensor was fabricated to detect cell-secreted H_2O_2, which could rapidly distinguish cancer cells from normal cells.

Intracellular molecules have been detected with ECL-based sensors with high sensitivity. Zhang et al. built a new technology using ECL as a form of microscopy to obtain parallel images of miRNA-21 in single cancer cells (Figure 2D).[43] In this scheme, phorbol-12-myristate-13-acetate (PMA) and DNA loaded gold nanocages that can recognize miRNA-21 were employed as a probe. Upon recognition of miRNA-21, PMA was released inside the cells that induced the production of ROS and was visualized by ECL imaging. This probe can also be applied in chemotherapy and photothermal therapy. Wang et al. achieved intracellular wireless electroanalysis by using a Pt-deposited nanopipette tip as an open bipolar ECL device.[44] Pt deposited inside the nanopipette transported intracellular molecules into the nanopipette that was coupled to enzymatic reactions. This approach restricted the extremely low potential inside the nanopipette, and it minimized the bias potential on the cellular activity. In addition, Xia et al. prepared a gold-coated polydimethylsiloxane (PDMS) chip with cell-sized microwells through a stamping and spraying process and applied it to the high-throughput ECL analysis of intracellular glucose at single cells.[45]

SUPER-RESOLUTION MICROSCOPY FOR IMAGING OF SINGLE CELLS AND ORGANELLES

Latest Advances in Super-Resolution Microscopy Techniques. The diffraction limit is classically considered the barrier that restricts optical resolution; however, since the rapid development of super-resolution microscopy (SRM), considerably smaller resolution can be obtained. Currently, a

https://dx.doi.org/10.1021/acs.analchem.0c04361
Anal. Chem. 2021, 93, 41−71

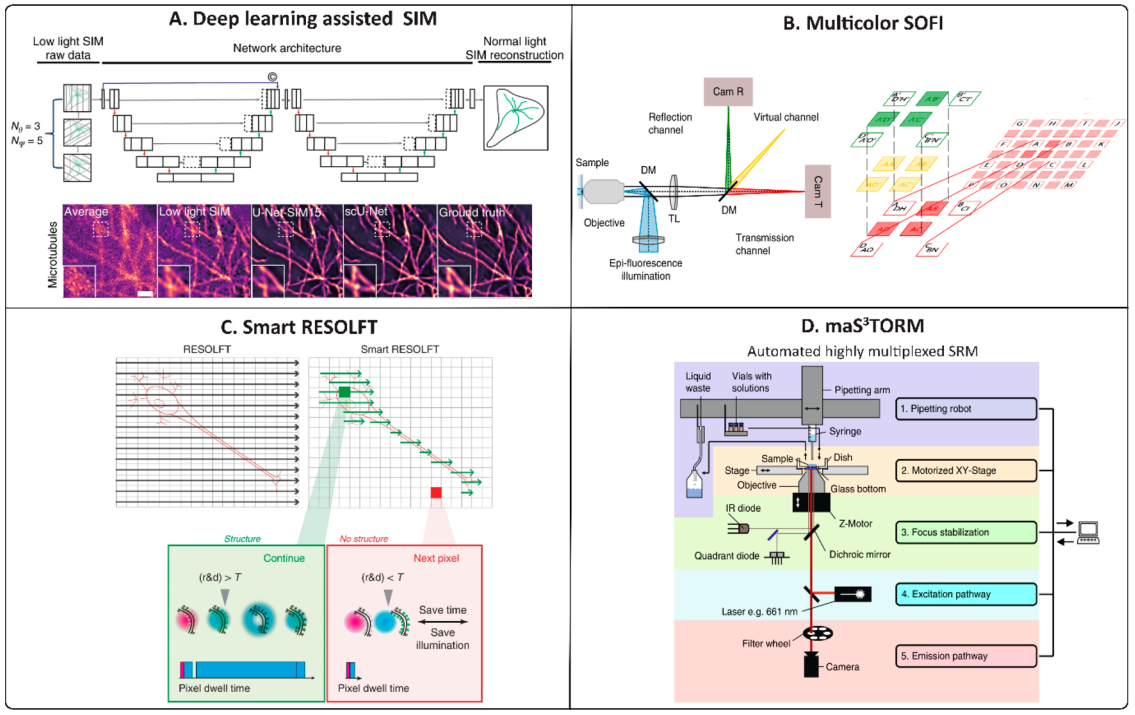

Figure 3. Principles of some new improvements of SRM techniques. (A) Deep learning assisted SIM. Fifteen or three SIM raw data images were used as input, and the corresponding SIM reconstructions from 15 images were used as the ground truth to train the U-Net. θ: the angle of the sinusoidal patterned illumination; ψ: the phase of the patterned illumination. Reconstruction results for microtubules (lower panel). (B) Multicolor SOFI, cross-cumulant analysis between spectral channels. (C) Raster (left) compared to smart (right) scanning, which is specimen-adaptive. The feedback loop and smart pixel technologies enable one to perform RESOLFT imaging only in regions of the specimen containing labeled structures. The decision in smart RESOLFT (red and green boxes) is in intrapixels and threshold-based. (D) Automated maS^{3}TORM multiplex setup and experimental workflow. Panel A is reproduced from Jin, L.; Liu, B.; Zhao, F.; et al. *Nature Communications* **2020**, *11*, 1934 (ref 46). Panel B is reproduced from Grußmayer, K. S.; Geissbuehler, S.; Descloux, A.; et al. *Nature Communications* **2020**, *11*, 3023 (ref 47). Panel C is reproduced from Dreier, J.; Castello, M.; Coceano, G.; et al. *Nature Communications* **2019**, *10*, 556 (ref 48). Panel D is reproduced from Klevanski, M.; Herrmannsdoerfer, F.; Sass, S.; et al. *Nature Communications* **2020**, *11*, 1552 (ref 49). Panels A–D are reproduced under a Creative Commons 4.0 International License (http://creativecommons.org/licenses/by/4.0/).

broad range of SRM techniques is available, which can be categorized into two major groups that (i) improve the spatial resolution by few factors; (ii) break the resolution barrier (diffraction unlimited). The first group includes several techniques such as expansion microscopy (ExM), image scanning microscopy (ISM), structured illumination microscopy (SIM), and super-resolution optical fluctuation imaging (SOFI). The second group includes coordinate-targeted-based SRM such as stimulated emission depletion microscopy (STED) and reversible saturable optical linear fluorescence transitions (RESOLFT); single-molecule localization-based SRM (SMLM) such as stochastic optical reconstruction microscopy (STORM), photoactivated localization microscopy (PALM), and points accumulation for imaging in nanoscale topography (PAINT); finally, coordinate-targeted single-molecule localization-based SRM MINFLUX (minimal emission fluxes). An overview of the recent advances in SRM techniques is given in Figure 3 and discussed more throughout. The SRM techniques shown in Figure 3 include deep learning assisted SIM (Figure 3A),[46] multicolor SOFI (Figure 3B),[47] raster (Figure 3C, left) compared to smart (Figure 3C, right) scanning,[48] and automated maS^{3}TORM multiplexing (Figure 3D).[49]

These SRM techniques, with different working principles, have their own pros and cons as well as requirements for probes, hardware, and/or software supports. However, they all aim to the ultimate goal of promoting new discoveries, revealing *"the tiny world"* with high-quality and reliable images. Several recent reviews have discussed super-resolution microscopy with different focuses.[50−53] Herein, we limited ourselves to summarizing the latest developments of these SRM techniques over the last two years to achieve even better resolution and localization precision, faster imaging speed, multicolor/multiplex imaging, and better live-cell compatibility. Figure 4 provides examples of the super-resolved architecture of cellular compartments that can be revealed by super-resolution microscopy. These examples are discussed throughout this section and include images of a subset of microtubules around the mother centriole in human retinal pigment epithelial cells (Figure 4A), dSTORM images of an axial view of centrioles showing the radial distribution of various critical proteins that were not resolvable with wide-field (WF) imaging (Figure 4B),[54] time-lapse STED imaging of mitochondrial dynamics in cells (Figure 4C),[55] representative dSTORM images of chemically fixed HeLa cells expressing vimentinBC2T (Figure 4D, right)[56] and WF/dSTORM images with intracellular live-cell labeling and imaging of clickable microtubule-associated protein (EMTB) in COS-7 cells (Figure 4D, left),[57] rapid time-lapse imaging of peroxisomes with smart RESOLFT (Figure 4E),[48] dendritic and axonal profiles with MemBright (blue) to visualize glutamate AMPA receptor clusters (green) aggregated at the dendrite in front of the axonal profile with an interleaved 3D STORM stack (Figure 4F),[58] a DNA-PAINT image of NUP96-SNAP in

https://dx.doi.org/10.1021/acs.analchem.0c04361
Anal. Chem. 2021, 93, 41−71

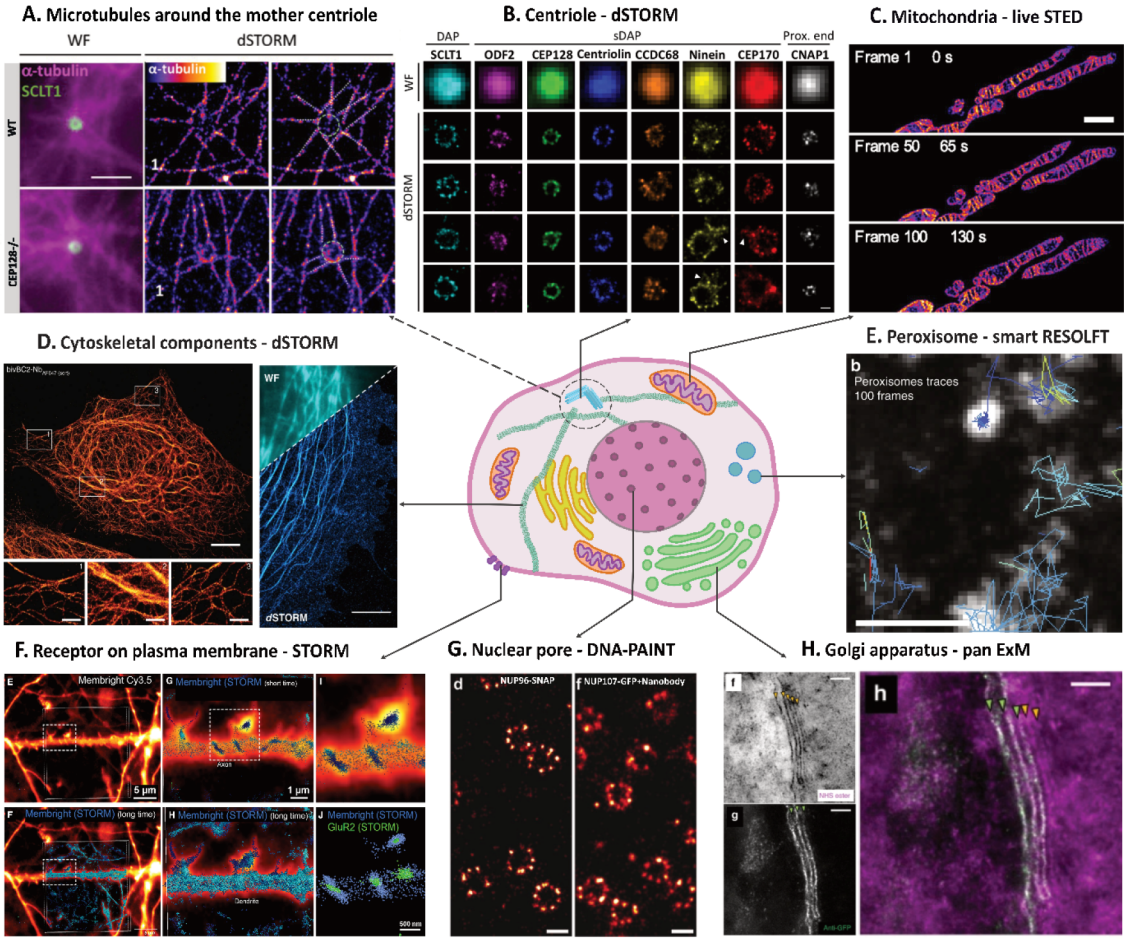

Figure 4. Revealing the super-resolved architecture of cellular compartments by super-resolution microscopy. (A) A subset of microtubules around the mother centriole in human retinal pigment epithelial cells (RPE-1); dSTORM images revealing fewer α-tubulin fibers arranged around the CEP128 −/− centriole (white dotted line) as compared to the WT centriole. Scale bar: 2 μm. (B) Centriole−dSTORM, images of axial-view centrioles showing the radial distribution of the distal appendage (DAP) protein SCLT1, various sDAP proteins, and the centriole proximal-end (Prox. end) protein CNAP1, which were not resolvable under wide-field (WF) imaging. Scale bar: 200 nm. (C) Time-lapse STED imaging of mitochondrial dynamics in MitoPB Yellow-labeled cells. Three frames are presented. Huygens deconvolution. Scale bar: 2 μm. (D) Right part: Representative dSTORM images of chemically fixed HeLa cells expressing vimentinBC2T, stained with the sortase-coupled bivBC2-NbAF647 (sort). Scale bars: main image, 5 μm; insets, 1 μm; Left part: WF/dSTORM images with intracellular live-cell labeling and imaging of clickable microtubule-associated protein (EMTB) in COS-7 cells; cells were fixed and labeled with 3 μM H-Tet-HMSiR. Scale bar: 5 μm. (E) Rapid time-lapse imaging of peroxisomes with smart RESOLFT, over 100 time points recorded at 2−5 Hz. Maximum projection of the entire 100 frames time-lapse is shown. Pex16-rsEGFP2 was expressed in U2OS cells. Scale bar: 1 μm. (F) Dendritic and axonal profiles; MemBright (blue) used to visualize glutamate AMPA receptor clusters (green) aggregated at the dendrite in front of the axonal profile with an interleaved 3D STORM stack. Scale bars: 5 μm, 1 μm, and 500 nm, respectively. (G) DNA-PAINT image of NUP96-SNAP in U2OS cells (left) and NUP107-GFP in HeLa cells (right) reveal the nuclear pore complexes. Scale bars: 100 nm. (H) Images of Golgi apparatus achieved by pan ExM/STED; inset (f) shows an NHS ester pan-stained Golgi stack in a ManII-GFP expressing HeLa cell. The yellow arrowheads show five distinct Golgi cisternae; inset (g) shows an Anti-GFP STED image of the same area; inset (h) is the overlay. Scale bar: 250 nm. Panels A and B are reproduced from Chong, W. M.; Wang, W. J.; Lo, C. H.; et al. *eLife* **2020**, *9*, 1−21 (ref 54). Panel C is reproduced and adapted with permission from Proceedings of the National Academy of Sciences; Wang, C.; Taki, M.; Sato, Y.; et al. *J. Proc. Natl. Acad. Sci. U.S.A.* **2019**, *116* (32), 15817−15822 (ref 55). Panel D, right part, is reproduced from Virant, D.; Traenkle, B.; Maier, J.; et al. *Nature Communications* **2018**, *9* (1), 1−14 (ref 56); left part, is reproduced from Beliu, G.; Kurz, A. J.; Kuhlemann, A. C.; et al. *Communications Biology* **2019**, *2* (1), 261 (ref 57). Panel E is reproduced from Dreier, J.; Castello, M.; Coceano, G.; et al. *Nature Communications* **2019**, *10*, 556 (ref 48). Panel F is reproduced and adapted from *Cell Chemical Biology*, *26* (4), Collot, M.; Ashokkumar, P.; Anton, H.; et al. MemBright: A Family of Fluorescent Membrane Probes for Advanced Cellular Imaging and Neuroscience. pp 600−614 (ref 58). Copyright 2019, with permission from Elsevier. Panel G is reproduced and adapted from Direct Visualization of Single Nuclear Pore Complex Proteins Using Genetically-Encoded Probes for DNA-PAINT, Schlichthaerle, T.; Strauss, M. T.; Schueder, F.; et al. *Angew. Chem. Int. Ed. Engl.*, Vol. *58*, Issue 37 (ref 59). Copyright 2019 Wiley. Panel H is reproduced and adapted from M'Saad, O.; Bewersdorf, J. *Nature Communications* **2020** *11* (1), 1−15 (ref 60). Panels A, B, D, E, G, and H are reproduced and adapted under a Creative Commons 4.0 International License (http://creativecommons.org/licenses/by/4.0/).

U2OS cells (Figure 4G, left) and NUP107-GFP in HeLa cells (Figure 4G, right) revealing the nuclear pore complexes,[59] and images of the Golgi apparatus with panExM/STED (Figure 4H).[60]

Extended Resolution SRM. Expansion microscopy (ExM)[61] tackles the resolution limit by a simple approach, sample physical expansion, without requiring a complex microscope system. Recently, ExM performance has been improved in many of its new variants; for instance, magnified analysis of the

https://dx.doi.org/10.1021/acs.analchem.0c04361
Anal. Chem. 2021, 93, 41−71

proteome (MAP) and ultrastructure-ExM (U-ExM) achieves an expansion factor of ∼4 in all three dimensions. These protocols were also carefully optimized to reduce cellular content degradation and allow isotropic expansion without inter- and intraprotein cross-linking. Gambarotto et al. presented a protocol of U-ExM combined with STED microscopy to resolve the centriolar chirality.[62] In this protocol, a postexpansion labeling approach provided a smaller distance from the fluorophore to the epitope, which is usually unchanged in conventional ExM, benefiting the combined technique, STED.

Moreover, recently, M'Saad and Bewersdorf presented pan-ExM, a new principle, to further improve the expansion factor.[60] The authors utilized the concept of semi-interpenetrating polymer networks (semi-IPN) to develop polymer−protein hybrids. First, the cell is prepared in dense hydrogels with cleavable cross-linkers. Later, this sample is embedded in another dense superabsorbent hydrogel. The interactions of the polymer chains between the different hydrogels physically interlock the protein−polymer mixtures, preserving the proteome while achieving a linear expansion factor of ∼16 (Figure 4H), comparable with iterative-ExM (iExM).[63] Despite the effort to improve resolution, the application of ExM is still restricted to only fixed-cell imaging due to its design.

Image scanning microscopy (ISM) is another simple approach that doubles the spatial resolution of standard confocal microscopes.[64] In ISM, a small array of detectors is used instead of a point detector to generate an array of images. Each image is used as a pixel for reconstruction via computer-based pixel-reassignment to achieve a sharper image. This allows resolution enhancement without reducing the signal level. Tenne et al. advanced this technique by introducing quantum-ISM (Q-ISM), combining ISM with quantum photon correlation measurement, enhancing the resolution ∼4 times over the diffraction limit.[65] In Q-ISM, using photon correlations, each pair of detectors in a detector array generates a sharp image; later, the images are merged. On the basis of a quantum optical effect called photon antibunching, super-resolved images can be obtained. The authors demonstrated Q-ISM use for biological samples by imaging fluorescent quantum dot labeled microtubules in 3T3 cells.

Traditionally, structured illumination microscopy (SIM) employs frequency shifting upon patterned illumination and mathematical reconstruction to bypass the lateral resolution limit.[66] Later, a variant of SIM, 3D-SIM, was shown to provide optical sectioning doubling both lateral and axial resolution.[67,68] Nevertheless, the z-resolution is still poorer than the x,y-resolution of wide-field microscopy. Thus, Manton et al. presented a new approach to enhance axial resolution in 3D-SIM by a simpler dual-objective scheme, reaching lateral and axial resolution of ∼125 nm using conventional fluorophores without requiring interferometric detection.[69] This approach involves only a small adjustment to the shape of the OTF bands used, thereby showing great potential to be integrated into existing software reconstructing 3D SIM data (e.g., fairSIM).

Aiming to get SIM more live-cell compatible, recently, Jin et al. presented a new approach called deep learning assisted SIM (DL-SIM), acquiring SRM images with higher speed (∼20× faster than SRRF) and with low light levels (∼100× fewer photons).[46] DL-SIM allows faster imaging speed by requiring fewer raw images to reconstruct the image while also significantly reducing photobleaching as it can retrieve super-resolution information from low-light samples (Figure 3A). In this work, deep neural networks were trained on real images to visualize specific complex cellular compartments such as microtubules, mitochondria, etc. and applied to achieve multicolor, live-cell super-resolution SIM imaging of these cellular compartments.

SOFI is one example of a fluorescent probe fluctuation-based SRM, which is very close to SMLM techniques like PALM/STORM. However, SOFI only manages to improve resolution around 2- to 3-fold by its design. SOFI overcomes the resolution limit by analyzing stochastic fluorescence fluctuations with higher-order statistics. The spatial resolution and the sampling can increase up to n-fold in all spatial dimensions when analyzing with n^{th} order spatiotemporal cross-cumulants. Recently, Grußmayer et al. extended the cumulant analysis into the spectral domain and proposed a multicolor super-resolution scheme called multicolor SOFI (Figure 3B).[47] The authors demonstrated spectral unmixing of three fluorophore species for both fixed and live cells with two color channels.

Diffraction Unlimited SRM. Stimulated emission depletion microscopy (STED) breaks the spatial resolution limit by using an additional laser beam (STED beam) with a well-defined pattern to confine the area where fluorophores "are allowed" to be in an "on" state. The STED beam intensity is directly correlated with the achievable resolution. This SRM technique has been used greatly in various applications, including live/fixed cell imaging, slow/fast dynamics observations, and multicolor imaging. However, the nanometer resolution of STED microscopy often comes with a high cost in terms of photodamaging effects induced by the STED laser high intensity. Therefore, many alternative approaches have been introduced to reduce this drawback by employing adaptive illumination strategies such as RESCue (REduction of State transition Cycles)/DyMIN (DYnamic intensity MINimum) and MINFIELD-STED.[70] Another strategy that appears to be a solution for this issue is utilizing separation by the lifetime tuning (SPLIT) technique.[71] In SPLIT, the phasor analysis is applied to distinguish photons emitted from the center and the periphery of the excitation spot (photon separation), resulting in resolution enhancement without increasing the STED beam intensity. SPLIT was previously applied in a continuous wave STED beam (cw-STED). Recently, Tortarolo et al. extended this approach to pulsed STED beam to introduce a new method named pSTED SPLIT.[72] The authors showed that pSTED-SPLIT can achieve the same resolution while using significantly lower STED intensity compared to the raw STED counterpart (e.g., 50% I_{STED} for a target fwhm of 140 nm). Despite the excellent performance in achieving nanoscale resolution, temporal resolution sufficient to measure molecular diffusion is still quite a challenge for STED. Thus, fluorescence correlation spectroscopy (FCS) has been combined with STED to allow the direct investigation of fast dynamics at the relevant spatial scales. Sezgin et al. presented a straightforward protocol to perform point STED−FCS (pSTED−FCS) and scanning STED−FCS (sSTED−FCS) measurements. The authors demonstrated the use of this strategy to measure 2D diffusion dynamics in cellular membranes with molecules tagged with organic fluorophores.

Another approach belonging to the subgroup with STED microscopy (coordinate-targeted-based SRM) is RESOLFT. Instead of using the depletion phenomenon, RESOLFT

https://dx.doi.org/10.1021/acs.analchem.0c04361
Anal. Chem. 2021, 93, 41−71

achieves a favorable fluorescence inhibition scheme through long-lived on/off states with reversibly photoswitchable fluorescent labels. RESOLFT can provide nanometer resolution; however, illumination dose and imaging speed are still in need of improvements for better live-cell imaging. To tackle this challenge, recently, Dreier et al. introduced SmartRESOLFT, a new scanning strategy for low-illumination and fast RESOLFT (Figure 3C).[48] The scanning approach was built on a real-time feedback system, increasing the acquisition speed by ∼6-fold and reducing 70−90% of the light dose in in vivo imaging. The authors demonstrated the new method with nanoscale imaging of organelles such as mitochondria, peroxisomes (Figure 4E) up to 35 Hz, and actin dynamics in *C. elegans* (at 20−30 μm depth).

In single-molecule localization-based SRM (SMLM) techniques, single fluorophores are temporally separated; thus, sparse sets of individual emitters are collected over consecutive frames. Later, the image can be reconstructed by mapping the center positions of the single molecules detected. In SMLM, the resolution strongly depends on the labeling efficiency and photon yield of each molecule, which defines how well the underlying structure can be revealed and localized with precision, respectively. Thus, the localization precision is as important and should not be confused with resolution in SMLM.

Coelho et al. recently presented a new principle, active stabilization, that allows the direct measurement distance between molecules within the 1−20 nm scale in intact cells.[73] The authors presented an actively stabilized microscope utilizing 3D real-time drift corrections, resulting in a stabilization of <1 nm and ultrahigh localization precision of ∼1 nm. The newly developed microscope can be used to reveal a 4 to 7 nm difference in spatial separation between signaling T cell receptors and phosphatases (CD45) in active and resting T cells. With similar intentions to achieve high localization precision, Xu et al. presented a different approach called in situ point spread function retrieval (INSPR) SMLM.[74] The system showed the ability to construct an in situ 3D response of single emitters directly from single-molecule blinking data sets. The authors demonstrated the use of this method in imaging various organelles in mammalian cells (e.g., mitochondrial networks and nuclear pores) as well as in tissue (e.g., amyloid-β plaques and dendrites in brain tissues) at a depth of <20 μm, achieving 7−12 nm lateral and 21−45 nm axial precision in localization.

Confronting another desire of modern SRM, imaging multiple targets within the same sample, Klevanski et al. presented a new configuration to achieve highly multiplexed protein localization and called it maS^{3}TORM (Figure 3D).[49] The authors introduced a system that allows automated 3D direct STORM (dSTORM) imaging coupled with a solution-exchange scheme with a restaining protocol, thus facilitating multiplex labeling of tens of target proteins within the same sample. Consequently, this allows the observation of patterns that might get lost in multisample averaging. In this work, the maS^{3}TORM configuration was used to obtain 3D super-resolution images of 15 targets in single cells and 16 targets in individual neuronal tissue samples with <10 nm localization precision.

Another example of multiplexing SMLM (in this case, via DNA-FISH and RNA-FISH; fluorescence in situ hybridization, FISH) that has led to valuable information is 3D ATAC-PALM introduced by Xie et al.[75] This method combines an assay for transposase-accessible chromatin with microscopy (PALM and lattice light-sheet microscopy), allowing for imaging of the accessible genome in situ with nanometer resolution. The approach shows the potential to probe the structure and organizing mechanism of the genome. The authors analyzed genetically perturbed cells with 3D ATAC-PALM, discovering that genome architectural protein CTCF prevents excessive clustering of accessible chromatin and decompacts accessible chromatin domains.

Another technique in the single-molecule localization-based SRM family is PAINT.[76] Here, molecules are localized and mapped by stochastic switching via transient binding of fluorescent molecules to the target. In this method, multiple fluorescent molecules can bind to the same site over time; for instance, DNA-PAINT uses oligonucleotides pairing between the docking strand (binding to target protein) and the imagers (carrying the fluorophore label). Thus, multiplexed imaging of various targets can be achieved through a programmable and controllable transient-binding interaction. Wade et al. recently introduced an example utilizing "barcodes" to engineer blinking kinetics and allowing multiplexing of up to 124 targets.[77] Taking advantage of the controllable transient-binding interaction and applying it to another field of application, Brockman et al. presented the use of super-resolved tension PAINT (tPAINT) imaging to map cellular traction forces at the piconewton scale in living cells with a resolution of ∼25 nm.[78] In this work, the authors engineered reversible probes with a cryptic docking site that is only revealed when the probe experiences forces exceeding the mechanical threshold of ∼7−21 pN.

MINFLUX was introduced as a new approach that inherits the advantages of both coordinate-targeted and single-molecule localization-based techniques, thus reaching localization precision of <1 nm and resolution of $\lesssim$6 nm, and requires a 20-fold less photon count to acquire the same localization precision compared with traditional SMLM.[79] However, the technique is limited to a small field of view (FOV) of ∼50 × 50 nm^2 and requires a relatively long acquisition time of ∼50 s for such FOV.[50] Despite the limitations, MINFLUX is still one of the very few current nanoscopy techniques that can achieve single-digit nanometer 3D localization of fluorescently labeled molecules. Recently, Pape et al. showed that MINFLUX could achieve 3D multicolor super-resolved images via an application using 3D MINFLUX to image densely packed labeled proteins (e.g., subunits of the MICOS complex, a large protein complex within the mitochondrial inner membrane).[80] The authors reported the yield of a 3D localization precision of ∼5 nm in human mitochondria. This work demonstrated a high potential for use of multicolor 3D MINFLUX in analyzing the nanoscale arrangement of proteins within oligomeric protein complexes.

Recent Advances in Labeling Approaches and Fluorescent Probes for Super-Resolution Microscopy. The development of better labeling probes is a constant requirement for super-resolution imaging to achieve higher-quality and reliable images. Desired probes must be highly specific and small in size to reduce linkage error and assist in complete labeling. Permeability, solubility, photophysical criteria (e.g., brightness, photostability, switching kinetics), and the excitation/emission window of the fluorophores are likewise the targeted factors for improvements. In some recent reviews focused on live-cell imaging, the topic of fluorescent probes for SRM has also been discussed.[81,82] Here, we briefly

https://dx.doi.org/10.1021/acs.analchem.0c04361
Anal. Chem. 2021, 93, 41−71

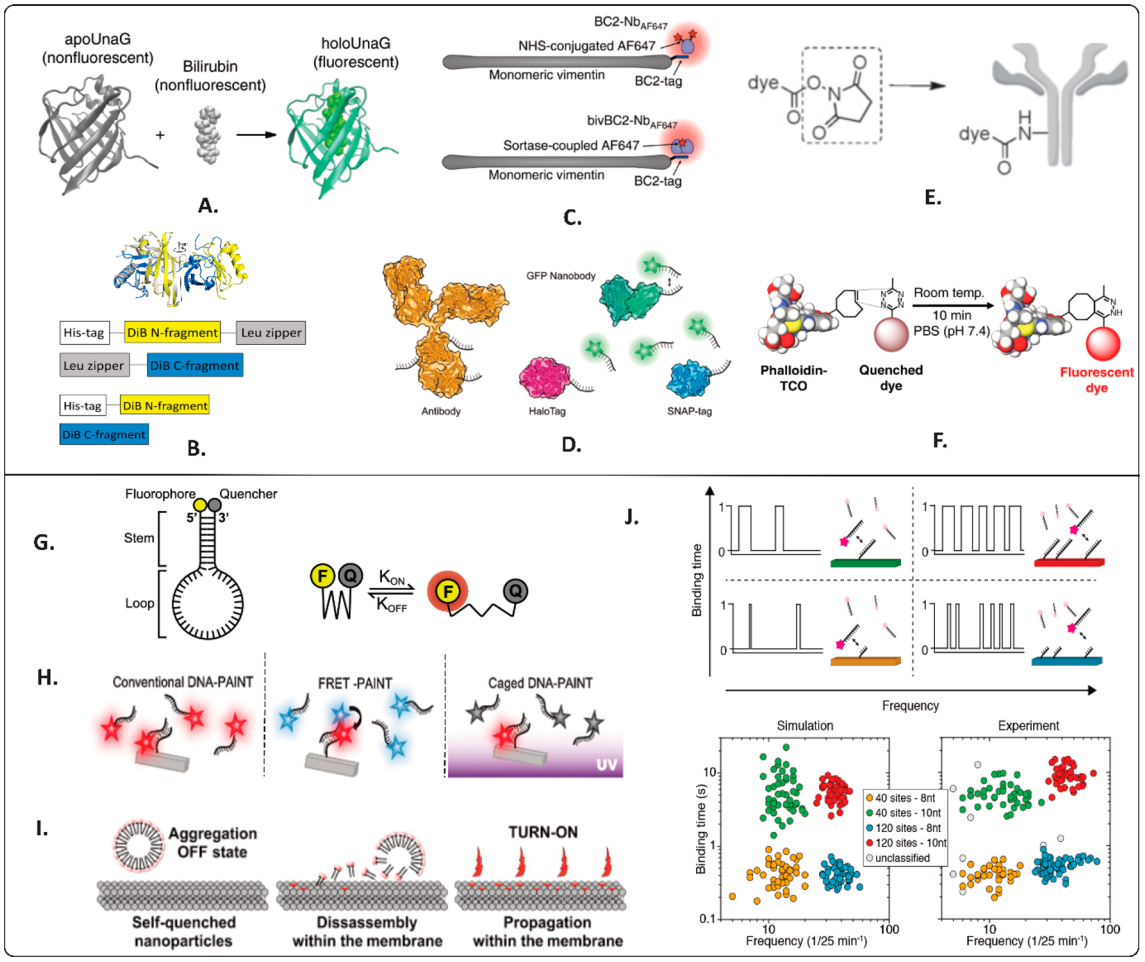

Figure 5. Updates on fluorescent probes and labeling strategies for super-resolution microscopy. (A) Scheme of BR-inducible fluorescence of UnaG. Crystal structures of apoUnaG, BR, and holoUnaG are obtained from the Protein Data Bank (PDB ID: 4I3B). (B) Schematic representation of the leucine zippers-containing "split-Zip" (upper panel) and leucine zippers-free "split" (lower panel) DiB-split protein constructs. (C) Schematic illustration of the BC2-Nb dye-conjugation strategies. Monovalent and bivalent BC2-Nbs were either conjugated with Alexa Fluor 647 (AF647) via *N*-hydroxysuccinimide (NHS) ester (upper panel) or linked to AF647 by enzymatic sortase coupling (lower panel). (D) Secondary antibody: yellow; GFP nanobody: green; HaloTag: magenta; SNAP-tag: blue conjugated with DNA strands for DNA-PAINT imaging. (E) Dye *N*-hydroxysuccinimidyl esters target: direct labeling of proteins. (F) Labeling with phalloidin-TCO followed by click labeling with different tetrazine−dyes. (G) Superbeacon structure (left) and model of transient quenching-mediated photoswitching (right). (H) Schematic representations of conventional DNA-PAINT (left), FRET-based DNA-PAINT (middle), and caged DNA-PAINT (right). (I) Turn-on mechanism of the MemBright probes. (J) Simultaneous multiplexed super-resolution imaging by engineering blinking kinetics. Panel A is reproduced from Kwon, J.; Park, J.; Kang, M.; et al. *Nature Communications* **2020**, *11* (1), 1−11 (ref 83). Panel B is adapted from Bozhanova, N. G.; Gavrikov, A. S.; Mishin, A. S.; Meiler, J. *Sci. Rep.* **2020**, *10* (1), 1−11 (ref 84). Panel C is reproduced from Virant, D.; Traenkle, B.; Maier, J.; et al. *Nature Communications* **2018**, *9* (1), 1−14 (ref 56). Panel D is reproduced from Direct Visualization of Single Nuclear Pore Complex Proteins Using Genetically-Encoded Probes for DNA-PAINT, Schlichthaerle, T.; Strauss, M. T.; Schueder, F.; et al. *Angew. Chem. Int. Ed. Engl.*, Vol. *58*, Issue 37 (ref 59). Copyright **2019** Wiley. Panel E is reproduced from Green-Emitting Rhodamine Dyes for Vital Labeling of Cell Organelles Using STED Super-Resolution Microscopy, Grimm, F.; Nizamov, S.; Belov, V. N., *ChemBioChem*, Vol. *20*, Issue 17 (ref 85). Copyright **2019** Wiley. Panel F is reproduced from Beliu, G.; Kurz, A. J.; Kuhlemann, A. C.; et al. *Communications Biology* **2019**, *2* (1) (ref 57). Panel G is adapted from Super-Beacons: Open-Source Probes with Spontaneous Tunable Blinking Compatible with Live-Cell Super-Resolution Microscopy, Pereira, P. M.; Gustafsson, N.; Marsh, M.; et al. *Traffic*, Vol. *21*, Issue 5 (ref 86). Copyright **2020** Wiley. Panel H is reproduced from Reductively Caged, Photoactivatable DNA-PAINT for High-Throughput Super-Resolution Microscopy, Jang, S.; Kim, M.; Shim, S. H.; *Angew. Chem. Int. Ed. Engl.*, Vol. *59*, Issue 29 (ref 87). Copyright **2020** Wiley. Panel I is reproduced from *Cell Chemical Biology 26* (4), Collot, M.; Ashokkumar, P.; Anton, H.; et al. MemBright: A Family of Fluorescent Membrane Probes for Advanced Cellular Imaging and Neuroscience, pp 600−614 (ref 58). Copyright **2019**, with permission from Elsevier. Panel J is adapted from Wade, O. K.; Woehrstein. J. B.; Nickels, P. C.; et al. *Nano Letters* **2019**, *19* (4), 2641−2646 (ref 77). Copyright 2019 American Chemical Society, https://pubs.acs.org/doi/10.1021/acs.nanolett.9b00508 and further permissions related to the material excerpted should be directed to the ACS. Panels A−D, G, and F are reproduced and adapted under a Creative Commons 4.0 International License (http://creativecommons.org/licenses/by/4.0/).

summarize the latest advances in fluorescent probes and labeling strategies for live and fixed samples within the last two years, expanding the potential of SRM in imaging to many more cellular targets and observing new biological phenomena.

Making Target Proteins Fluorescent. A broad range of labeling probes, including fluorescent proteins, fusion tags, antibodies, antigen-binding fragments, aptamers, nanobodies, nanoparticles, and small-molecule fluorophores available for SRM, is in continual development. Conventional fluorescent

https://dx.doi.org/10.1021/acs.analchem.0c04361
Anal. Chem. 2021, 93, 41−71

proteins (FPs) are popular due to their labeling simplicity and specificity; however, they often have limitations in photophysical criteria and color options. Organic dyes have excellent photophysical properties but suffer high background fluorescence from nonspecific binding. Fluorogen probes, on the other hand, do not fluoresce unless bound to their specific small-molecule fluorogens. Therefore, this class of probes has a high potential to become more popular as they open up opportunities for rapid, specific labeling with a high signal-to-noise ratio and also multicolor SRM.

Kwon et al. presented a bright ligand-activatable fluorescent protein holoUnaG (Figure 5A)[83] that strongly fluoresces only upon binding to a fluorogenic metabolite, bilirubin, achieving equivalent quantum yield to the current brightest photoswitchable red protein. The nature of apo/holoUnaG results in a low fluorescence background and reversible switching with easily controllable kinetics. The concentration of the ligand controls the on-switching rate, while the excitation light intensity and the dissolved oxygen control and promote the off-switching rates, respectively. As the ligand binds to UnaG via noncovalent interactions instead of ligand−protein covalent bonds as in conventional FPs, the photo-oxidized ligand will detach and leave the binding cavity empty for rebinding to a new ligand molecule. This makes holoUnaG a suitable probe for PALM/STORM and PAINT imaging. With all of these features, the authors demonstrated live-cell SMLM imaging with up to three colors for various subcellular structures genetically encoded with UnaG. UnaG shows the potential to become the next default protein for high-performance super-resolution imaging.

With the effort of developing smaller probes, Bozhanova et al. presented a self-assembling fluorogen-activating protein (FAP) split system called DiB-splits (Figure 5B), decreasing the size of the FAPs label to ∼8−12 kDa.[84] The authors showed that the two fragments of the split protein could spontaneously reassemble to restore the properties of the parental full-length DiBs, including strong fluorescence upon binding, excellent binding affinities down to the nanomolar range, and high photostability of the protein−ligand complex. The probe was used as a smaller size protein-PAINT label for live-cell SRM. DiB-splits were also suggested to be used for developing protein−protein interaction detection systems.

Fusion proteins with an additional polypeptide/protein tag (e.g., SNAP-tag, ∼20 kDa; Halo-tag, ∼33 kDa) that later incorporate with exogenously added fluorophores are also widely used in SRM. Virant et al. presented a short and inert BC2 peptide-tag and a corresponding high-affinity bivalent nanobody (bivBC2-Nb) for dSTORM imaging (Figure 5C).[56] BC2-tagging was shown to not disturb the native structures (vimentin, lamin, actin, and tubulin), and bivBC2-Nb staining achieved high labeling coverage with minimal linkage errors (Figure 4D, left). The authors also reported that bivBC2-Nb could retain its function and its binding capacity toward its target structures in living cells, demonstrating the ability of the BC2-tag/bivBC2-Nb labeling system for SRM imaging of both fixed and living cells.

Expanding further the use of fusion proteins, Schlichthaerle et al. combined protein tags with DNA-PAINT docking strands, making it available for DNA-PAINT microscopy (Figure 5D).[59] The authors presented a strategy to target the DNA-conjugated ligands benzyl guanine (BG) and chloroalkane against the SNAP-tag and Halo-tag, respectively. This approach enabled 1:1 labeling of single proteins in the nuclear pore complex (NPC) (Figure 4G), resolving single copies of nucleoporins in the human Y-complex in 3D with approximately a 3 nm precision. However, Schlichthaerle et al. also reported that, currently, the labeling efficiency is only about 30%.

It should be noted that, although the size of these additional polypeptide/protein tags usually does not directly affect the functions of the host proteins, the expression levels of the fusion proteins can immensely alter their localization, consequently affecting cellular function. The artifact caused by overexpression can be reduced with the help of gene editing, creating knock-in cell lines that produce fusion proteins expressed under their endogenous promoter.

The additional polypeptide/protein tags are usually designed to locate at either N- or C-termini of the target proteins, limiting the access to other preferred sites. The use of unnatural amino acids integrated into proteins can help to solve this issue. Beliu et al. presented an example of this approach, demonstrating bioorthogonal labeling with 22 tetrazine derivatives covering the whole visible wavelength range, applicable in both fixed and live-cell imaging.[57] First, noncanonical amino acids (ncAAs) with small functional groups were introduced to any desired position in a target protein by genetic code expansion technology. Later, the protein carrying trans-cyclooct-2-ene (TCO)-modified ncAAs were labeled with a tetrazine−dye conjugate via the Diels−Alder reaction (Figure 5F). This labeling strategy also showed the potential for fluorogenicity. The authors discovered that, in red-absorbing oxazine and rhodamine derivatives, photoinduced electron transfer from the excited dye to tetrazine results in quenching; later, upon reaction with dienophiles, quenching interactions are reduced, thus increasing fluorescence intensity substantially. Plus, the difference in cell permeability of the tetrazine−dyes enabled specific intra/extracellular labeling of proteins. This labeling approach was applied for the dSTORM imaging of the membrane receptors, actin, and tubulin, observing microtubule dynamics in living cells.

Another approach is to label proteins by conjugating fluorophores to ligands that bind to the target proteins with high affinity and specificity. Belov et al. presented an example of this approach, developing synthesized jasplakinolide analogs that bind with high specificity to F-actin, which were successfully applied in live-cell STED imaging.[88] In this work, des-bromo-des-methyl-jasplakinolide-lysine (ligand) was later coupled with the red-emitting fluorescent dyes 580CP and 610CP via a 6-aminohexanoate linker. This strategy provided an extra labeling option for observing actin dynamics (Figure 4D, right). Nevertheless, it should also be noted that the targeted protein might be affected by the binding (e.g., jasplakinolide could stabilize F-actin[82]).

Immunolabeling probes are also a significant group that provides a comparatively good labeling specificity, high signal amplification, and various color options. The application of antibodies in SRM is still limited due to the relatively large size (∼150 kDa), bivalency, and polyclonality. Other smaller probes such as antigen-binding fragments (∼50 kDa), aptamers (7−30 kDa), and nanobodies (∼15 kDa) have a great potential for use with SRM. An example of this is modified aptamers SOMAmers developed by Strauss et al., enabling quantitative sub-10 nm cellular DNA-PAINT imaging.[89] More unique than other DNA aptamers, SOMAmers contain modified bases with hydrophobic residues,

https://dx.doi.org/10.1021/acs.analchem.0c04361
Anal. Chem. 2021, 93, 41−71

similar to the amino acid residues abundant in antibody epitopes used for the high-specificity high-affinity binding of proteins. Coupling with the multiplexing capabilities of Exchange-PAINT, the SOMAmers approach shows the potential to image multiple cellular targets in single cells or allow live labeling and imaging of membrane-bound proteins. Additionally, Sograte-Idrissi et al. presented the benefit of using secondary nanobodies over secondary antibodies in SRM (demonstrated with STED, DNA-PAINT, and light-sheet microscopy) to avoid common labeling artifacts.[90] In this work, the use of secondary nanobodies showed significant increases in localization accuracy and improvement of penetration efficiency. It also allowed the direct premixing with primary antibody before staining (reducing time, multiple primary antibodies of the same species can be used) and avoided clustering artifacts of target molecules.

Nanoparticles have been a considerable source of labeling probes due to their excellent photophysical properties such as brightness and high resistance to photobleaching. However, there are still many drawbacks (e.g., unspecific labeling, poor biocompatibility, cross-linking, aggregation via multiple reactive groups[91]) to overcome in the new generation of nanoparticle probes. Utilizing nanoparticles a bit differently, Li et al. presented the use of fluorescent magnetic nanoparticles (FMNPs) to track and manipulate membrane protein motion at the single-molecule level in live cells.[92] This strategy achieved single-particle tracking at 10 nm and 5 ms spatiotemporal resolution. With a magnetic needle, applying femtonewton-range forces, the authors were able to drag membrane proteins over the surface of living cells, consequently detecting barriers localized to the submembrane actin cytoskeleton. This is a new approach to probe membrane processes in live cells. The authors also referred to the potential of FMNPs for PALM or live-cell STED to capture the cellular dynamic cellular environment.

Equally essential to the desired fluorophores, the delivery system for cell-impermeable organic fluorescent probes into living cells also has significant developments recently. As an example of this, Zhang et al. presented new peptide vehicles, improving the live-cell labeling efficiency by simple coincubation and opening up the opportunity for multicolor imaging.[93] The peptide vehicle was described as a very efficient *"trojan horse"* for intracellular delivery.[94] Employing the concept of cell-penetrating peptides, the authors discovered a positively charged peptide vehicle (PV-1) containing 12 amino acids having excellent features for efficient membrane translocation of cell-impermeable organic fluorescent probes.

Regulating the Fluorophores. In SRM, the ability of the fluorophore to "switch" between an "on" and an "off" state is required; however, the mechanism to achieve these on/off states is different in various SRM techniques. For example, STED uses a depletion laser; in contrast, many single-molecule localization-based SRM techniques utilize stochastic switching/blinking of fluorescent probes or, more recently, via emission fluctuation. Consequently, STED requires fluorophores to be very photostable; however, several SMLM dyes employ mechanisms associated with photobleaching to switch to "off" states. Thus, the search for universal fluorophores for all SRM techniques may not be easy to achieve.

For single-molecule localization-based SRM, much progress has been made to improve the fluorophores to be live-cell compatible and to allow longer time-lapse and multiplex imaging with better imaging speed. Recently, Pereira et al. presented a set of self-quenching probes named Superbeacons that have photoswitching kinetics that can be tuned structurally, thermally, and chemically.[86] With Superbeacons, highly efficient photoswitching is achieved upon the DNA-hairpin scaffold resembling molecular beacons altered instead of oligonucleotide sensing (Figure 5G). As the switching between emitting/nonemitting states is stochastic and independent of illumination, Superbeacons are more compatible with live-cell experiments, allowing imaging with low illumination and without toxic photoswitching inducing buffers.

Collot et al. presented a family of blinking fluorescent membrane probes named MemBright suitable for STORM-type SRM.[58] MemBright is available with six different colors within the spectral range of 550−850 nm and operates at very low concentrations (nM) in live or fixed cells (Figure 5I). For multicolor imaging, it can be used in combination with immunofluorescence, labeling multiple targets. With MemBright, the authors showed the nanoscale organization of both axonal and dendritic compartments and endogenous glutamate receptor clusters in cells with multicolor 3D STORM (Figure 4F).

Halabi et al. introduced another approach using photoregulated fluxional fluorophores, named PFF1, allowing long (>30 min) live-cell time-lapse in both 2D and 3D SMLM.[95] With this approach, the author showed that a fraction of the total nonfluxional isomer was converted to a fluxional form upon photoactivation. At this stage, the thermal equilibrium between fluorescent and dark species was used for single-molecule imaging. After the whole population of fluxional molecules was photobleached, there was a replacement with a new subset of molecules, enabling a very long time-lapse with low phototoxicity. PFF1 allowed one to track several intracellular organelles, including synaptic vesicle trafficking in live human neurons. The author reported achieving a resolution of nearly 60 nm and subsecond time resolution.

Jang et al. presented a probe enabling a faster imaging speed by 2 orders of magnitude, bringing DNA-PAINT closer to high-throughput SRM.[87] In this work, reductive caging was applied onto DNA-PAINT imagers to create bright photoactivatable probes with low background and photobleaching resistance. The imager strand was chemically reduced into a dark state by chemical deactivation and then selectively activated using UV TIR illumination (Figure 5H).

Wade et al. presented a novel approach to multiplexed SRM, allowing the simultaneous detection of 124 colors within minutes.[77] Engineering blinking kinetics in DNA-PAINT was adopted to created "barcodes" using a single imager strand. In this work, the "barcodes" define both blinking frequency and binding duration. The number of binding sites determines the blinking frequency, and the length of the docking strand on a specific target defines the binding duration (Figure 5J). The approach was successfully applied for multiplexed RNA and protein detection in cells. Kinetic barcoding shows enormous potential to expand the capacity of SRM.

For STED, many of the available dyes have emission wavelengths in the far-red or near-infrared to reduce phototoxicity (suitable for 765/775 nm STED lasers) or have large Stokes shift, allowing the use of the same STED laser to deplete several fluorophores while maintaining several excitation windows in multicolor imaging. A lot of effort has recently been focused on developing more photostable dyes emitting in the shorter range suitable for 592/595 and 660 nm

https://dx.doi.org/10.1021/acs.analchem.0c04361
Anal. Chem. 2021, 93, 41−71

STED lasers. The newly developed dyes also allow longer time-lapse and enhance the biocompatibility for live-cell STED.

Grimm et al. developed two bright and photostable green-emitting rhodamine dyes, LIVE 510 and LIVE 515, suitable for 592/595 nm STED lasers.[85] The dyes can penetrate the intact plasma membrane, allowing labeling in living cells. The authors also demonstrated high selectivity and specificity labeling by incorporating LIVE 510 and LIVE 515 into probes for lysosomes, mitochondria, tubulin, and actin.

Wang et al. presented a superphotostable fluorescent molecule, MitoPB Yellow, for live-cell STED. This probe allowed imaging of the mitochondrial cristae dynamics by SRM for the first time (Figure 4C).[55] MitoPB Yellow has a long fluorescence lifetime due to structurally reinforced naphthophosphole fluorophore conjugating with an electron-donating diphenylamino group. With MitoPB Yellow, the mitochondrial cristae's ultrastructures were selectively captured at a resolution of ∼60 nm (using a 660 nm STED laser). This label also offers a chance to get a better insight into dynamic ultrastructures such as the intermembrane fusion and the intercristae mergence.

Bucevičius et al. demonstrated a new strategy to enhance the biocompatibility of rhodamine fluorescence probes by the use of a neighboring group effect.[96] The authors showed that positioning an amide group next to a carboxyl group in the benzene ring of the rhodamine significantly improves cell permeability of the rhodamine-based probe as this stabilizes a fluorophore in a hydrophobic spirolactone state. With this approach, Bucevičius et al. created probes targeting tubulin, actin, and DNA with excellent staining efficiency allowing long-term STED imaging with sub-30 nm resolution in living cells.

Dual labeling probes for correlated STED and NanoSIMS imaging were developed and tested by Phan and co-workers.[97,98] The authors synthesized the probes that incorporate boron or fluorine to fluorescent dyes, allowing the image of specifically targeted proteins with fluorescence and NanoSIMS imaging. NanoSIMS is discussed in the next section of mass spectrometry imaging of cells and organelles.

Other Points of Consideration for High-Quality Super-Resolution Images. The quality of the SRM images does not just depend on the labeling or the process of acquiring images but also very much depends on other steps of the sample preparation such as fixation or even mounting in the case of fixed cell imaging. Furthermore, with the desire to get closer to high-quality quantitative SRM, the need for reference standards has also become more critical than ever.

Arsić et al. showed the effect of Vectashield, one of the most commonly used mounting media, causing the loss of fluorescence intensity of Alexa Fluor 647 (AF647) via fluorescence quenching.[99] As AF647 blinks in Vectashield, this dye-mounting media combination is often used for dSTORM. However, the authors observed that the fluorescence intensity of AF647 is quenched after mounting immunolabeled samples in Vectashield. This loss was noticed in the immunostainings of several components of the neuronal cytoskeleton and axonal initial segment. Offering solutions for this issue, the authors provided a quantitative analysis of AF647 intensity in different imaging media and quantitative analysis examining the Vectashield performance for dSTORM imaging in high- and low-abundance AF647-labeled targets.

Concerned that the effect of fixation on preserving authentic cellular structures would strongly affect image reliability, Stanly et al. presented work investigating the critical importance of the appropriate fixation conditions for advanced fluorescence microscopy.[100] The authors demonstrated this by showing the artifactual clustering of receptors in lymphatic endothelial cells induced by an inadequate fixation in PFA alone. Additionally, Richter et al. presented fixation protocols using glyoxal, which was shown to be a better alternative to PFA for immunostaining.[101] In this work, the author confirmed that glyoxal performs protein cross-linking faster and more effectively than PFA, improving cellular morphology preservation.

Mund and Ries highlighted the importance of using suitable reference standards and summarized a guideline for thoroughly optimizing the imaging pipeline in quantitative SRM.[102] The approach helps when characterizing the performance of a microscope over time, serves as a benchmark to evaluate newly developed microscopy or labeling techniques, allows a comparison of SRM data between laboratories and, more importantly, when performing high-quality quantitative and absolute measurements. A year earlier, Ries's group presented the use of nuclear pores as universal reference standards.[103] Recognizing the need for biologically relevant control standards, the authors chose to use the nuclear pore complex as an in situ reference due to the stereotypic arrangement of the proteins in the complex. Four gene-edited cell lines that endogenously labeled nucleoporin Nup96 with mEGFP, SNAP-tag, Halo-tag, or the photoconvertible fluorescent protein mMaple were generated. They were used as 3D resolution standards for calibration and quality control and precise reference standards for molecular counting and absolute quantification of labeling efficiencies.

Updates on Software/Toolboxes for Super-Resolution Image Analysis. With rapid development in all aspects, SRM has become a powerful imaging tool to study nanoscale biological processes. However, excellent quality SRM images also come with a high demand for specialized image analysis tools to process a large volume of data, reconstruct reliable images, and extract quantitative information.

Henriques's group developed a high-performance open-source image analysis toolbox for SRM named NanoJ, available as a series of ImageJ-based plugins that can be used independently or in parallel.[104] NanoJ includes many modules (NanoJ-Core, NanoJ-SRRF, NanoJ-VirusMapper, NanoJ-Fluidics, and NanoJ-SQUIRREL) capable of solving common imaging problems in several processing steps. For instance, NanoJ-SQUIRREL is an algorithm to evaluate the resolution and detect artifacts in super-resolution images thoroughly. The current common practice for measuring image resolution in localization-based SRM images uses the Fourier ring correlation, which only provides a single resolution measurement for the whole SRM image. However, the resolution is not always homogeneous across the field of view, especially when localization accuracy varies by different labeling densities and laser illumination intensities. Additionally, with point-like patterns, FRC performance could be biased. Henriques and colleagues showed that the error mapping functionality of NanoJ-SQUIRREL complements FRC; thus, it provides a comprehensive assessment of super-resolution image quality.

Ries presented another open-source analysis platform for localization-based SRM data named SMAP.[105] SMAP has a freely configurable graphical user interface (GUI) and currently contains more than 200 plugins assisting all data analysis steps, including determining single-molecule positions to postprocessing (e.g., merge localizations in consecutive

https://dx.doi.org/10.1021/acs.analchem.0c04361
Anal. Chem. 2021, 93, 41−71

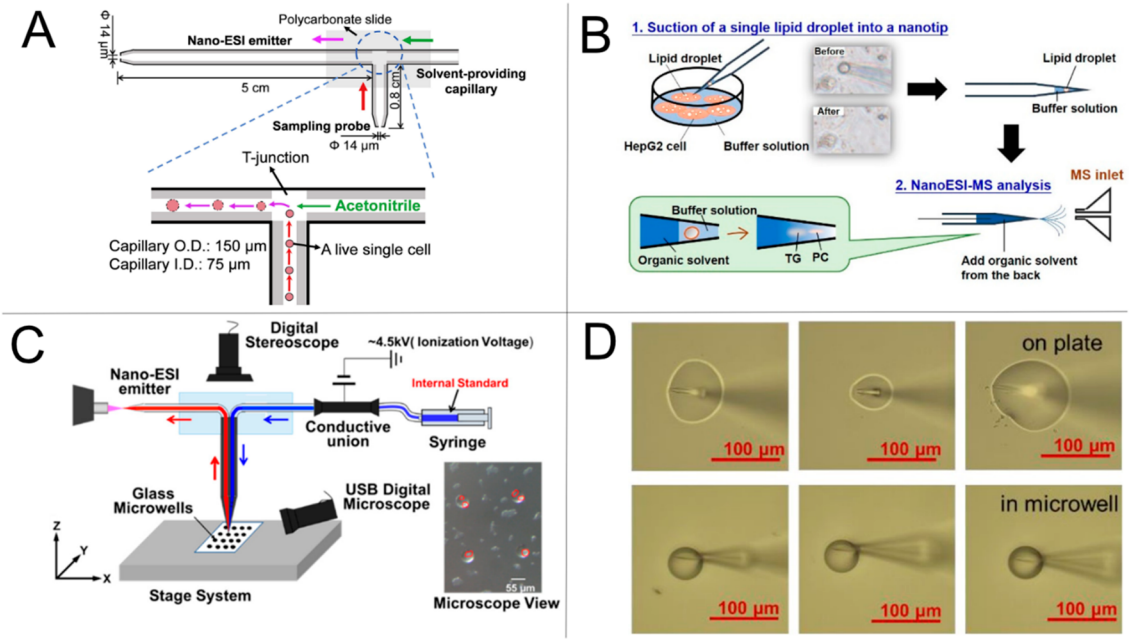

Figure 6. single-cell methods with ESI-MS. (A) Schematic of the T-probe and mechanisms of SCMS analysis. The inset shows the single cell withdrawn into the cell sampling probe undergoes a rapid (within a few seconds) lysis. single-cell lysate is immediately ionized through the nano-ESI emitter for MS analysis. Reprinted with permission from Zhu, Y.; Liu, R.; Yang, Z. Redesigning the T-probe for mass spectrometry analysis of online lysis of nonadherent single cells. *Anal. Chim Acta.* **2019**, *1084*, 53−59. Copyright 2019 Analytica Chimica Acta (ref 110). (B) Schematic of single lipid droplet analysis with ITSME-MS. Reprinted from Zhao, Y.; Chen, Z.; Wu, Y.; Tsukui, T.; Ma, X.; Zhang, X.; et al. Separating and Profiling Phosphatidylcholines and Triglycerides from Single Cellular Lipid Droplet by In-Tip Solvent Microextraction Mass Spectrometry. *Anal. Chem.* **2019**, *91* (7), 4466−4471. Copyright 2019 American Chemical Society (ref 111). (C) qSCMS experimental setup with individual cells highlighted in the microscopic image of the glass microwells. Reprinted from Pan, N.; Standke, S. J.; Kothapalli, N. R.; Sun, M.; Bensen, R. C.; Burgett. A. W. G.; et al. Quantification of Drug Molecules in Live Single Cells Using the Single-Probe Mass Spectrometry Technique. *Anal. Chem.* **2019**, *91* (14), 9018−9024. Copyright 2019 American Chemical Society (ref 114). (D) Comparison of the microextraction on the plate and in the microwell. Optical images of droplet microextraction on the plate (top row) and in the microwell (bottom row). Reprinted in part from Feng, J.; Zhang, X.; Huang, L.; Yao, H.; Yang, C.; Ma, X.; et al. Quantitation of Glucose-Phosphate in Single Cells by Microwell-Based Nanoliter Droplet Microextraction and Mass Spectrometry. *Anal. Chem.* **2019**, *91* (9), 5613−5620. Copyright 2019 American Chemical Society (ref 121).

frames, perform 3D drift correction, etc.), rendering, and advanced analyses. SMAP is now also available in MATLAB. Another nice feature of SMAP is that any users can reproduce results from raw data as all analysis steps and parameters are logged.

MASS SPECTROMETRY OF SINGLE CELLS AND ORGANELLES

In the past several decades, single-cell and subcellular analysis studies have been receiving increasing interest due to the growing need for characterizing individual cell metabolic profiles and intracellular environments, as opposed to tissue and cell population averages. Some of the main obstacles to single-cell analysis include the relatively low sample volume of a single cell (generally down to picoliter scale), the complex biological composition of the subcellular environment (which can lead to interferences during analysis due to ever-present chemical and physiological processes), and the need for multidimensional profiling (i.e., simultaneous structural and chemical information).

Mass spectrometry (MS) in the analysis of single cells has seen many advances with respect to sensitivity, specificity, and cell profile coverage. Numerous types of single-cell mass spectrometry (SCMS) methods have been developed with the use of different combinations of ionization, mass separation, and detection techniques, and novel applications are presented regularly within the literature. Both vacuum and ambient approaches have been thoroughly developed, and each provide separate benefits and drawbacks. Soft- and hard-ionization methods exist and can be selected depending on whether large, high mass molecular fragments or smaller, low mass molecular fragments, respectively, are to be detected. A comprehensive review on the subject of single-cell analysis by the use of MS was recently published by Gu and co-workers, and it includes detailed outlines of MS techniques.[106]

Mass Spectrometry Based on Electrospray Ionization. Mass spectrometry based on electrospray ionization (ESI-MS) is considered a soft-ionization technique, and it allows one to sample single cells (live cultured or tissue embedded) at ambient conditions, which minimizes artifacts and interferences. ESI-MS generally does not allow imaging of samples, although there are exceptions with ESI methods that have been adapted for this purpose. NanoESI is a development of conventional ESI, which involves low sample consumption and is thus well suited for single-cell analysis.[107] In nanoESI, the sample (single-cell contents or a whole single cell) is collected in a microcapillary tip and ionized by applying a high voltage. Charged microdroplets are generated, and selected ions are separated, then detected, and identified using MS.

NanoESI has seen special improvements by the introduction in 2014 of the Single-probe, a sampling and ionization device, by Yang and co-workers.[108] The probe comprised a laser-pulled tubing, a silica capillary, and a nanoESI emitter and allowed in situ MS analysis of live cells in real time at ambient

https://dx.doi.org/10.1021/acs.analchem.0c04361
Anal. Chem. 2021, 93, 41−71

conditions. In 2018, Zhu et al. introduced another design termed a "T-probe".[109] This probe was fabricated via a semiautomated protocol and tested via analysis of single HeLa cells under control and anticancer drug treatment conditions. More recently, Zhu et al. reported an improved redesign of the T-probe (Figure 6A) which, compared to the previous design, features a larger sample orifice and a longer nanoESI emitter.[110] The first feature allows sampling of an entire single cell instead of just withdrawing cellular contents, avoiding sample loss; the second feature increases the time for inducing cell lysis inside the emitter, boosting throughput.

Zhao et al. developed a novel ESI-MS technique termed in-tip solvent microextraction mass spectrometry (ITSME-MS), which allowed the profiling of lipids within single liquid droplets (LDs) sampled from individual HepG2 cells.[111] This technique specifically enabled the separation between phosphatidylcholines (PCs) and triglycerides (TGs), which was not yet possible with other ESI-MS methods. Figure 6B shows a schematic of ITSME-MS. The LD was sucked into a nanoESI nanotip emitter using a three-dimensional mobile manipulator and an inverted microscope; a gradient solvent system was then generated at the tip, and nanoESI-MS was performed. An LTQ orbitrap mass spectrometer fitted with a nanoESI source was employed. The separation between PCs and TGs thus took place owing to the varied solubility of these lipids in the solvent, resulting in different MS detection times.

In the past couple of years, Yang and co-workers further reported the use of other probe-ESI (PESI) SCMS techniques.[112] Standke et al. combined a cell manipulation platform commonly used for in vitro fertilization with the single-probe sampling technology to analyze the metabolic composition of single K562 cells (a suspension leukemia cell line).[112] Zhu et al. fabricated a micropipette by combining a pulled glass capillary needle and a fused silica capillary and induced Paternó-Büchi reactions in single HCT-116 cells (a human colon cancer cell line) to determine the location of C=C bonds of unsaturated lipids.[113] Pan et al. carried out quantitative SCMS experiments using the single-probe technique and custom glass microchips with microwells (Figure 6C) and directly quantified the absolute amount of irinotecan in single HeLa and HCT-116 cells.[114] Additionally, Liu and co-workers used a reduced graphene oxide functional copper probe (rGO-Cu probe) to analyze several neurotransmitters in single PC12 cells (a rat pheochromocytoma cell line). The many advantages of this probe and the setup are well described in the paper, and further applications for rapid, in situ detection of analytes in living single cells are suggested.[115]

Another sampling ESI approach is laser-ablation ESI (LAESI). This method, introduced by Nemes and Vertes in 2007,[116] utilizes mid-IR laser beam pulses to ablate a sample surface and subsequently desorp and ionize the ejected analytes. Stopka et al. integrated fluorescence and brightfield microscopy with fiber-based LAESI-MS (f-LAESI-MS) to selectively target single leaf blade cells in *Egeria densa* leaf tissue and reveal metabolic variations between different cellular subpopulations (i.e., epidermal cells and excretory idioblasts). This type of analysis is reportedly not ideal for animal cell analysis, where higher sensitivity is needed, although possible mitigation strategies are suggested in the paper.[117]

ESI can also be coupled with capillary electrophoresis (CE). CE is a well-established separation method for single-cell analysis as it is associated with nanoscale sample volumes and high separation efficiency. An original application of CE-ESI-MS was reported recently by Portero and Nemes, who profiled both cationic and anionic metabolites in the same single embryonic cell in a sequential manner.[118] CE-ESI-MS is usually restricted to cationic analysis due to electrical discharges at the electrospray emitter in the negative mode. Here, this limitation was minimized by enclosing the CE-ESI interface in a nitrogen gas-filled chamber. Cell material from live embryos was collected by capillary microsampling; complementary ionic species separation was achieved by using different background electrolytes, and species were later detected using a CE-ESI system coupled to a quadrupole time-of-flight (ToF) mass spectrometer. The study finally achieved enhanced, dual cationic−anionic characterization of small polar metabolites in single cells.

In CE, sample injection can be performed electrokinetically or hydrodynamically. However, in CE-ESI-MS, hydrodynamic injection is often chosen due to solvent and sample volume requirements. Sweedler and co-workers developed an approach for detecting metabolites in a single pleural sensory neuron via field amplified sample injection (FASI) CE-ESI-MS.[119] FASI was performed by electrokinetic injection, and it was directly compared to classic hydrodynamic injection in terms of performance. Both techniques were carried out on single neurons, and several cationic metabolites were detected and quantified. It was reported that the FASI approach yielded a better detection limit for metabolites.

Various other approaches of mass spectrometric analysis based on ESI have been reported recently. Among these, Xu et al. established an electrosyringe-assisted ESI-MS method to sample from the delicate structures or body of single primary cultured rat hippocampal neurons.[120] The setup comprised a nanocapillary, a Pt wire, a voltage generator for electrospraying, and a Q-ToF mass spectrometer. This is the first example of single axon, dendrite, and cell body molecular profiling in single living neurons, and it revealed the molecular distribution of certain analytes in distinct parts of the neurons. Feng et al. proposed a method to quantitatively detect glucose phosphate in K562 cells (a human leukemia cell line) by droplet microextraction MS in the microwell.[121] The use of the microwell provided reproducibility of the internal standard trace concentration during sampling, improving precision and accuracy of the quantification of the analyte. A comparison of microextraction on the plate and in the microwell is presented in Figure 6D.

Mass Spectrometry Based on Laser-Desorption/Ionization. The rudiments of optical pumping were first reported during the 1960s, and the approach has since been greatly implemented.[122−124] Building on decades of refinement, today, mass spectrometry based on laser-desorption/ionization (LDI-MS) has found widespread use in a variety of applications. In LDI-MS, a sample is irradiated by a laser beam that ionizes its surface, and subsequently, the mass-to-charge ratios of the ejected ions are detected and analyzed with a mass spectrometer. LDI can be either matrix-free or matrix-assisted (MALDI); the use of a matrix allows for softer ionization and imaging of intact macromolecules. While the spatial resolution is generally limited to a few hundred nanometers, novel optics systems are continuously being researched to push the boundaries of laser-based MS.

A recent advance is the development of near-field desorption postionization MS (NDPI-MS) by Tian and co-workers for correlated chemical imaging and 3D topographical reconstruc-

https://dx.doi.org/10.1021/acs.analchem.0c04361
Anal. Chem. 2021, 93, 41−71

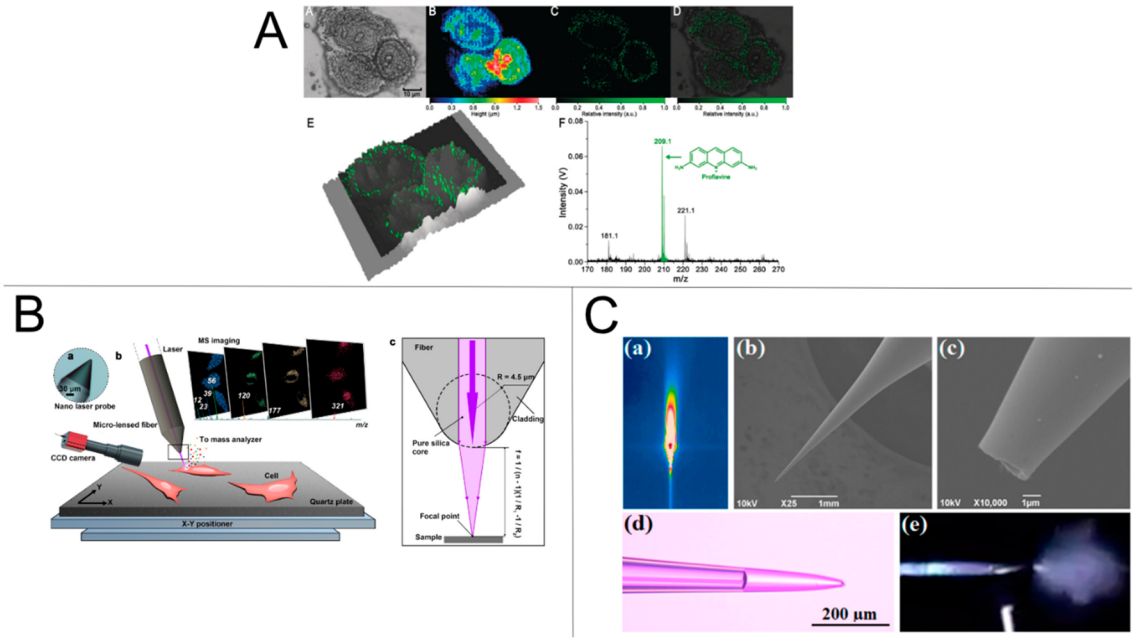

Figure 7. Mass spectrometry based on laser-desorption/ionization. (A) Multimodal images of the subcellular proflavine distribution within HeLa cells. (*A*) An optical image, (*B*) a topographical image (128 × 28 pixels) and (*C*) an MS image with a pixel size of 250 nm and two pulses for each pixel, (*D*) an overlay of the optical and chemical images, (*E*) a 3D topographically reconstructed chemical image, and (*F*) a single-pixel mass spectrum derived from a subcellular area containing proflavine. Reprinted with permission from Yin, Z.; Cheng, X.; Liu, R.; Li, X.; Hang, L.; Hang, W.; Xu, J.; Yan, X.; Li, J.; Tian, Z. Chemical and Topographical Single-Cell Imaging by Near-Field Desorption Mass Spectrometry. *Angew. Chem.* **2019**, *131* (14), 4589−4594. Copyright 2019 Angewandte Chemie (ref 125). (B) Nano laser probe-based MSI system. (a) A microscope photograph of the tip of the nano laser probe (NLP), (b) diagram of the ion source and MSI process, and (c) focusing principle of the nano laser probe. Reprinted with permission from Meng, Y.; Cheng, X.; Wang, T.; Hang, W.; Li, X.; Nie, W.; et al. Micro-Lensed Fiber Laser Desorption Mass Spectrometry Imaging Reveals Subcellular Distribution of Drugs within Single Cells. *Angew Chem.* **2020**, 18020−18027. Copyright 2020 Angewandte Chemie (ref 128). (C) (a) Thermal imaging of the hydrogen flame (VH2/VCO2 = 1:1), (b, c) SEM images of the tip of the probe, (d) microscope image of the probe postsampling, and (e) photograph of the thermal desorption spray plume. Reprinted from Zhao, J. B.; Zhang, F.; Guo, Y. L. Quantitative Analysis of Metabolites at the Single-Cell Level by Hydrogen Flame Desorption Ionization Mass Spectrometry. *Anal. Chem.* **2019**, *91* (4), 2752−2758. Copyright 2019 Americal Chemical Society (ref 129).

tion.[125] The potential of this technique was demonstrated by imaging the distinct subcellular 2D and 3D distribution of proflavine and other compounds in HeLa cells (Figure 7A) with 350 nm lateral resolution. The feasibility for single-cell measurements using NDPI-MS was rapidly confirmed in a paper by Hang and co-workers, in which the accumulation patterns of proflavine and ethacridine in different subcellular compartments were 3D imaged at the single-cell level.[126] In a further study by Cheng et al., NDPI-MS was applied to image silver and gold nanoparticles (NPs) in single mouse macrophage cells.[127] NPs receive considerable attention particularly in the biomedical field due to their applications in areas such as targeted drug delivery and toxicology assays; these innovative NDPI-MS approaches reportedly bridge the gap between LDI-MS and multimodal single-cell imaging and open the door to novel tools for drug monitoring via laser-based, high resolution single-cell MS.

Meng et al. considered the matter of high costs and complexity of modern, ever-advancing MS methods; they introduced a nano laser probe-based LDI-MS that only requires an existing LDI-MS apparatus to be fitted with a microlensed fiber and a submicron precision positioner, making the upgrade approachable.[128] Here, the microlensed fiber was used to focus the beam, producing a lateral resolution of 300 nm in HeLa cells cultured with the drugs acriflavine and azure B. A schematic of the setup is shown in Figure 7B.

Zhao et al. achieved direct quantitation of analytes at the single-cell level by introducing hydrogen flame desorption ionization MS (HFDI-MS).[129] Sampling of single plant cells from holly leaves was performed under a microscope using a pressure-assisted microsampling probe (Figure 7C). Pressure-assisted microsampling involves sucking a known volume of cellular content into the probe and manually controlling the volume by observing the meniscus in the tip. A practical schematic of the sampling probe and detailed calculations are provided in the paper and its Supporting Information. Analytes on the surface of the sample are then desorbed with the hydrogen flame, vaporized into ions, and analyzed by an ion mobility quadrupole time-of-flight mass spectrometer (IM-Q-ToF MS).

Steady progress is similarly underway in the single-cell MALDI field. Sweedler and co-workers recently presented a workflow combining MALDI-MS and immunocytochemistry (ICC) for cell-type classification.[130] The protocol involves sequential MALDI-MS and ICC, allowing the detection of many compounds that are generally removed by ICC fixation protocols but are instead easily ionized by MALDI. This workflow enabled correlative profiling of single rat cerebellar cell ICC, imaging, and mass spectra and classified them according to their lipid composition. Another publication by Sweedler and co-workers additionally elaborated on this data set which, along with others, was used in the development of a novel machine learning workflow for the classification of single

https://dx.doi.org/10.1021/acs.analchem.0c04361
Anal. Chem. 2021, 93, 41−71

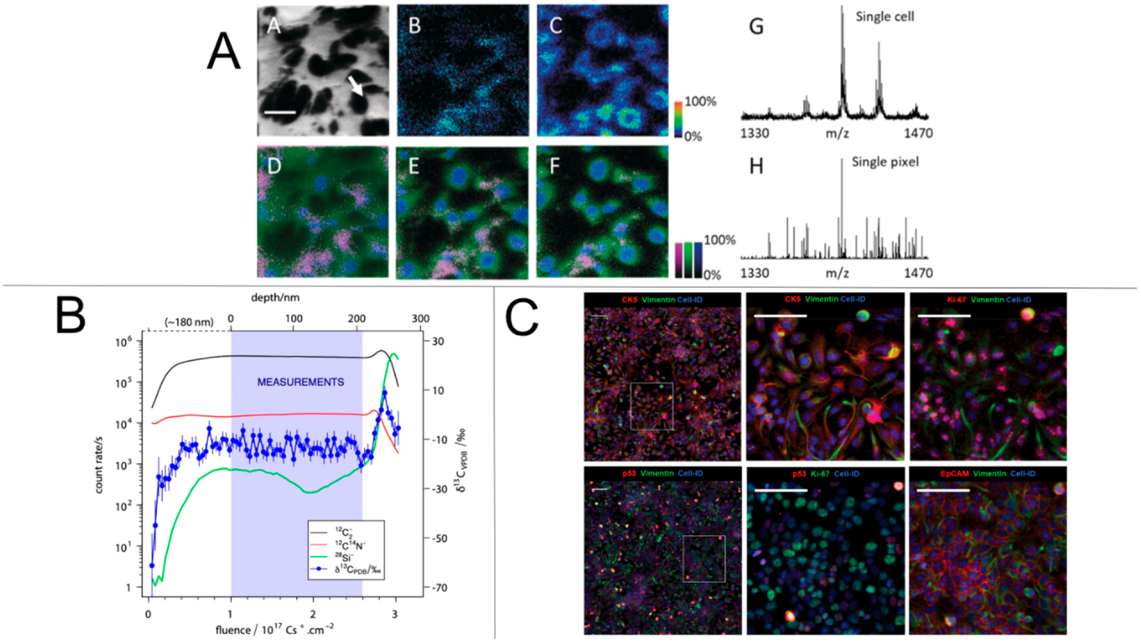

Figure 8. SIMS imaging of single cells and subcellular regions. (A) GCIB-SIMS imaging of CL in hippocampal neuronal HT22 cells at 1 μm pixel size. Cells were treated with EDC/PLC immediately prior to analysis to enhance CL signals: (*A*) SIMS first-layer total-ion current image gives the outline of HT22 cells; a representative cell is indicated by an arrow (scale bar = 50 mm), (*B*) SIMS second-layer image of cellular CL (68:2, *m*/*z* 1404.0) and (*C*) PI (38:4, *m*/*z* 885.5) to a give subcellular structure, (*D*−*F*) depth profiling of HT22 cells (*D*, first layer, surface to subsurface (0−200 nm); E, second (200−400 nm) subsurface; F, third (400−600 nm) subsurface). Panels D−F: green: PI (38:4, *m*/*z* 885.6); blue: deoxyribosediphosphate (*m*/*z* 257.0); magenta: CL (68:2, *m*/*z* 1404.0). (*G*) CL region (*m*/*z* 1330−1470) SIMS first-layer spectrum of the single cell indicated in (*A*) and of a representative single pixel (*H*) in that cell. Reprinted with permission from Tian, H.; Sparvero, L. J.; Blenkinsopp, P.; Amoscato, A. A.; Watkins, S. C.; Bayır, H.; et al. Secondary-Ion Mass Spectrometry Images Cardiolipins and Phosphatidylethanolamines at the Subcellular Level. *Angew Chemie - Int Ed.* **2019**, *58*, 3156−3161. Copyright 2019 Angewandte Chemie (ref 140). (B) $^{12}C^{14}N^-$, $^{12}C_2^-$, and $^{28}Si^-$ secondary ion count rates and $\delta^{13}C_{VPDB}$ vs Cs^+ ion dose. During the first part of sputtering, the transient state (0 to 10^{17} $Cs^+ \cdot cm^{-2}$ from 0 to ∼180 nm depth); the sputtering rate changed. At steady state (>10^{17} $Cs^+ \cdot cm^{-2}$, >∼180 nm depth), the sputtering rate was constant, and it is in this region where measurements were performed until reaching the silicon wafer. VPDB stands for the Vienna Pee Dee Belemnite standard. Reprinted from Thomen, A.; Najafinobar, N.; Penen, F.; Kay, E.; Upadhyay, PP.; Li, X.; et al. Subcellular Mass Spectrometry Imaging and Absolute Quantitative Analysis across Organelles. *ACS Nano*. **2020**, *14*, 4316 (ref 146). Copyright 2020 American Chemical Society, https://pubs.acs.org/doi/full/10.1021/acsnano.9b09804 and further permissions related to the material excerpted should be directed to the ACS. (C) Imaging mass cytometry images of cellular and nuclear markers expressed by HCC1143 with zoom-in areas (two ROI). Cell-ID: nuclei labeled with Ir-intercalator. Each zoom-in composite image is rendered with a selection of different markers. Scale bar = 100 μm. Reprinted with permission from Bouzekri, A.; Esch, A.; Ornatsky, O. Multidimensional Profiling of Drug-Treated Cells by Imaging Mass Cytometry. *FEBS Open Bio* **2019**, *9*, 1652−1669. Copyright 2019 FEBS Open Bio (ref 161). Reproduced and adapted under a Creative Commons 4.0 International License (http://creativecommons.org/licenses/by/4.0/).

cells into groups of interest (e.g., neurons vs astrocytes) according to their mass spectra.[131]

One more study by Sweedler and co-workers further investigated the lipid heterogeneity of rat cerebellar cells via microscopy-guided MALDI Fourier transform ion cyclotron resonance (FTICR) MS; this high throughput approach allowed the assay of more than 30 000 cells, from which around 520 lipid features were detected.[132] This is reportedly one of the largest number of cells profiled in a single-cell MS experiment.

MALDI-MS analysis on single cells can be hindered by matrix saline interferences, which are enhanced by the use of small and salt rich volumes such as the contents of a single cell. MALDI-MS is thus not yet commonly employed for SCMS studies. To overcome this issue, Zhang and co-workers proposed a three-phase droplet-based single-cell printing (TP-SCP) analysis system, which allows packaging, extraction, separation, and printing of single live-cell contents for subsequent MALDI-MS analysis.[133] The lipid substance of MCF-7 cells (human breast cancer cell line) was analyzed, and the performance of the technique was characterized. In principle, this method reportedly eliminates matrix effects and provides MALDI-MS native-state single-cell information.

Another novel approach combining transmission mode MALDI (t-MALDI) and post-ionization (MALDI-2) was employed by Dreisewerd et al. to image phospholipids in single Vero B4 cells (monkey renal epithelial cell line) using a pixel size as low as 600 nm.[134] So-called t-MALDI-2-MS reportedly achieved higher subcellular spatial resolution and higher sensitivity compared to conventional top-illumination t-MALDI and MALDI-2-MS for the samples in question.

Mass Spectrometry Based on Secondary Ion Mass Spectrometry. Secondary ion mass spectrometry (SIMS) is a relatively hard ionization, MS imaging method, which has shown promising applications in SCMS thanks to its potential for high spatial resolution, sensitivity, specificity, and multiplex analysis. In SIMS, a sample surface is bombarded with a focused primary ion beam, which sputters neutral and charged analytes off the surface of the sample; secondary ions are extracted by an electric field into a mass spectrometer and separated according to their mass-to-charge (*m*/*z*) ratios. These ions then reach a detector, and a mass spectrum of

https://dx.doi.org/10.1021/acs.analchem.0c04361
Anal. Chem. 2021, 93, 41−71

signal intensity versus m/z is generated for each ion species. Since the sample is scanned spot-by-spot and a mass spectrum is generated for each spot, an image is produced that reveals the spatial distribution of the elements and molecules across a sample surface according to their relative intensity. The two main platforms of SIMS are ToF-SIMS and nanoscale SIMS (NanoSIMS). Thorough details on the principles of SIMS were recently reviewed by Agüi-Gonzalez et al.[135]

As we approach submicrometer level resolution MS, a few trade-offs need to be considered. For example, SIMS analysis has to be performed under vacuum, which requires samples to be chemically, cryo, or pressure fixed, and thus, it does not allow live-cell imaging. Additionally, small beam and pixel size can lead to low secondary ion yield; Li et al. approached this issue and investigated the signal enhancement effects of graphene quantum dots (GE QDs) as matrix material using ToF-SIMS.[136] While NanoSIMS uses a magnetic sector mass analyzer and a high energy focused beam, ToF-SIMS utilizes a time-of-flight mass analyzer and either a pulsed primary or secondary beam. ToF-SIMS is a generally label-free, non-targeted technique, and lateral resolution can be down to approximately 100 nm. In the study by Li et al.,[136] both lipids and amiodarone were imaged in single MCF-7 cells using a Bi_3^+ primary ion beam, and both endogenous and exogenous species (lipids and amiodarone) were subject to significant signal enhancement. This result promotes the potential for GE QDs in research on drug metabolism pathways and interactions in single cells.

Cumpson and co-workers similarly investigated the effects of water cluster primary ion beams for enhancing secondary ion yield in ToF-SIMS and reported a many-fold enhancement for positive and negative molecular ions.[137] This builds on previous literature showing that positive ion yields benefit from the presence of added water during SIMS analysis such as from the use of water clusters as a primary ion beam.[138,139]

More research is continuously underway to evolve SIMS primary ions beams and accommodate different analysis requirements. The introduction of gas cluster ion beams (GCIB) allows lower chemical damage and a relatively softer ionization compared to other SIMS beam types (such as mono- and polyatomic beams), thus enabling the detection of higher-mass molecular ions. Winograd and co-workers recently presented the development of a unique version of high-voltage CO_2 GCIB.[140] In short, the beam reportedly lead to an unprecedented spatial resolution of 1−1.6 μm for intact lipid imaging at the cellular and subcellular level in single HT22 cells (hippocampal neuronal cell line) using a direct current beam buncher-ToF-SIMS (Figure 8A). Further analyses (e.g., immunohistochemistry and depth profiling) were performed and were described to further characterize beam performance and sample features. Pareek et al. then used this GCIB to study the subcellular distribution of intact molecular ions of purine biosynthetic pathway intermediates and end nucleotides in HeLa cells.[141]

While relative quantification using SIMS has been previously explored, absolute quantification still represents a challenge.[142−145] This is partly due to a lack of instrument standards and the uncommon use of complementary techniques. In a recent paper, Thomen et al. presented a novel approach to directly measure the absolute concentration of an isotopically labeled drug directly from a NanoSIMS image.[146] In addition, the optimization of NanoSIMS parameters, such as the secondary ion emission steady state (Figure 8B), was discussed. This study was also thoroughly explored in a perspective by Kraft and co-workers.[147]

Together with high sensitivity and mass resolution, NanoSIMS currently features a spatial resolution down to approximately 50 nm (lateral) and 10 nm (depth), and it is therefore on the way to becoming one of the most useful single-cell analysis methods in MSI. It also finds many applications in the biogeochemistry and marine environment fields, and it is used to study how single-cell and oligocellular organisms such as phytoplankton, algae, and bacteria metabolize and respond to environmental changes. Recently, Arandia-Gorostidi et al. described the cell-specific response to the uptake of isotopic C and N of two bacterial groups (*Rhodobacteraceae* and *Flavobacteria*) under controlled temperature alterations;[148] although with some limitations, which are discussed by the authors, this study suggests that temperature changes in the environment significantly impact some types of bacterial communities. Schoffelen et al. developed a NanoSIMS-based approach to assess the role of single-cell dissolved inorganic uptake for bacterial growth in combination with cellular CO_2 and N_2 fixation and assessed the toxicity of the projected P availability rise in the Baltic Sea.[149] Berthelot et al. investigated the C and N uptake strategies of some types of marine phytoplankton at the single-cell level using NanoSIMS and flow cytometry cell sorting.[150] This is reportedly the first study reporting this combination of a cell-specific contribution in these organisms and reconciles previous conflicting reports on the topic. Dekas et al. used FISH-NanoSIMS to describe the metabolic lifestyle (chemoautotrophic or heterotrophic) of some archaea and bacteria marine populations by screening C and N isotopic changes in a vast number of individual cells.[151]

Mass Spectrometry Based on Inductively Coupled Plasma. Broadly, in inductively coupled plasma-based mass spectrometry (ICP-MS), a sample is aerosolized and carried into an ICP by an inert gas, and analysis is performed by MS. ICP-MS is traditionally used for the determination of the atomic composition of inorganic materials, but it has seen a growing association with the field of cell biology. Within its expanding biological applications, ICP-MS has seen advancements in single-cell studies thanks to research into improving the sensitivity and resolution of the technique. Aerosol dispersion has been reduced, and signal-to-noise ratios have been improved, which enables single-cell discrimination and makes analysis and subcellular imaging via ICP-MS not only possible but also advantageous. Thorough reviews specifically about ICP-MS and single-cell analysis have been recently published.[152,153]

There are two ways in which cells can be introduced into the ICP, that is either by spraying whole single cells from a suspension via conventional pneumatic nebulization where they are then vaporized and ionized by the plasma ("single-cell", SC-ICP-MS) or by directly aerosolizing single or multi cells deposited on a glass slide by plasma laser ablation ("laser ablation", LA-ICP-MS).

LA-ICP-MS can be used for imaging, but for some types of single-cell analysis, single spot analysis (laser ablation of one single cell) has been shown to be sufficient and provides better signal-to-noise ratio and higher throughput.[154] The use of custom array systems can be effective in this type of technique. Jakubowski and co-workers employed this principle and tested a novel automated single spot LA-ICP-TOF-MS using a single-cell piezo-acoustic microarrayer to optically detect individual cells, generate droplets containing single cells, and dispense

https://dx.doi.org/10.1021/acs.analchem.0c04361
Anal. Chem. 2021, 93, 41−71

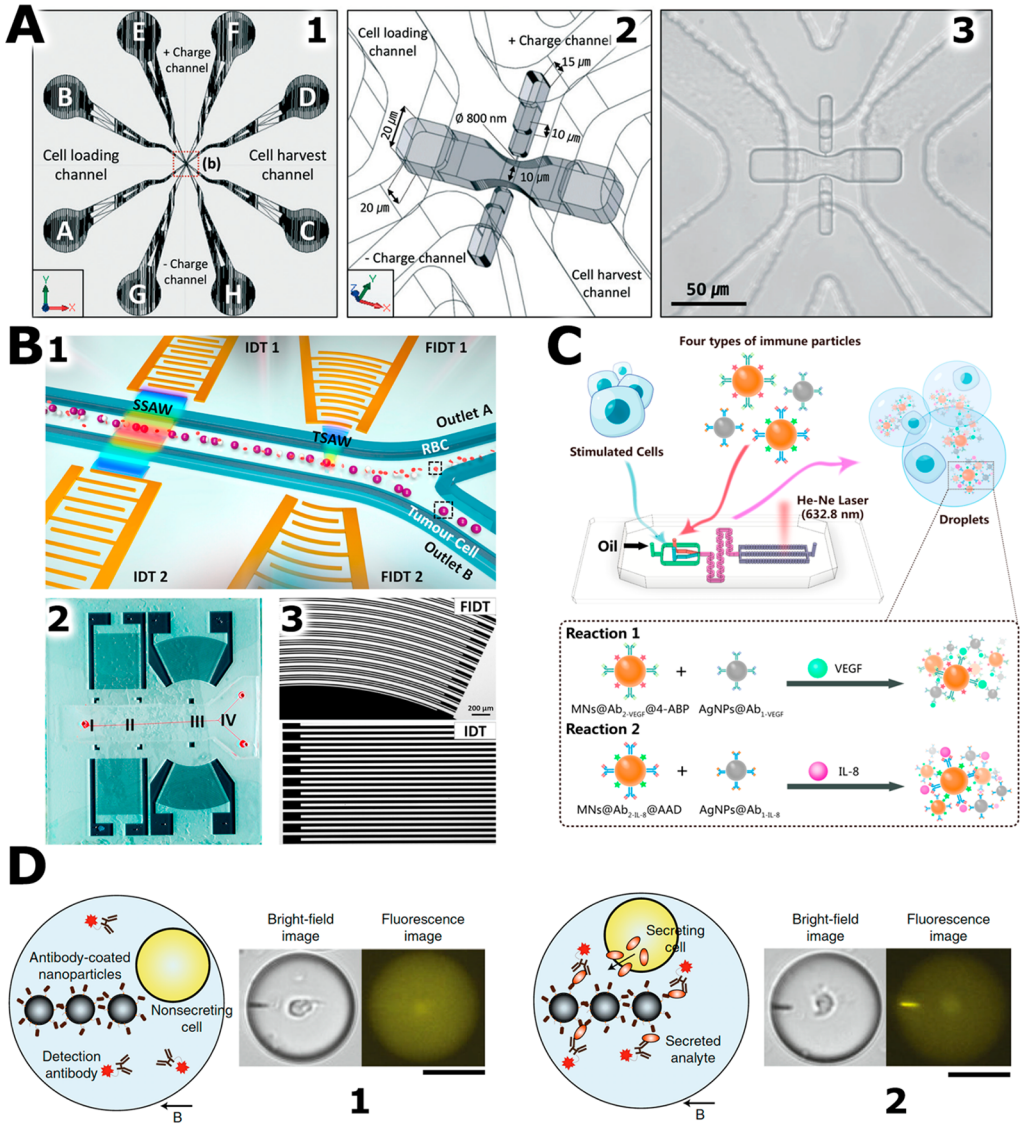

Figure 9. Examples of microfluidic devices for single-cell trapping and analysis. (A) Device for the injection of controlled volumes into single cells: (1) Schematic representation of the chip layout showing cell loading and harvest channels as well as channels used for electroporation and electrokinetic pumping of factors into a cell. (2) Schematic representation of the area marked with a (b) in (1), showing the microfluidic channels, single-cell trap, and nanoinjection channels. (3) A single human mesenchymal stem cell trapped in the device. Adapted from Yun, C. K.; Hwang, J. W.; Kwak, T. J.; Chang, W. J.; Ha, S.; Han, K.; Lee, S.; Choi, Y. S. Nanoinjection System for Precise Direct Delivery of Biomolecules into Single Cells. *Lab Chip* **2019**, *19* (4), 580−588 (ref 179), with permission from the Royal Society of Chemistry. (B) A device for separating U87 glioma cells and red blood cells (RBCs). (1) Schematic of the device layout showing the straight interdigital transducers (IDTs) that generate standing surface acoustic waves (SSAWs) and the focused interdigital transducers (FIDTs) that generate traveling pulsed surface acoustic waves (TSAWs) along the channel through which the cell suspension is led. (2) Photograph of the device showing regions (I−IV) at which the cell samples could be monitored in the acoustic wave fields. (3) Micrographs of the microfabricated IDTs and FIDTs. Reprinted from *Sensors Actuators B: Chemical, 258*, Wang, K.; Zhou, W.; Lin, Z.; Cai, F.; Li, F.; Wu, J.; Meng, L.; Niu, L.; Zheng, H., Sorting of Tumour Cells in a Microfluidic Device by Multi-Stage Surface Acoustic Waves, 1174−1183, Copyright (2018), with permission from Elsevier (ref 193). (C) On-chip measurement of cytokine secretion by single cells. Stimulated single cells were encapsulated together with four types of nanoparticles coated: two particles coated with VEGF- or IL-8-specific antibodies and two magnetic nanoparticles with VEGF- or IL-8-specific antibodies as well as two distinct Raman reporter molecules. If cells secreted one or both cytokines, conglomerates based on antibody recognition and magnetic attraction are formed. This was then detected using a He−Ne laser and spectrometer as a change in the surface-enhanced Raman spectrum. Adapted from Sun, D.; Cao, F.; Xu, W.; Chen, Q.; Shi, W.; Xu, S. Ultrasensitive and Simultaneous Detection of Two Cytokines Secreted by Single Cell in Microfluidic Droplets via Magnetic-Field Amplified SERS. *Anal. Chem.* **2019**, *91* (3), 2551−2558 (ref 209). (D) In the device presented by Bounab et al., single cells are encapsulated in aqueous droplets with 300 nm-diameter magnetic nanoparticles functionalized with antibodies specific for a specific cytokine as well as fluorescently labeled detection antibodies. (1) If the cell is nonsecreting, the fluorescence from the detection antibodies is distributed homogeneously throughout the droplet. Yet, when the cell does secrete cytokines, these antibodies are captured by the magnetic beads. Since the magnetic beads are aligned in a magnetic field (direction indicated with the arrow labeled "B" in the figure), fluorescence is localized, which can be quantitatively assessed using microscopy. Adapted from Bounab, Y.; Eyer, K.; Dixneuf, S.; Rybczynska, M.; Chauvel, C.; Mistretta, M.; Tran, T.; Aymerich, N.; Chenon, G.; Llitjos, J. F.; Venet, F.; Monneret, G.; Gillespie, I. A.; Cortez, P.; Moucadel, V.; Pachot, A.; Troesch, A.; Leissner, P.; Textoris, J.; Bibette, J.; Guyard, C.; Baudry, J.; Griffiths, A. D.; Védrine, C. Dynamic Single-Cell Phenotyping of Immune Cells Using the Microfluidic Platform DropMap. *Nat. Protoc.* **2020**, *15*, 2920−2955 (ref 203).

https://dx.doi.org/10.1021/acs.analchem.0c04361
Anal. Chem. 2021, 93, 41−71

them onto an array.[155] Microarraying and subsequent LA-ICP-MS were thus performed on THP-1 cells (a human leukemia cell type) to detect naturally occurring isotopes as fingerprints of individual cells. The microarray procedure was optimized for cell concentration, cell occupancy, and array throughput. The technique was found to not be cell-size dependent, unlike conventional nebulization ICP-MS. Among other observations, this method was described to be convenient for the quantitative determination of single-cell isotopic content with a low detection limit (down to 100 attograms) and a valid alternative to conventional LA-ICP-MS.

Zheng et al. developed a high-throughput method for LA-ICP-MS single-cell analysis also comprising a microwell array.[156] This was used to study AgNP uptake in single 16HBE cells (human normal bronchial epithelial cells) and showed that biological responses to Ag exposure varied on an individual cell basis. This suggested that great insights into biological effects of metallic NP can be achieved next using LA-ICP-MS.

Research into NP uptake and distribution in single cells has seen further attention in this field. Pisonero et al. investigated the analytical potential of nanosecond sector field LA-ICP-Sector Field(MS) (ns-LA-ICP-SFMS).[157] Elemental distribution images of NIH73T3 fibroblast cells (mouse embryonic cells) and HeLa cells incubated with AuNPs and Cd-based QDs were obtained in a fast (50 μm/s) and highly spatially resolved (2.5 μm lateral resolution) manner, providing insights into the uptake and aggregation distribution of Au and Cd within fixed single cells. Mass cytometry (MC) has also been employed for NP studies. MC, introduced in 2009, combines ICP-MS with traditional cytometry principles.[158] In this technique, suspended cells are exposed to antibodies conjugated with isotopically labeled heavy metals; the antibodies label selected proteins, and ICP-MS analysis is then performed. López-Serrano Oliver et al. used MC to establish a novel MC-based procedure to detect and quantify NPs in single THP-1 cells using a calibration method based on the transmission efficiencies of NPs.[159] In this study, an MC-specific calibration procedure was developed to absolutely quantify NPs in single cells.

A new MC approach was recently presented by Zhang and co-workers.[160] MC was coupled to conventional ESI-MS, and it gave rise to a label-free MC method termed CyESI-MS. This method provided high-coverage and high-throughput (38 cell/min) cell-to-cell metabolic heterogeneity determination; it was also used to classify several types and subtypes of cancer cell lines, and it is reported as a promising tool for biological applications at the single-cell level.

Imaging mass cytometry (IMC), a recently developed approach, couples MC with laser ablation. Cells are exposed to the isotopically labeled tagged antibodies, and a sample surface is scanned with a laser; the resulting ions are then analyzed with ICP-MS and assembled into an image, which describes the spatial subcellular configuration of proteins in a single cell. Bouzekri et al. created an open source-based workflow for IMC data analysis of drug-treated cells, providing a tool for cell population screening and drug response research (Figure 8C).[161]

More recent studies using ICP-MS have been reported, expanding the applicability and capabilities of ICP-MS to single cells.[162−165] For example, Van Acker et al. evaluated the potential of LA-ICP-MS as a highly resolving imaging and single-cell analysis technique for the localization and quantification of membrane receptors of two human breast cancer cell lines.[166] The method was correlated and compared to fluorescence confocal microscopy, which provided similar results, thus validating the performance of LA-IPC-MS for the study of targeting vectors in the precision medicine field.

MICROFLUIDICS

Interest in microfluidic or lab-on-a-chip technology within the field of single-cell analysis has remained high.[167] The increasing accessibility of microfabrication techniques has allowed more researchers to work with lab-on-a-chip technology and use its inherent advantages. As was highlighted in some recent reviews, microfluidics is becoming more commonly applied in various areas within the field of single-cell analysis, e.g., on-chip extraction and trace element analysis,[168] microbiology,[169] and cancer[170] and omics[171] research.

Advanced microfabrication techniques can be used to create geometric and fluidic features within chips that allow precise capturing and manipulation (e.g., moving, sorting) of specific cells. For chemical analysis, sample preparation can be performed *on-chip* (e.g., reagent mixing, cell lysis, micro-extraction). The analysis itself can be performed either *off-chip* using external instruments (e.g., microscopy setups, mass spectrometers) or *on-chip* (e.g., integrated sensors). Since individual analytical units on microfluidic chips are highly miniaturized, increased throughput is often achieved by designing complex chip architectures containing many units that can be operated in parallel.

In this section, the use of microfluidics for the capture and manipulation of single cells will be illustrated using recent examples. Furthermore, microfluidics-assisted sample preparation and analyses will be discussed.

Trapping and Sorting. Microfluidic devices for chemical analysis of single cells generally revolve around the capturing or trapping of cells. This is often combined with further manipulation steps that allow precise placement or sorting of cells. This trapping and sorting can be achieved by various means, including the use of geometrical features, hydrodynamic flow patterns, or microdroplets or by exerting magnetic, acoustic, or dielectrophoretic forces on cells. We cover a series of these and highlight four in Figure 9 including a device for the injection of controlled volumes into single cells (Figure 9A), a device for separating tumor and red blood cells (Figure 9B), a device for on-chip measurement of cytokine secretion by single cells (Figure 9C), and a device where single cells can be encapsulated in aqueous droplets with 300 nm-diameter magnetic nanoparticles functionalized with antibodies specific for specific cytokines and fluorescently labeled detection antibodies.

Geometrical and Gravitational Trapping and Sorting. Cells can be trapped or forced into a specific place on a chip (e.g., a cavity or microwell) by using geometrical features that obstruct or constrict the flow path of a cell suspension or allow single cells to sediment in microwells. Cama et al. reported a microfluidic device for the study of antibiotic accumulation in individual *E. coli* Gram-negative bacteria.[172] The device consisted of a two-layer channel structure made of the biocompatible and gas-permeable poly(dimethylsiloxane) (PDMS), which was covalently bonded to a glass coverslip. The channel structure comprised a larger channel, through which cells or medium could be flowed in, lined with smaller side channels in which bacteria could grow. By flowing in an

https://dx.doi.org/10.1021/acs.analchem.0c04361
Anal. Chem. 2021, 93, 41−71

autofluorescent antibiotic solution during different metabolic states (e.g., stationary or growing) and using fluorescent microscopy, both drug dosage and intracellular drug accumulation could be monitored in hundreds of individual cells.

The device presented by Lee et al. similarly used a glass bottom in combination with a microfluidic PDMS top part, yet here, yeast (*S. cerevisiae*) cells were trapped in 4 μm-high gaps underneath 50 × 25 μm "micropads".[173] A microfluidic concentration gradient generator delivered 7 different dilutions of a stimulus to 14 culture chambers. Each culture chamber was equipped with an array of 60 micropads with each pad trapping 5−15 budding yeast cells. As the cells were trapped in a single focal plane, individual cells could be tracked and imaged using fluorescence microscopy in response to serial dilutions. The device was used to monitor the relocation of effectors associated with the activation of mitogen-activated protein kinase (MAPK) pathways, which sense pheromones, stress signals, or mediate meiosis. Stratz et al. also studied *S. cerevisiae*.[174] Their PDMS-glass chip used a system of 32 geometrical single-cell traps, surrounded by ring-shaped valves. After cells were injected and most traps were occupied, the outer valves were closed, confining the volume around each cell to 11.8 nL. A gap in the ring allowed the diffusion-based exchange of medium, and in this configuration, cells could grow in the absence of shear stress. Using the chip and live-cell microscopy, growth rates were monitored under normal or oxidative stress conditions. In a different experiment, the inner ring-shaped valve surrounding single trapped cells was actuated to confine the volume around each cell to 230 pL. Lysis buffer, the enzyme diaphorase, and its substrate resazurin were then added to each cell, after which β-nicotinamide adenine dinucleotide phosphate (NADPH) levels were assessed fluorometrically. Due to the low volume (and thus low dilution of reagents), a limit of detection of 10 amol of NADPH per analysis chamber was realized.

Zhang et al. designed a highly complex, PDMS-based system that allowed independent programming of culturing conditions (including exposure to chemical stimuli) in 1500 culture chambers or microwells. These could be equipped with single cells or 2/3D cell cultures that were cultured for up to 1 week.[175] Individual cells were tracked and imaged using live-cell fluorescence microscopy, which allowed them to monitor protein localization and gene expression dynamics in single cells. The system was used to study the importance of the timing and sequence of growth factors that decide the fate of differentiating neural stem cells in a highly multiplexed fashion.

A device presented by Fatsis-Kavalopoulos et al. could be operated in two modes.[176] In "cell-trapping mode", three single cells could be isolated from an injected cell suspension in geometrical traps. In "cell-ejecting mode", these cells could then be released from the traps and directed to adjacent chambers (one for each trap). This procedure of trapping with subsequent release into the adjacent chambers was used to control the creation of clusters of different cancer cells in the chambers. As a proof of principle, 4-cell clusters of three human breast cancer cells (MCF7 and MDA-MB-231) and one murine pancreatic β-cell MIN6 were created. Calcium imaging was performed and used to study calcium dynamics in the cancer cells in response to ATP release by the adjacent β-cells.

The Lee group discussed two devices directed at the separation and trapping of specific cells from blood. In Lee et al., a PDMS-glass device was used to filter out red blood cells (RBCs), while trapping white blood cells (WBCs) and leukemia cells (THP-1, Jurkat, and K562 cell lines) in 1600 single-cell traps.[177] After diluting to 2% hematocrit with phosphate-buffered saline (PBS), blood was loaded into the chip, and a microfluidic prefilter prevented cell aggregates from continuing into the trapping part. Small RBCs then continued down the main channel toward the outlet of the device, while similarly sized leukemia cells and WBCs were filtered out and trapped in microstructures lining the channel. Using a phasor approach to fluorescence lifetime imaging microscopy (FLIM), changes in free/bound NADH were observed as an indication of metabolic change. This allowed the researchers to distinguish trapped leukemia cells (which display higher ratios of free/bound NADH) from WBCs as well as different leukemia cells from each other. In a second paper, another device presented by Lee et al. expanded on this concept.[178] Here, human U937 monocytes (a type of WBC) were separated from diluted blood in which they were spiked at a 1:1000 dilution. Similar to the other device from the Lee group, RBCs and small WBCs were first filtered out in the microfiltration structure with target monocytes ending up in a second, downstream trapping structure. Then, live U937 monocytes were separated from unwanted cells using a combination of hydrophoretic focusing (via ridges in the channel) and chevron-shaped dielectrophoresis (DEP) electrodes. Finally, U937 monocytes were trapped in the single-cell traps with good viability (84.8%) and a capturing efficiency of 83.2% when using a 20 V potential for the DEP separation.

Yun et al. developed a microfluidic nanoinjection system that allowed for the confinement of a single cell in a narrow, geometrical trap (Figure 9A).[179] After loading through a PDMS channel, cells were in contact with a 800 nm-diameter microfabricated glass capillary. An electric field was triggered to allow electroporation of the cell membrane as well as electrokinetic pumping of factors into the cell. The pulse width of this trigger could be modulated to control the injected volume. Monitoring of the procedure was done using fluorescent microscopy. After the injection, cells were ejected from the trap by redirecting flow and harvested for further experiments. In this study, the effective and controlled injection of red fluorescent protein and plasmid DNA into human mesenchymal stem cells was demonstrated with a maintenance of viability (>95%). However, improvements toward higher throughput are necessary, as the presented device can trap and inject only one cell at a time.

The device presented by Liu et al. consisted of a serpentine PDMS channel lined with geometrical traps.[180] Due to a gap in each trap, cells are hydrodynamically manipulated into the confinement. When a trap is occupied, the next cell will not be forced into this trap but progress to the next empty trap. The device consists of 1000 traps, and after optimization of the dimensions in the channel and traps, a >90% single-cell capture rate for Jurkat (human T lymphocyte cell line) and MCF-7 cells was achieved within 2 min. The trapped cells were observed using fluorescence microscopy and maintained good viability.

He et al. published a PDMS-glass device bonded to a tissue culture dish.[181] Here, up to 48 geometrical traps were used to capture single cells. After filling of the traps, the flow of medium was reversed to eject the cells from the traps into adjacent culture chambers. The same (now empty) traps were used to capture a different cell type, which was then ejected to

https://dx.doi.org/10.1021/acs.analchem.0c04361
Anal. Chem. 2021, 93, 41−71

the same culture chamber. Using three different cell types (oral squamous carcinoma and lymphatic endothelial cells), triple single-cell capture and ejection into the culture chambers were achieved. The total operation of the device took less than 21 min, and triple single-cell capture efficiency was close to 50%. Each cell type was stained with different dyes to allow the recognition in the culture chambers, allowing cell motility studies using fluorescence microscopy. No chemical analysis application was shown.

Hydrodynamic Trapping and Sorting. Although the nomenclature is not used consistently in the literature, we consider hydrodynamic trapping to mean contact-less manipulation of cells using fluid flows. Chiang et al. used hydrodynamic trapping to manipulate single bone marrow stem cells into U-shaped PDMS weirs, where they could be cultured and monitored using fluorescence microscopy.[182] The device consisted of 96 trapping units along a central cell loading channel. Due to the hydrodynamic flows within the trapping units, cells end up in a V-shaped weir as opposed to the U-shaped "dwelling" weir. After cells are loaded in the V-shaped weir, the flow is reversed to allow single cells to enter the dwelling weir. Using repeated loading and flow-reversal steps, a single-cell capture efficiency of 64% was achieved. Single cells were perfused with minimal shear stress and imaged for 48 h to monitor cellular dynamics (e.g., growth, adherence, migration, death).

Many microfluidic devices oriented toward single-cell analysis find applications in the study of (rare) circulating tumor cells (CTCs). These are cells released from primary tumors into the bloodstream of patients and can cause metastasis. Pei et al. presented microfluidic enrichment and purification of CTCs from whole blood and subsequent single-cell analysis.[183] Label-free CTC enrichment from whole blood was achieved by injecting the sample through a spiraling channel. Due to centrifugal force, unfocused RBCs were thus ejected from the PDMS-glass chip, while CTCs and WBCs entered a larger chamber featuring carefully placed micropillars. This array of micropillars controls the trajectory of particles or cells based on diameter. The enrichment steps resulted in a throughput of 5 mL whole blood/3 h, 92% cell sorting purity, and 96% viability. The purified CTCs were collected and labeled for phenotypic biomarkers *off-chip*. The labeled cells were then injected into the analysis microchip, which was also equipped with a micropillar array. This process was used to wash off unbound fluorescent labels before the labeled CTCs were interrogated using fluorescence spectroscopy, allowing quantitative monitoring of clinically relevant protein markers. This was done using blood from tumor-bearing mice as well as human colorectal cancer patients. The CTC phenotype was found to be related to clinical tumor stages and treatment response. Kwon et al. also employed a spiral-shaped channel, which was used to purify suspensions of Chinese hamster ovary cells (CHO cells).[184] Due to centrifugal force, nonviable cells were ejected from the device. Although this was not very efficient (3.5−28.0% removal efficiency), purity (83.6−88.3%) and live-cell retention (97.8−99.8%, 80% viability) was high using a cell suspension with 4×10^6 cells/mL. Although no analytical application was shown, the device could be used to improve the viability of cell suspensions used as a preparatory step for downstream single-cell analysis.

Droplet-Based Trapping and Sorting. Droplet microfluidics has many advantages when applied to single-cell trapping, sorting, and analysis: encapsulated cells are often easily manipulated through channels, fused with reagents, or interrogated in an inherently small volume. Babahosseini et al. described the on-chip generation, storage, manipulation, and merging of droplets from that storage within a single, multilayer PDMS device.[185] A microvalve was actuated to control the size and generation of pL-volume aqueous droplets at a T-junction generator, which were dispersed in an oil phase. These droplets were then sorted by droplet size by controlling the size of the geometric traps using pneumatic microvalves. Droplets could then be ejected from the traps toward a merging chamber and fused with other droplets. Human skin fibroblasts were encapsulated in droplets, trapped, and merged successfully. Yu et al. also employed a T-junction in a PDMS-glass device to generate water-in-oil droplets.[186] Here, yellow fluorescent protein (YFP)-modified *M. polymorpha* protoplasts (plant cells without a cell wall) were encapsulated. The autofluorescence of chlorophyll or the YFP reporter protein was quantified using a confocal microscope with a throughput of 115 200 individual cells per hour. A second device combined the droplet generation with electrodes generating dielectrophoretic force, triggered if the fluorescence intensity of an encapsulated protoplast exceeded a set threshold. If triggered, the droplet is then forced into a specific channel, allowing on-chip fluorescence assisted cell sorting (FACS).

The device presented by Shen et al. allows researchers to monitor the release of the reactive oxygen species hydrogen peroxide (H_2O_2) from single cells.[187] For this, Au nanoclusters were conjugated with horseradish peroxidase (HRP) to generate fluorescent HRP−Au nanoclusters. The fluorescence of these clusters is quenched in a dose-dependent manner by H_2O_2 and can be quantified using fluorescence microscopy. By encapsulating the clusters together with single cells in the microdroplets, a sufficient limit of detection (circa 1 nM) can be achieved to monitor the minute amounts of H_2O_2 released by cells. Droplets were generated at a rate of 43 s^{-1} using a polyether ether ketone (PEEK) microfluidic T-junction. Single-cell encapsulation efficiency was 33%. Four cell types with different levels of reactive oxygen species (human HUVEC (human umibilical vein endothelial cells), MCF7 and U937 cells, and murine Mut6 cells) were encapsulated with HRP−Au nanoclusters, allowing the H_2O_2 release to be monitored.

T cells expressing engineered T cell receptors (TCR T) are used in cancer immunotherapy. Segaliny et al. developed a device that can assist in finding the right TCR Ts by studying the interaction of these cells with target tumor antigens at the single-cell level.[188] For this, a PDMS microfluidic device was developed that allowed the coencapsulation of Jurkat-based TCR T cells and target cells into aqueous droplets in a continuous oil phase (about 20% efficiency). The cells were engineered to express eGFP upon interaction with target cells, whereas multiple interactions lead to more expression. After encapsulation, thousands of microdroplets were trapped in 10 368 microwells lining the ceiling of a second PDMS device due to the buoyancy of the aqueous droplets. Fluorescence microscopy was then used to assess the interaction of the coencapsulated, trapped cells. If TCR T cells showed a good interaction with the target cells, a laser was used to heat up the oil in that microwell. This created a bubble, forcing the droplet from the microwell, after which it was washed off the chip for downstream analysis (PCR, sequencing). The encapsulated cells showed good viability for up to 9 h in the microwell array.

https://dx.doi.org/10.1021/acs.analchem.0c04361
Anal. Chem. 2021, 93, 41−71

Guo et al. presented a different way of manipulating the droplets.[189] Their system consisted of a glass, hydrophobic microchip with a hydrophilic micropillar array. The chip was covered in oil and placed on an $x-y-z$ translation stage. On top of the pillars, aqueous droplets of reagents or samples could be loaded using solid, hydrophobic pins of which only the tip was hydrophilic. The system also allowed for fusion of droplets using the pin. The diameter of the pillars and tip determined the droplet volume (fL to nL volumes). The droplets could be interrogated using a fluorescence microscopy setup. A single-cell analysis application was shown by first seeding droplets containing a human hepatic HepG2 cancer cell suspension on 50 μm-diameter pillars (about 60% probability of a single cell on a micropillar). Subsequently, lysis buffer and fluorescein di-β-D-galactopyranoside were added to each droplet using the pin. After 30 min of incubation, the activity of β-galactosidase in each cell was measured using the fluorescence microscopy setup. An element of concern, especially with smaller droplet volumes ($\geq$pL), is evaporation. The researchers implemented several measures to mitigate this, e.g., introduction of a "water moat" surrounding the micropillar array and presaturation of the oil with water.

Other Techniques for Trapping and Sorting. Beyond the categories listed above, there have been reports of other techniques for trapping and sorting of single cells on microfluidic chips. Wu et al. published a device relying on DEP force for separation, trapping, and manipulation of single yeast cells.[190] At the bottom of a PDMS microchannel, actuation electrodes generated DEP barriers. These were used to separate polystyrene microbeads and yeast cells flowing in the channel, directing their flow path as they passed the actuation electrodes (90% separation efficiency). The microbeads and cells were then trapped on an array of wireless circular bipolar microelectrodes by controlling the distribution of the electric field (single yeast cell occupancy of 72% using a cell density of 800 cells/μL). This system of bipolar electrodes also allowed the cells to be rotated and propelled along the electric field with a velocity of 94.2 μm/min. No analytical application was shown. Li and Anand used a very similar bipolar electrode-based DEP approach yet added functionality allowing on-chip cell lysis.[191] Their PDMS-based chip featured 48 trapping sites along a main channel with wireless bipolar electrodes extending 5 μm into the main channel. By turning the electrical field on, MDA-MB-231 was trapped with an 81.2% single-cell capture rate. By switching the field off and then on again, the cells were then transferred to an attached, slightly larger microchamber (88.0% transfer efficiency). The cell suspension in the main channel was exchanged with hydrophobic ionic liquid to fluidically isolate the microchambers. By increasing the AC field strength, the cells were lysed.

In a publication from the same group, DEP-based cell trapping and manipulation were combined with gene expression analysis.[192] Here, K562 leukemia cells were injected into one of two main PDMS microchannels, lined with a thin film metallic electrode. Using the electrodes, an electric field was generated to trap cells based on DEP (single-cell capture efficiency of 91.7%). Then, loop-mediated isothermal amplification (LAMP) buffer was added, flushing away excess cells and forcing trapped single cells into adjacent microchambers. The LAMP buffer was then exchanged for oil to fluidically isolate the microchambers, after which the cells were thermally lysed. By measuring the fluorescence of each microchamber, the expression of the oncogene BCR-ABL could be monitored in single cells.

Wang et al. chose a different contact-less cell manipulation method and used surface acoustic waves to separate human U87 glioma cells from red blood cells (Figure 9B).[193] Here, a 65 μm-diameter PDMS channel was lined by two pairs of electrodes for generating acoustic waves: interdigital transducers (IDTs) for generating standing surface acoustic waves and focused interdigital transducers (FIDTs) for generating traveling pulsed surface acoustic waves. Cells were flowing through the channel, while the IDTs generated a wavelength of 130 μm. This led to the cells being focused at pressure nodes in the center of the microfluidic channel. Further down the channel, the FIDTs allowed for separation of the cells into two channels. Using this approach, 90% of U87 cells were separated from red blood cells. The cells maintained good short- and long-term viability, as was assessed using immunofluorescence staining with Calcein AM and propidium iodine and cell proliferation experiments, respectively.

Although the silicon–borosilicate glass device first presented by Nitta and co-workers is microfluidic, the automated operation of the device relied on computer vision.[194,195] Here, cells were first hydrodynamically 3D-focused into a single stream using sheath flows surrounding the cell suspension. Over the course of the microchannel, the cells were interrogated using high-resolution, high-speed multicolor frequency-division-multiplexed fluorescence microscopy. Image analysis was performed using either a classical algorithm or convolutional neural network (deep learning). During the analysis, the stream of cells was maintained through acoustic focusing while flowing to the actual sorting section of the chip. Here, piezoelectric actuators manipulated dual membrane pumps, diverting the stream (and cells) into one of three channels. The position of the membrane pumps is decided on the basis of the analysis of the images of intracellular molecular localization and cell morphology. Total sorting took 32 ms. Although the method is similar to FACS in some ways, it has the advantage of using multidimensional images instead of the unidimensional fluorescence intensity measurements used in FACS. The setup was shown to be effective in identifying highly rare EpCAM (CD326) CTCs in a blood sample for a pancreatic cancer patient. It was also used to show sorting of algal *Chlamydomonas reinhardtii* exhibiting abnormal protein localization, sorting 2000 mutants out of 200 000 cells within 4 min. Sorting 255 platelet aggregates from 6000 human blood cells was performed in <1 min. Currently, the technology allows only 100 "events per second", but this is limited by available computing power, which is expected to improve in the future.

Sample Analysis. After describing the various techniques researchers have at their disposal for the trapping, sorting, and manipulation of cells in microfluidic devices, we will now highlight some recent examples of (on-chip) analyses of single cells.

Sequencing and Expression Analyses. The study of genes and expression of genes at the level of the individual cell can provide detailed information on single-cell status and heterogeneity of the cell population. With the help of various types of microfluidics, single-cell RNA or DNA analysis can be achieved. Although several commercial platforms are available,[196] improvements and new approaches are still being published. Xu et al. reported a digital microfluidics platform for single-cell mRNA sequencing.[197] In digital microfluidics,

https://dx.doi.org/10.1021/acs.analchem.0c04361
Anal. Chem. 2021, 93, 41−71

researchers move around aqueous droplets in a minute, oil-filled space between two parallel plates. This is achieved by applying the principle of electrowetting-on-dielectric (EWOD): applying specific voltages allows the moving, merging, splitting of the droplets with control over droplet volume. In their platform, the researchers isolated single cells in droplets on hydrophilic spots on the otherwise hydrophobic plates of the device. These droplets were then merged with cell lysis buffer and reverse transcriptase polymerase chain reaction (RT-PCR) reagents, after which the complementary DNA (cDNA) was amplified. After removal of the sample from the chip, sequencing was performed *off-chip* and used to reveal the presence of rare genes and expression heterogeneity in populations of murine embryonic stem cells (MEF) and fibroblasts.

Another example of microfluidics-assisted single-cell RT-PCR was presented by Kim et al.[198] Here, cells were also encapsulated in droplets but dispersed in a continuous oil phase flowing through a PDMS microchannel. Single cells, Jurkat and MC7 (human breast cancer cell line), were encapsulated in 100 pL droplets containing alkaline lysis buffer. After incubation for 30 s in a microfluidic delay line, the droplets were merged with RT-PCR reagent droplets, which neutralized the alkaline lysis buffer. The droplets were then harvested, and their target mRNA (CD45) was amplified in a thermal cycle off-chip. In this manner, ∼50 000 single-cell RT-PCR droplets could be generated within 20 min. Finally, the droplets were assessed using fluorescence microscopy to identify CD45-expressing cells.

Sarma et al. presented a diffusion-based approach to cell lysis, reverse transcription, and cDNA amplification.[199] Their design consisted of a two-layer PDMS device, containing microfluidic structures and two parallel, 80 pL reaction chambers in one layer and pneumatic microvalves in another. After trapping single cells (MEF and GM12878 (human lymphoblastoid)) in the reaction chamber, lysis reagents were allowed to diffuse into the chamber. Using the valves, the chamber was closed, and lysis was performed for 3 min at 72 °C. After this, RT reagents were allowed to diffuse into the chamber over 40 min, followed by PCR reagents. After amplification of the cDNA under thermal cycling, the products were harvested and sequenced off-chip using standard benchtop methods. The microfluidic platform was compared to state-of-the-art single-cell RNA-sequencing platforms and found to be sensitive, precise, and accurate although the throughput of the system needs to be improved. The authors indicated that their platform is scalable, which might decrease processing time significantly.

High-throughput, droplet-based single-cell RNA-sequencing platforms often employ molecular "barcoding" of captured mRNA in order to track individual cells or genes after amplification and bulk sequencing. The technique presented by Bioč anin et al. is presented as an improvement of the popular Drop-seq platform.[200] Drop-Seq is based on the coencapsulating of single cells with barcoded RNA primers attached to solid microbeads. Two of the major drawbacks of the Drop-seq technique are its incompatibility with air pressure-driven pumping systems and a significant loss of barcoded beads during the capturing step. In their work, the researchers combined two PDMS microfluidic devices, operable via syringe or pressure-driven pumps: an encapsulation chip and a bead capture and processing chip. This allowed researchers to significantly improve efficiency (up to 93%) compared to the original protocol, especially if cDNA generation was also performed on-chip. The researchers showed the use of several cell types in their system and confirmed the metric performance of the system was comparable to the original protocol.

The highly scalable platform Hydro-Seq was presented by Cheng et al.[201] Oriented toward the transcriptome analysis of single CTCs, it was also intended as an improvement on the Drop-seq protocol, again targeting the bead loss seen in the original protocol. The PDMS-based device consisted of ∼1 nL capture chambers. Here, CTCs were size-separated from cellular and acellular debris in the original sample, trapped, and paired with barcoded beads. Lysis buffer was then loaded into the chambers in order to extract mRNA. Control valves ensured selective closing and opening of the flow paths of the cells, beads, and washing and lysis buffer. After extraction, the beads were retrieved from the chip and used for downstream procedures (reverse transcription, amplification, sequencing). At the end of the on-chip procedures, 73% of the initially loaded cells were successfully paired with barcoded beads. To demonstrate clinical relevancy, Hydro-Seq was validated by performing transcriptome analysis on 666 CTCs from samples of 21 breast cancer patients. The authors indicate the chamber array (which is currently composed of 800 chambers) can be expanded to thousands of chambers.

A device presented by Marie et al. was made by injection-molding the polymer TOPAS 5013.[202] It featured 8 geometrical single-cell traps lining a main channel. After the cells were trapped, lysis buffer was introduced. DNA was then harvested for genome-wide amplification and off-chip sequencing using (commercial) multiple displacement amplification. The device was validated using several colorectal cancer-derived cell lines and fresh colorectal tumor samples in two different laboratories (99% overlap of the obtained DNA sequences with a reference genome). The authors state that their approach is highly flexible, as it only performs DNA extraction from single cells, making it compatible with commercial amplification protocols. Furthermore, they speculate their platform could be used as a clinical tool for the personalization of oncolytic chemotherapy if cells from the patient's own tumor are used for genome analysis.

On-Chip Immunoassays. Microfluidic devices can be used for the phenotyping of single cells using on-chip immunoassays. We discuss three recent examples of on-chip immunoassays for the measurement of cytokine and antibody secretion by individual cells. Bounab et al. presented a droplet-based platform: DropMap (Figure 9D).[203] The platform consists of a microfluidic chip that allows the encapsulation of individual cells in 50 pL droplets, which are then collected as a 2D array. The cells are encapsulated together with fluorescently labeled detection antibodies and 300 nm-diameter magnetic nanoparticles functionalized with capturing antibodies. The magnetic nanoparticles are aligned in a single file in a magnetic field. If the cell does not secrete the analyte of interest, fluorescence is homogeneously distributed in the droplet. If the cell does secrete proteins to which the detection antibodies are specific, they are captured on the magnetic beads. This results in a localization of the fluorescence at these beads, allowing high-throughput dynamic and quantitative measurement of cell secretion using microscopy. DropMap was used to measure the secretion of the cytokine tumor necrosis factor-alpha (TNF-α), interferon-gamma (IFN-γ), interleukin 2 (IL-2), and interleukin 4 (IL-4) from single human T-cells as well as TNF-α

https://dx.doi.org/10.1021/acs.analchem.0c04361
Anal. Chem. 2021, 93, 41−71

secretion from human single monocytes from healthy donors and septic shock patients and immunoglobin G antibody secretion from murine B-cells. Limits of detection for the cytokines using this system were on the order of 0.2 to 10.4 nM. A system using a very similar approach was presented by Gérard et al. for the study of antibody diversity as generated by individual cells.[204] However, here, the droplets were analyzed *in-flow*, after which they were sorted using DEP and harvested. By performing single-cell barcoded reverse transcription in the droplets, antibody-coding genes could be sequenced.

Herrera et al. discuss the use of a similar on-chip sandwich immunoassay for the detection of TNF-α secretion by single cells.[205] To facilitate the assay, luminescent quantum dots were first modified with tetrazine after which they were conjugated with detection antibodies, modified with trans-cyclooctene. The cycloaddition product has a small footprint, allowing multiple nanoparticles to attach to a single protein target, which amplifies the signal. Human U-937 cells were seeded into ∼350 pL PDMS microwells and treated with lipopolysaccharide. The wells were then closed off with a glass detection slide coated with TNF-α-specific antibodies. After 24 h, detection slides were removed, stained with the immunoconjugated quantum dots, and imaged using fluorescence microscopy. Using their approach, the researchers were able to lower the threshold for the detection of TNF-α to 60 aM, corresponding to about 1.3 molecules per cell.

The glass device developed by Nakao et al. consisted of both micro- and nanofluidic components (the latter employing channel dimensions on the order of 100−1000 nm).[206] By modifying the nanofluidic channel structures using hydrophilic, hydrophobic, antibody, and blocking coatings, an on-chip enzyme-linked immunosorbent assay (ELISA) for interleukin 6 (IL-6) secretion by single Raji cells (a human B-lymphocyte cell line) was realized. The device used a total of 13 operating units and nine pumps to control nine reagents. A single cell could be selected from a 400-cell microfluidic chamber using optical tweezers. After selection, the cell was chemically stimulated and isolated by introducing an air−liquid interface. The supernatant was then aspirated using a fL-scale nanopipette for volumetry. To decrease viscosity, the sample was diluted and transported to the ELISA channel, where reactions with immobilized antibodies occurred. After the formation of a colored substrate, detection was done using differential interference contrast-thermal lens microscopy. For their method, the researchers found a detection limit of 5 molecules of IL-6, and using it, they measured the IL-6 secretion rate of stimulated B-cells to be 3 molecules/min.

Other Microfluidics-Assisted Analyses. Sibbitts et al. presented a device that is aimed at the detection of nitric oxide (NO) by single cells.[207] NO is produced by microglia in the brain as an inflammatory signaling molecule under pathological conditions (e.g., neurodegenerative diseases). Due to cellular heterogeneity and NO's short half-life, the measurement is challenging. A PDMS device with two optical fibers was used: one located at the intersection of the cell seeding channel and an electrophoretic separation channel with the second at the end of the separation channel. SIM-A9 cells (microglial cell line) were labeled with a fluorescent NO probe and an internal standard and stimulated with LPS and IFN-γ with and without exposure to an inhibitor of NO synthesis (1400 W dihydrochloride). A suspension of these cells was then inserted and transported through the microfluidic cell loading channel using on-chip pumping. When the first optical fiber detected a cell, a strong electrical field was used to lyse the cell. Then, the contents of the cell were electrophoretically separated with fluorescence peaks detected via the second optical fiber. The researchers report a 56% increase in NO production in stimulated vs nonstimulated cells. The cells that were exposed to the inhibiting compound and stimulated produced 47% less NO compared to untreated cells and 18% in nonstimulated cells.

A device presented by Li et al. is aimed at the detection of cytokine secretion by single cells, using a gold, plasmonic nanohole array (NHA)-based biosensor.[208] It is housed in a two-layer (fluidic and pumping) microfluidic chip, fabricated using injection molding. The biosensor operates on the principal of extraordinary optical transmission (EOT), which occurs when light is transmitted through the subwavelength-diameter nanoholes, resulting in detection of EOT resonance peaks in the transmission spectrum. Very small changes in refractive index will change the location of these peaks in the spectrum. After functionalizing the surface with IL-2 antibodies, this phenomenon was exploited to create an IL-2 plasmonic biosensor (39 pg/mL sensitivity). The application of the device was shown by injecting EL4 lymphoma cells and trapping several of these cells on the biosensors' surface in valve-gated chambers. The device was then placed in an inverted microscope with control over temperature, CO_2, and humidity. Using the microscope, EOT spectra could be obtained at individual cells. After stimulation, IL-2 secretion could thus be monitored over time. However, since the biosensor was uniformly extended over the entire chip, spatial diffusion analysis was also realized. The analysis of data obtained with the device from many individual EL4 cells allowed the researchers to study heterogeneity in secretion capacity.

Sun et al. also studied the secretion of cytokines, in this case vascular endothelial growth factor (VEGF) and interleukin 8 (IL-8) (Figure 9C).[209] Here, droplet microfluidics and the detection of cytokines using surface-enhanced Raman spectroscopy (SERS) were employed. After stimulation with PMA, individual MDA-MB-231, A549 (lung cancer cell line), and SGC (gastric cancer cell line) cells were encapsulated in aqueous droplets and dispersed in an oil phase flowing through a microchannel (20% single-cell encapsulation). The cells were coencapsulated with four different types of nanoparticles: two Ag particles modified with VEGF- or IL-8-specific antibodies and two magnetic nanoparticles with VEGF- or IL-8-specific antibodies as well as two distinct Raman reporter molecules. When the cells secrete VEGF and/or IL-8, aggregates are formed on the basis of the antibody recognition and magnetic attraction. Using a spectrometer aimed at a detection site on the chip, this was then detected as a change in the SERS spectrum and related to VEGF and/or IL-8 secretion. With a sensitivity of 1 fg/mL, the simultaneous detection of VEGF and IL-8 secretion was achieved. It was found that SGC and A549 secreted more VEGF than IL-8 with measurements on MDA-MB-231 cells showing the opposite. In a paper from the same group, Sun et al. used a very similar approach for the analysis of alkaline phosphatase (ALP) expression in individual cells.[210] ALP is a biomarker used in the diagnosis of biliary and skeletal diseases. This is a common indicator used for the diagnosis of biliary and skeletal diseases. In contrast to the previous example, cell encapsulation in droplets was performed on a separate chip. Single HepG2 cells were encapsulated with Au nanoparticles and 5-bromo-4-chloro-3-indolyl phosphate

https://dx.doi.org/10.1021/acs.analchem.0c04361
Anal. Chem. 2021, 93, 41−71

(BCIP) and collected. BCIP can be specifically converted by ALP; the oxidized product of this reaction is a Raman-active compound that can be measured using SERS (LOD = 1×10^{-15} M). After incubation with BCIP for 2 h, the droplets were injected into the detection chip. Here, three parallel channels could harbor 100 cell-containing droplets in a single file before analysis with a spectrometer. Finally, the SERS spectra were analyzed to assess ALP activity in the cells. The application of the system was shown for HepG2 (hepatic cancer cell line) and BNL.CL (a noncancer liver cell line). It was found that noncancer cells show 40% less ALP activity than the HepG2 cells. The system was also used to monitor the dynamic, concentration-dependent effects of the ALP-inhibiting compounds sodium orthovanadate and sorafenib.

A final example of the application of SERS for the chemical analysis of single cells was presented by Zhang et al.[211] Here, a PDMS chip was used to separate and trap breast cancer cells from 10× diluted blood based on size (capture rate of 87%, 93%, and 87% for SKBR3, MCF7, and MDA-MB-231, respectively). A cocktail of three different types of Au/Ag nanostructures, each modified with one of three distinct Raman reporters, was prepared. Each type was also modified with aptamers to be specific for human epidermal growth factor receptor 2 (HER2), epithelial cell adhesion molecule (EpCAM), or human epidermal growth factor receptor (EGFR). SERS measurements were then performed to assess the interaction between the Raman-reporting nanostructures with each target analyte on individual cells. The data were analyzed to classify the different cell types based on their expression of HER2, EpCAM, and EGFR with high sensitivity and selectivity.

We finish this section with two examples of microfluidics-assisted single-cell mass spectrometry (MS). Huang et al. demonstrated the detection of phosphatidylcholines in single cells of different cell lines (U87, HepG2, HUVEC, and Caco-2 (human colorectal cancer cell line)).[212] For this, a simple PDMS-based cell trap was made in which a single cell could be captured. The cell was then lysed, and its (surface) contents were extracted using methanol, after which the extraction mixture was analyzed using an electrospray quadrupole time-of-flight mass spectrometer. The data were used to characterize and identify the human cell lines on the basis of their phospholipid expression profiles. However, challenges remain, as heterogeneity between cells of the same cell line affected the identification process.

Zhou et al. presented a device that used a NH_4HCO_3 buffer as a continuous phase in which cells could be dispersed and flown through a PDMS-based microfluidic chip.[213] The chip featured an array of microposts to filter out cell debris and facilitate the generation of a single file of cells. By controlling the flow of buffer, the interval between cells ending up at the outlet could be controlled. The outlet was connected to a homemade micronebulizer that was used to infuse single cells into an inductively coupled plasma quadrupole-based mass spectrometry (ICP-qMS) system for elemental analysis. During infusion, the buffer was decomposed at 95 °C. HeLa (human cervical cancer cell line) and RAW264.7 (murine macrophage cancer cell line) cells were analyzed for intrinsic Zn concentration as well as Au concentration after exposure to Au nanoparticles. Of the total cell throughput of 1080 cells per min, 72% and 82% of HeLa cells could be analyzed for Au and Zn, respectively, and 81% and 78% of RAW264.7 cells could be analyzed for Au and Zn, respectively. Zn concentrations were found to be 34 and 33 fg/cell in HeLa and RAW264.7 cells, respectively. After exposure to Au nanoparticles, the Au concentration in RAW264.7 cells was much higher than in HeLa cells (136 vs 6 fg/cell), which the researchers attributed to the phagocytic properties of the macrophage-type RAW264.7 cells.

AUTHOR INFORMATION

Corresponding Author

Andrew G. Ewing − *Department of Chemistry and Molecular Biology, University of Gothenburg, 41296 Gothenburg, Sweden;* orcid.org/0000-0002-2084-0133; Email: andrew.ewing@chem.gu.se

Authors

Keke Hu − *Department of Chemistry and Molecular Biology, University of Gothenburg, 41296 Gothenburg, Sweden*

Tho D. K. Nguyen − *Department of Chemistry and Molecular Biology, University of Gothenburg, 41296 Gothenburg, Sweden*

Stefania Rabasco − *Department of Chemistry and Molecular Biology, University of Gothenburg, 41296 Gothenburg, Sweden*

Pieter E. Oomen − *Department of Chemistry and Molecular Biology, University of Gothenburg, 41296 Gothenburg, Sweden; ParaMedir B.V., 9301 LK Roden, The Netherlands*

Complete contact information is available at: https://pubs.acs.org/10.1021/acs.analchem.0c04361

Author Contributions

[§]K.H., T.D.K.N., S.R., and P.E.O. contributed equally to this work. K.H., T.D.K.N., S.R., and P.E.O. worked on the electrochemistry, super-resolution microscopy, mass spectrometry, and microfluidics, respectively. K.H. organized the internal writing effort.

Notes

The authors declare no competing financial interest.

Biographies

Keke Hu is a postdoctoral researcher at the Department of Chemistry and Molecular Biology at the University of Gothenburg, Sweden. She obtained a dual Ph.D. degree from Beijing Institute of Technology and the Graduate Center of the City University of New York. Her research focuses on nanoscale electrochemistry, electrochemical methodology, single-cell electrochemistry, and neurochemistry.

Tho D. K. Nguyen is currently a Ph.D. student at the Department of Chemistry and Molecular Biology, University of Gothenburg, Sweden. She received her B.Sc. degree in pharmacy from the University of Medicine and Pharmacy, Ho Chi Minh City, Vietnam, in 2014. From 2014 to 2016, she worked as a research assistant at the Clinical Pharmacology Laboratory, Oxford University Clinical Research Unit, Vietnam, developing analytical methods for therapeutic drug monitoring. She obtained her M.Sc. degree (2018) in analytical chemistry from Uppsala University, Sweden, and the University of Tartu, Estonia, via a two-year Erasmus Mundus joint master's program (Excellence in Analytical Chemistry-EACH). She joined the research group of Andrew Ewing in 2018. Her research interests include the application and development of NanoSIMS imaging and STED microscopy incorporating electrochemistry techniques for the studies of exocytosis and stress granules.

Stefania Rabasco is currently a Ph.D. student at the University of Gothenburg. She received her B.Sc. degree in chemistry from the University of Brighton in 2017 and her M.Sc. degree in chemistry in

https://dx.doi.org/10.1021/acs.analchem.0c04361
Anal. Chem. 2021, 93, 41−71

environmental forensics from Örebro University in 2018. Her research focuses on using mass spectrometry imaging (NanoSIMS) to investigate subcellular structures in single cells.

Pieter E. Oomen is a is a researcher and entrepreneur specialized in (bio)sensing and microfluidics. He received his B.Sc. (2009) and M.Sc. (2012) degrees in pharmacy from the University of Groningen, The Netherlands. He obtained his Ph.D. degree in analytical chemistry and microfluidics at the same university in 2016. After a brief postdoc there and subsequently working as a researcher in industry for 9 months, he joined the group of Andrew Ewing at the University of Gothenburg, Sweden, as a postdoc in 2017, continuing his research with a Marie Skłodowska-Curie Individual Fellowship. He is currently working in The Netherlands with the Dutch biotechnology company ParaMedir, which he cofounded. His research interests include the study of biomarkers and pharmacological phenomena and further development of (bio)sensors and microfluidics.

Andrew G. Ewing is Professor of Chemistry and Molecular Biology at the University of Gothenburg, Sweden, and is currently also Academician Professor at Shenzhen University in China. He received his B.S. from Saint Lawrence University in Canton, NY and his Ph.D. at Indiana University in Bloomington, IN with R. Mark Wightman. He was a postdoc in the laboratory of Royce Murray at the University of North Carolina. He is a Knut and Alice Wallenberg Scholar (2011−2023), an elected member of the Royal Swedish Academy of Sciences, class 4 (chemistry), Nobel Class (2012), and the Gothenburg Academy of Arts and Sciences (2013). His research focuses on the neuronal process of exocytosis pioneering small-volume chemical measurements at single cells and the contents of individual nanometer vesicles in cells.

■ ACKNOWLEDGMENTS

We acknowledge the many co-workers that have come before us and whose works we cite in this Review. We acknowledge support from the European Research Council (ERC Advanced Grant), the Knut and Wallenberg Foundation in Sweden, the Swedish Research Council (VR), and the USA National Institutes of Health (NIH).

■ REFERENCES

(1) Wightman, R. M.; Jankowski, J. A.; Kennedy, R. T.; Kawagoe, K. T.; Schroeder, T. J.; Leszczyszyn, D. J.; Near, J. A.; Diliberto, E. J.; Viveros, O. H. *Proc. Natl. Acad. Sci. U. S. A.* **1991**, *88* (23), 10754−10758.
(2) He, X.; Ewing, A. G. *J. Am. Chem. Soc.* **2020**, *142* (29), 12591−12595.
(3) Gu, C.; Zhang, X.; Ewing, A. G. *Anal. Chem.* **2020**, *92* (15), 10268−10273.
(4) Tang, Y.; Yang, X. K.; Zhang, X. W.; Wu, W. T.; Zhang, F. L.; Jiang, H.; Liu, Y. L.; Amatore, C.; Huang, W. H. *Chem. Sci.* **2020**, *11* (3), 778−785.
(5) Li, X.; Majdi, S.; Dunevall, J.; Fathali, H.; Ewing, A. G. *Angew. Chem.* **2015**, *127* (41), 12146−12150.
(6) Roberts, J. G.; Mitchell, E. C.; Dunaway, L. E.; McCarty, G. S.; Sombers, L. A. *ACS Nano* **2020**, *14* (3), 2917−2926.
(7) Zhu, W.; Gu, C.; Dunevall, J.; Ren, L.; Zhou, X.; Ewing, A. G. *Angew. Chem.* **2019**, *131* (13), 4282−4286.
(8) Taleat, Z.; Larsson, A.; Ewing, A. G. *ACS Chem. Neurosci.* **2019**, *10* (4), 2060−2069.
(9) Majdi, S.; Larsson, A.; Najafinobar, N.; Borges, R.; Ewing, A. G. *ACS Chem. Neurosci.* **2019**, *10* (5), 2459−2466.
(10) Gu, C.; Larsson, A.; Ewing, A. G. *Proc. Natl. Acad. Sci. U. S. A.* **2019**, *116* (43), 21409−21415.
(11) Larsson, A.; Majdi, S.; Oleinick, A.; Svir, I.; Dunevall, J.; Amatore, C.; Ewing, A. G. *Angew. Chem.* **2020**, *132* (17), 6777−6780.
(12) Yue, Q.; Li, X.; Wu, F.; Ji, W.; Zhang, Y.; Yu, P.; Zhang, M.; Ma, W.; Wang, M.; Mao, L. *Angew. Chem.* **2020**, *132* (27), 11154−11158.
(13) Amatore, C.; Arbault, S.; Bouton, C.; Coffi, K.; Drapier, J. C.; Ghandour, H.; Tong, Y. *ChemBioChem* **2006**, *7* (4), 653−661.
(14) Hu, K.; Li, Y.; Rotenberg, S. A.; Amatore, C.; Mirkin, M. V. *J. Am. Chem. Soc.* **2019**, *141* (11), 4564−4568.
(15) Zhang, X.; Oleinick, A.; Jiang, H.; Liao, Q.; Qiu, Q.; Svir, I.; Liu, Y.; Amatore, C.; Huang, W. *Angew. Chem.* **2019**, *131* (23), 7835−7838.
(16) Pan, R.; Hu, K.; Jia, R.; Rotenberg, S. A.; Jiang, D.; Mirkin, M. V. *J. Am. Chem. Soc.* **2020**, *142* (12), 5778−5784.
(17) Wang, Y.; Feng, H.; Zhang, H.; Chen, Y.; Huang, W.; Zhang, J.; Jiang, X.; Wang, M.; Jiang, H.; Wang, X. *Analyst* **2020**, *145* (4), 1294−1301.
(18) Vaneev, A. N.; Gorelkin, P. V.; Garanina, A. S.; Lopatukhina, H. V.; Vodopyanov, S. S.; Alova, A. V.; Ryabaya, O. O.; Akasov, R. A.; Zhang, Y.; Novak, P.; Salikhov, S. V.; Abakumov, M. A.; Takahashi, Y.; Edwards, C. R. W.; Klyachko, N. L.; Majouga, A. G.; Korchev, Y. E.; Erofeev, A. S. *Anal. Chem.* **2020**, *92* (12), 8010−8014.
(19) Zhou, M.; Jiang, Y.; Wang, G.; Wu, W.; Chen, W.; Yu, P.; Lin, Y.; Mao, J.; Mao, L. *Nat. Commun.* **2020**, *11* (1), 1−9.
(20) Ding, S.; Li, M.; Gong, H.; Zhu, Q.; Shi, G.; Zhu, A. *Anal. Chem.* **2020**, *92* (3), 2543−2549.
(21) Xu, M.; Pan, R.; Zhu, Y.; Jiang, D.; Chen, H. Y. *Anal. Chem.* **2018**, *90* (17), 10117−10121.
(22) Chen, W.; Ding, S.; Wu, J.; Shi, G.; Zhu, A. *Chem. Commun.* **2020**, *56*, 13225−13228.
(23) Shen, M.; Qu, Z.; Deslaurier, J.; Welle, T. M.; Sweedler, J. V.; Chen, R. *J. Am. Chem. Soc.* **2018**, *140* (25), 7764−7768.
(24) Ying, Y. L.; Hu, Y. X.; Gao, R.; Yu, R. J.; Gu, Z.; Lee, L. P.; Long, Y. T. *J. Am. Chem. Soc.* **2018**, *140* (16), 5385−5392.
(25) Jiang, H.; Qi, Y. T.; Wu, W. T.; Wen, M. Y.; Liu, Y. L.; Huang, W. H. *Chem. Sci.* **2020**, *11* (33), 8771−8778.
(26) Dunevall, J.; Fathali, H.; Najafinobar, N.; Lovric, J.; Wigström, J.; Cans, A. S.; Ewing, A. G. *J. Am. Chem. Soc.* **2015**, *137* (13), 4344−4346.
(27) Pan, R.; Hu, K.; Jiang, D.; Samuni, U.; Mirkin, M. V. *J. Am. Chem. Soc.* **2019**, *141* (50), 19555−19559.
(28) Barlow, S. T.; Zhang, B. *Anal. Chem.* **2020**, *92* (16), 11318−11324.
(29) Zhang, X. W.; Hatamie, A.; Ewing, A. G. *J. Am. Chem. Soc.* **2020**, *142* (9), 4093−4097.
(30) Hu, K.; Jia, R.; Hatamie, A.; Long, K. L. V.; Mirkin, M. V.; Ewing, A. G. *J. Am. Chem. Soc.* **2020**, *142* (40), 16910−16914.
(31) Marquitan, M.; Mark, M. D.; Ernst, A.; Muhs, A.; Herlitze, S.; Ruff, A.; Schuhmann, W. *J. Mater. Chem. B* **2020**, *8* (16), 3631−3639.
(32) Yang, X. K.; Tang, Y.; Qiu, Q. F.; Wu, W. T.; Zhang, F. L.; Liu, Y. L.; Huang, W. H. *Anal. Chem.* **2019**, *91* (23), 15123−15129.
(33) Wang, Y.; Fathali, H.; Mishra, D.; Olsson, T.; Keighron, J. D.; Skibicka, K. P.; Cans, A. S. *J. Am. Chem. Soc.* **2019**, *141* (44), 17507−17511.
(34) Marquitan, M.; Ruff, A.; Bramini, M.; Herlitze, S.; Mark, M. D.; Schuhmann, W. *Bioelectrochemistry* **2020**, *133*, 107487.
(35) Liao, Q. L.; Jiang, H.; Zhang, X. W.; Qiu, Q. F.; Tang, Y.; Yang, X. K.; Liu, Y. L.; Huang, W. H. *Nanoscale* **2019**, *11* (22), 10702−10708.
(36) Voci, S.; Goudeau, B.; Valenti, G.; Lesch, A.; Jović, M.; Rapino, S.; Paolucci, F.; Arbault, S.; Sojic, N. *J. Am. Chem. Soc.* **2018**, *140* (44), 14753−14760.
(37) Liu, G.; Jin, B. K.; Ma, C.; Chen, Z.; Zhu, J. J. *Anal. Chem.* **2019**, *91* (9), 6363−6370.
(38) Zhang, J.; Jin, R.; Jiang, D.; Chen, H. Y. *J. Am. Chem. Soc.* **2019**, *141* (26), 10294−10299.
(39) Li, L.; Liu, K.; Fang, D. *Electroanalysis* **2020**, *32* (5), 958−963.
(40) Cui, C.; Chen, Y.; Jiang, D.; Chen, H. Y.; Zhang, J.; Zhu, J. J. *Anal. Chem.* **2019**, *91* (1), 1121−1125.

https://dx.doi.org/10.1021/acs.analchem.0c04361
Anal. Chem. 2021, 93, 41−71

(41) Zhang, J.; Ding, H.; Zhao, S.; Jiang, D.; Chen, H. Y. *Electrochem. Commun.* **2019**, *98*, 38−42.
(42) Chen, A.; Liang, W.; Wang, H.; Zhuo, Y.; Chai, Y.; Yuan, R. *Anal. Chem.* **2020**, *92* (1), 1379−1385.
(43) Zhang, H.; Gao, W.; Liu, Y.; Sun, Y.; Jiang, Y.; Zhang, S. *Anal. Chem.* **2019**, *91* (19), 12581−12586.
(44) Wang, Y.; Jin, R.; Sojic, N.; Jiang, D.; Chen, H. *Angew. Chem.* **2020**, *132* (26), 10502−10506.
(45) Xia, J.; Zhou, J.; Zhang, R.; Jiang, D.; Jiang, D. *Anal. Bioanal. Chem.* **2018**, *410* (20), 4787−4792.
(46) Jin, L.; Liu, B.; Zhao, F.; Hahn, S.; Dong, B.; Song, R.; Elston, T. C.; Xu, Y.; Hahn, K. M. *Nat. Commun.* **2020**, *11* (1), 1934.
(47) Grußmayer, K. S.; Geissbuehler, S.; Descloux, A.; Lukes, T.; Leutenegger, M.; Radenovic, A.; Lasser, T. *Nat. Commun.* **2020**, *11* (1), 3023.
(48) Dreier, J.; Castello, M.; Coceano, G.; Cáceres, R.; Plastino, J.; Vicidomini, G.; Testa, I. *Nat. Commun.* **2019**, *10* (1), 556.
(49) Klevanski, M.; Herrmannsdoerfer, F.; Sass, S.; Venkataramani, V.; Heilemann, M.; Kuner, T. *Nat. Commun.* **2020**, *11* (1), 1552.
(50) Alvelid, J.; Testa, I. *Curr. Opin. Biomed. Eng.* **2019**, *12*, 34−42.
(51) Oomen, P. E.; Aref, M. A.; Kaya, I.; Phan, N. T. N.; Ewing, A. G. *Anal. Chem.* **2019**, *91* (1), 588−621.
(52) Sahl, S. J.; Hell, S. W.; Jakobs, S. *Nat. Rev. Mol. Cell Biol.* **2017**, *18*, 685−701.
(53) Schermelleh, L.; Ferrand, A.; Huser, T.; Eggeling, C.; Sauer, M.; Biehlmaier, O.; Drummen, G. P. C. *Nat. Cell Biol.* **2019**, *21* (1), 72−84.
(54) Chong, W. M.; Wang, W. J.; Lo, C. H.; Chiu, T. Y.; Chang, T. J.; Liu, Y. P.; Tanos, B.; Mazo, G.; Tsou, M. F. B.; Jane, W. N.; Yang, T. T.; Liao, J. C. *eLife* **2020**, *9*, 1−21.
(55) Wang, C.; Taki, M.; Sato, Y.; Tamura, Y.; Yaginuma, H.; Okada, Y.; Yamaguchi, S. *Proc. Natl. Acad. Sci. U. S. A.* **2019**, *116* (32), 15817−15822.
(56) Virant, D.; Traenkle, B.; Maier, J.; Kaiser, P. D.; Bodenhöfer, M.; Schmees, C.; Vojnovic, I.; Pisak-Lukáts, B.; Endesfelder, U.; Rothbauer, U. *Nat. Commun.* **2018**, *9* (1), 1−14.
(57) Beliu, G.; Kurz, A. J.; Kuhlemann, A. C.; Behringer-Pliess, L.; Meub, M.; Wolf, N.; Seibel, J.; Shi, Z. D.; Schnermann, M.; Grimm, J. B.; Lavis, L. D.; Doose, S.; Sauer, M. *Commun. Biol.* **2019**, *2* (1), 261.
(58) Collot, M.; Ashokkumar, P.; Anton, H.; Boutant, E.; Faklaris, O.; Galli, T.; Mély, Y.; Danglot, L.; Klymchenko, A. S. *Cell Chem. Biol.* **2019**, *26* (4), 600−614.E7.
(59) Schlichthaerle, T.; Strauss, M. T.; Schueder, F.; Auer, A.; Nijmeijer, B.; Kueblbeck, M.; Jimenez Sabinina, V.; Thevathasan, J. V.; Ries, J.; Ellenberg, J.; Jungmann, R. *Angew. Chem., Int. Ed.* **2019**, *58* (37), 13004−13008.
(60) M'Saad, O.; Bewersdorf, J. *Nat. Commun.* **2020**, *11* (1), 1−15.
(61) Chen, F.; Tillberg, P. W.; Boyden, E. S. *Science* **2015**, *347* (6221), 543−548.
(62) Gambarotto, D.; Zwettler, F. U.; Le Guennec, M.; Schmidt-Cernohorska, M.; Fortun, D.; Borgers, S.; Heine, J.; Schloetel, J.-G.; Reuss, M.; Unser, M.; Boyden, E. S.; Sauer, M.; Hamel, V.; Guichard, P. *Nat. Methods* **2019**, *16* (1), 71−74.
(63) Chang, J.-B.; Chen, F.; Yoon, Y.-G.; Jung, E. E.; Babcock, H.; Kang, J. S.; Asano, S.; Suk, H.-J.; Pak, N.; Tillberg, P. W.; Wassie, A. T.; Cai, D.; Boyden, E. S. *Nat. Methods* **2017**, *14* (6), 593−599.
(64) Gregor, I.; Enderlein, J. *Curr. Opin. Chem. Biol.* **2019**, *51*, 74−83.
(65) Tenne, R.; Rossman, U.; Rephael, B.; Israel, Y.; Krupinski-Ptaszek, A.; Lapkiewicz, R.; Silberberg, Y.; Oron, D. *Nat. Photonics* **2019**, *13* (2), 116−122.
(66) Gustafsson, M. G. L. *J. Microsc.* **2000**, *198* (2), 82−87.
(67) Schermelleh, L.; Carlton, P. M.; Haase, S.; Shao, L.; Winoto, L.; Kner, P.; Burke, B.; Cardoso, M. C.; Agard, D. A.; Gustafsson, M. G. L.; Leonhardt, H.; Sedat, J. W. *Science (Washington, DC, U. S.)* **2008**, *320* (5881), 1332−1336.
(68) Gustafsson, M. G. L.; Shao, L.; Carlton, P. M.; Wang, C. J. R.; Golubovskaya, I. N.; Cande, W. Z.; Agard, D. A.; Sedat, J. W. *Biophys. J.* **2008**, *94* (12), 4957−4970.
(69) Manton, J. D.; Ströhl, F.; Fiolka, R.; Kaminski, C. F.; Rees, E. J. *Biomed. Opt. Express* **2020**, *11* (4), 2098.
(70) Jahr, W.; Velicky, P.; Danzl, J. G. *Methods* **2020**, *174* (4), 27−41.
(71) Lanzanò, L.; Coto Hernández, I.; Castello, M.; Gratton, E.; Diaspro, A.; Vicidomini, G. *Nat. Commun.* **2015**, *6* (1), 6701.
(72) Tortarolo, G.; Sun, Y.; Teng, K. W.; Ishitsuka, Y.; Lanzanó, L.; Selvin, P. R.; Barbieri, B.; Diaspro, A.; Vicidomini, G. *Nanoscale* **2019**, *11* (4), 1754−1761.
(73) Coelho, S.; Baek, J.; Graus, M. S.; Halstead, J. M.; Nicovich, P. R.; Feher, K.; Gandhi, H.; Gooding, J. J.; Gaus, K. *Sci. Adv.* **2020**, *6* (16), eaay8271.
(74) Xu, F.; Ma, D.; MacPherson, K. P.; Liu, S.; Bu, Y.; Wang, Y.; Tang, Y.; Bi, C.; Kwok, T.; Chubykin, A. A.; Yin, P.; Calve, S.; Landreth, G. E.; Huang, F. *Nat. Methods* **2020**, *17* (5), 531−540.
(75) Xie, L.; Dong, P.; Chen, X.; Hsieh, T. H. S.; Banala, S.; De Marzio, M.; English, B. P.; Qi, Y.; Jung, S. K.; Kieffer-Kwon, K. R.; Legant, W. R.; Hansen, A. S.; Schulmann, A.; Casellas, R.; Zhang, B.; Betzig, E.; Lavis, L. D.; Chang, H. Y.; Tjian, R.; Liu, Z. *Nat. Methods* **2020**, *17* (4), 430−436.
(76) Jungmann, R.; Avendaño, M. S.; Woehrstein, J. B.; Dai, M.; Shih, W. M.; Yin, P. *Nat. Methods* **2014**, *11* (3), 313−318.
(77) Wade, O. K.; Woehrstein, J. B.; Nickels, P. C.; Strauss, S.; Stehr, F.; Stein, J.; Schueder, F.; Strauss, M. T.; Ganji, M.; Schnitzbauer, J.; Grabmayr, H.; Yin, P.; Schwille, P.; Jungmann, R. *Nano Lett.* **2019**, *19* (4), 2641−2646.
(78) Brockman, J. M.; Su, H.; Blanchard, A. T.; Duan, Y.; Meyer, T.; Quach, M. E.; Glazier, R.; Bazrafshan, A.; Bender, R. L.; Kellner, A. V; Ogasawara, H.; Ma, R.; Schueder, F.; Petrich, B. G.; Jungmann, R.; Li, R.; Mattheyses, A. L.; Ke, Y.; Salaita, K. *Nat. Methods* **2020**, *17*, 1018−1024.
(79) Balzarotti, F.; Eilers, Y.; Gwosch, K. C.; Gynnå, A. H.; Westphal, V.; Stefani, F. D.; Elf, J.; Hell, S. W. *Science (Washington, DC, U. S.)* **2017**, *355* (6325), 606−612.
(80) Pape, J. K.; Stephan, T.; Balzarotti, F.; Büchner, R.; Lange, F.; Riedel, D.; Jakobs, S.; Hell, S. W. *Proc. Natl. Acad. Sci. U. S. A.* **2020**, *117* (34), 20607−20614.
(81) Stockhammer, A.; Bottanelli, F. *J. Phys. D: Appl. Phys.* **2021**, *54*, 033001.
(82) Wang, L.; Frei, M. S.; Salim, A.; Johnsson, K. *J. Am. Chem. Soc.* **2019**, *141* (7), 2770−2781.
(83) Kwon, J.; Park, J. S.; Kang, M.; Choi, S.; Park, J.; Kim, G. T.; Lee, C.; Cha, S.; Rhee, H. W.; Shim, S. H. *Nat. Commun.* **2020**, *11* (1), 1−11.
(84) Bozhanova, N. G.; Gavrikov, A. S.; Mishin, A. S.; Meiler, J. *Sci. Rep.* **2020**, *10* (1), 1−11.
(85) Grimm, F.; Nizamov, S.; Belov, V. N. *ChemBioChem* **2019**, *20* (17), 2248−2254.
(86) Pereira, P. M.; Gustafsson, N.; Marsh, M.; Mhlanga, M. M.; Henriques, R. *Traffic* **2020**, *21* (5), 375−385.
(87) Jang, S.; Kim, M.; Shim, S. H. *Angew. Chem., Int. Ed.* **2020**, *59* (29), 11758−11762.
(88) Belov, V. N.; Stoldt, S.; Rüttger, F.; John, M.; Seikowski, J.; Schimpfhauser, J.; Hell, S. W. *J. Org. Chem.* **2020**, *85* (11), 7267−7275.
(89) Strauss, S.; Nickels, P. C.; Strauss, M. T.; Jimenez Sabinina, V.; Ellenberg, J.; Carter, J. D.; Gupta, S.; Janjic, N.; Jungmann, R. *Nat. Methods* **2018**, *15* (9), 685−688.
(90) Sograte-Idrissi, S.; Schlichthaerle, T.; Duque-Afonso, C. J.; Alevra, M.; Strauss, S.; Moser, T.; Jungmann, R.; Rizzoli, S. O.; Opazo, F. *Nanoscale* **2020**, *12* (18), 10226−10239.
(91) Liu, Z.; Liu, J.; Wang, X.; Mi, F.; Wang, D.; Wu, C. *Bioconjugate Chem.* **2020**, *31* (8), 1857−1872.
(92) Li, J. H.; Santos-Otte, P.; Au, B.; Block, S.; Ewers, H. *Nat. Commun.* **2020**, *11*, 4259.
(93) Zhang, M.; Li, M.; Zhang, W.; Han, Y.; Zhang, Y. H. *Light Sci. Appl.* **2019**, *8*, 73.
(94) Beliu, G.; Sauer, M. *Light: Sci. Appl.* **2020**, *9* (1), 10−11.

https://dx.doi.org/10.1021/acs.analchem.0c04361
Anal. Chem. 2021, 93, 41−71

(95) Halabi, E. A.; Pinotsi, D.; Rivera-Fuentes, P. *Nat. Commun.* **2019**, *10* (1), 1−10.
(96) Bucevičius, J.; Kostiuk, G.; Gerasimaitė, R.; Gilat, T.; Lukinavičius, G. *Chem. Sci.* **2020**, *11* (28), 7313−7323.
(97) Kabatas, S.; Agüi-Gonzalez, P.; Hinrichs, R.; Jähne, S.; Opazo, F.; Diederichsen, U.; Rizzoli, S. O.; Phan, N. T. N. *J. Anal. At. Spectrom.* **2019**, *34*, 1083−1087.
(98) Kabatas, S.; Agüi-Gonzalez, P.; Saal, K. A.; Jähne, S.; Opazo, F.; Rizzoli, S. O.; Phan, N. T. N. *Angew. Chem., Int. Ed.* **2019**, *58* (11), 3438−3443.
(99) Arsić, A.; Stajković, N.; Spiegel, R.; Nikić-Spiegel, I. *Sci. Rep.* **2020**, *10* (1), 6441.
(100) Stanly, T. A.; Fritzsche, M.; Banerji, S.; Garcia, E.; De La Serna, J. B.; Jackson, D. G.; Eggeling, C. *Biol. Open* **2016**, *5* (9), 1343−1350.
(101) Richter, K. N.; Revelo, N. H.; Seitz, K. J.; Helm, M. S.; Sarkar, D.; Saleeb, R. S.; D'Este, E.; Eberle, J.; Wagner, E.; Vogl, C.; Lazaro, D. F.; Richter, F.; Coy-Vergara, J.; Coceano, G.; Boyden, E. S.; Duncan, R. R.; Hell, S. W.; Lauterbach, M. A.; Lehnart, S. E.; Moser, T.; Outeiro, T. F.; Rehling, P.; Schwappach, B.; Testa, I.; Zapiec, B.; Rizzoli, S. O. *EMBO J.* **2018**, *37* (1), 139−159.
(102) Mund, M.; Ries, J. *Mol. Biol. Cell* **2020**, *31* (19), 2093−2096.
(103) Thevathasan, J. V.; Kahnwald, M.; Cieśliński, K.; Hoess, P.; Peneti, S. K.; Reitberger, M.; Heid, D.; Kasuba, K. C.; Hoerner, S. J.; Li, Y.; Wu, Y.; Le Mund, M.; Matti, U.; Pereira, P. M.; Henriques, R.; Nijmeijer, B.; Kueblbeck, M.; Sabinina, V. J.; Ellenberg, J.; Ries, J. *Nat. Methods* **2019**, *16* (10), 1045−1053.
(104) Laine, R. F.; Tosheva, K. L.; Gustafsson, N.; Gray, R. D. M.; Almada, P.; Albrecht, D.; Risa, G. T.; Hurtig, F.; Lindås, A. C.; Baum, B.; Mercer, J.; Leterrier, C.; Pereira, P. M.; Culley, S.; Henriques, R. *J. Phys. D. Appl. Phys.* **2019**, *52* (16), 163001.
(105) Ries, J. *Nat. Methods* **2020**, *17*, 870−872.
(106) Yin, L.; Zhang, Z.; Liu, Y.; Gao, Y.; Gu, J. *Analyst* **2019**, *144* (3), 824−845.
(107) Wilm, M. S.; Mann, M. *Int. J. Mass Spectrom. Ion Processes* **1994**, *136*, 167−180.
(108) Pan, N.; Rao, W.; Kothapalli, N. R.; Liu, R.; Burgett, A. W. G.; Yang, Z. *Anal. Chem.* **2014**, *86* (19), 9376−9380.
(109) Liu, R.; Pan, N.; Zhu, Y.; Yang, Z. *Anal. Chem.* **2018**, *90* (18), 11078−11085.
(110) Zhu, Y.; Liu, R.; Yang, Z. *Anal. Chim. Acta* **2019**, *1084*, 53−59.
(111) Zhao, Y.; Chen, Z.; Wu, Y.; Tsukui, T.; Ma, X.; Zhang, X.; Chiba, H.; Hui, S. P. *Anal. Chem.* **2019**, *91* (7), 4466−4471.
(112) Standke, S. J.; Colby, D. H.; Bensen, R. C.; Burgett, A. W. G.; Yang, Z. *Anal. Chem.* **2019**, *91* (3), 1738−1742.
(113) Zhu, Y.; Wang, W.; Yang, Z. *Anal. Chem.* **2020**, *92* (16), 11380−11387.
(114) Pan, N.; Standke, S. J.; Kothapalli, N. R.; Sun, M.; Bensen, R. C.; Burgett, A. W. G.; Yang, Z. *Anal. Chem.* **2019**, *91* (14), 9018−9024.
(115) Zheng, Y.; Liu, Z.; Xing, J.; Zheng, Z.; Pi, Z.; Song, F.; Liu, S. *Talanta* **2020**, *211*, 120751.
(116) Nemes, P.; Vertes, A. *Anal. Chem.* **2007**, *79* (21), 8098−8106.
(117) Stopka, S. A.; Khattar, R.; Agtuca, B. J.; Anderton, C. R.; Paša-Tolić, L.; Stacey, G.; Vertes, A. *Front. Plant Sci.* **2018**, *9*, 1−13.
(118) Portero, E. P.; Nemes, P. *Analyst* **2019**, *144* (3), 892−900.
(119) Liao, H. W.; Rubakhin, S. S.; Philip, M. C.; Sweedler, J. V. *Anal. Chim. Acta* **2020**, *1118*, 36−43.
(120) Xu, M.; Pan, R.; Zhu, Y.; Jiang, D.; Chen, H. Y. *Analyst* **2019**, *144* (3), 954−960.
(121) Feng, J.; Zhang, X.; Huang, L.; Yao, H.; Yang, C.; Ma, X.; Zhang, S.; Zhang, X. *Anal. Chem.* **2019**, *91* (9), 5613−5620.
(122) Maiman, T. H. *Nature* **1960**, *187*, 493−494.
(123) Honig, R. E.; Woolston, J. R. *Appl. Phys. Lett.* **1963**, *2*, 138−139.
(124) Hillenkamp, F.; Unsöld, E.; Kaufmann, R.; Nitsche, R. *Appl. Phys.* **1975**, *8* (4), 341−348.
(125) Yin, Z.; Cheng, X.; Liu, R.; Li, X.; Hang, L.; Hang, W.; Xu, J.; Yan, X.; Li, J.; Tian, Z. *Angew. Chem.* **2019**, *131* (14), 4589−4594.
(126) Cheng, X.; Yin, Z.; Rong, L.; Hang, W. *Nano Res.* **2020**, *13* (3), 745−751.
(127) Cheng, X.; Wang, T.; Yin, Z.; Hang, W. *J. Anal. At. Spectrom.* **2020**, *35* (5), 927−932.
(128) Meng, Y.; Cheng, X.; Wang, T.; Hang, W.; Li, X.; Nie, W.; Liu, R.; Lin, Z.; Hang, L.; Yin, Z.; Zhang, B.; Yan, X. *Angew. Chem.* **2020**, *132* (41), 18020−18027.
(129) Zhao, J. B.; Zhang, F.; Guo, Y. L. *Anal. Chem.* **2019**, *91* (4), 2752−2758.
(130) Neumann, E. K.; Comi, T. J.; Rubakhin, S. S.; Sweedler, J. V. *Angew. Chem., Int. Ed.* **2019**, *58* (18), 5910−5914.
(131) Xie, Y. R.; Castro, D. C.; Bell, S. E.; Rubakhin, S. S.; Sweedler, J. V. *Anal. Chem.* **2020**, *92* (13), 9338−9347.
(132) Neumann, E. K.; Ellis, J. F.; Triplett, A. E.; Rubakhin, S. S.; Sweedler, J. V. *Anal. Chem.* **2019**, *91*, 7871−7878.
(133) Li, Q.; Tang, F.; Huo, X.; Huang, X.; Zhang, Y.; Wang, X.; Zhang, X. *Anal. Chem.* **2019**, *91* (13), 8115−8122.
(134) Niehaus, M.; Soltwisch, J.; Belov, M. E.; Dreisewerd, K. *Nat. Methods* **2019**, *16* (9), 925−931.
(135) Agüi-Gonzalez, P.; Jähne, S.; Phan, N. T. N. *J. Anal. At. Spectrom.* **2019**, *34* (7), 1355−1368.
(136) Li, H. W.; Hua, X.; Long, Y. T. *Anal. Bioanal. Chem.* **2019**, *411* (18), 4025−4030.
(137) Sheraz, S.; Tian, H.; Vickerman, J. C.; Blenkinsopp, P.; Winograd, N.; Cumpson, P. *Anal. Chem.* **2019**, *91* (14), 9058−9068.
(138) Roddy, T. P.; Cannon, D. M.; Ostrowski, S. G.; Ewing, A. G.; Winograd, N. *Anal. Chem.* **2003**, *75* (16), 4087−4094.
(139) Conlan, X. A.; Lockyer, N. P.; Vickerman, J. C. *Rapid Commun. Mass Spectrom.* **2006**, *20*, 1327−1334.
(140) Tian, H.; Sparvero, L. J.; Blenkinsopp, P.; Amoscato, A. A.; Watkins, S. C.; Bayır, H.; Kagan, V. E.; Winograd, N. *Angew. Chem., Int. Ed.* **2019**, *58*, 3156−3161.
(141) Pareek, V.; Tian, H.; Winograd, N.; Benkovic, S. J. *Science (Washington, DC, U. S.)* **2020**, *368* (6488), 283−290.
(142) Ostrowski, S. G.; Kurczy, M. E.; Roddy, T. P.; Winograd, N.; Ewing, A. G. *Anal. Chem.* **2007**, *79* (10), 3554−3560.
(143) Kleinfeld, A. M.; Kampf, J. P.; Lechene, C. *J. Am. Soc. Mass Spectrom.* **2004**, *15* (11), 1572−1580.
(144) He, C.; Hu, X.; Jung, R. S.; Weston, T. A.; Sandoval, N. P.; Tontonoz, P.; Kilburn, M. R.; Fong, L. G.; Young, S. G.; Jiang, H. *Proc. Natl. Acad. Sci. U. S. A.* **2017**, *114* (8), 2000−2005.
(145) Stryhanyuk, H.; Calabrese, F.; Kümmel, S.; Musat, F.; Richnow, H. H.; Musat, N. *Front. Microbiol.* **2018**, *9* (OCT), 1−15.
(146) Thomen, A.; Najafinobar, N.; Penen, F.; Kay, E.; Upadhyay, P. P.; Li, X.; Phan, N. T. N.; Malmberg, P.; Klarqvist, M.; Andersson, S.; Kurczy, M. E.; Ewing, A. G. *ACS Nano* **2020**, *14* (4), 4316−4325.
(147) Gorman, B. L.; Brunet, M. A.; Pham, S. N.; Kraft, M. L. *ACS Nano* **2020**, *14* (6), 6414−6419.
(148) Arandia-Gorostidi, N.; Alonso-Sáez, L.; Stryhanyuk, H.; Richnow, H. H.; Morán, X. A. G.; Musat, N. *Environ. Microbiol.* **2020**, *22*, 1381−1396.
(149) Schoffelen, N. J.; Mohr, W.; Ferdelman, T. G.; Littmann, S.; Duerschlag, J.; Zubkov, M. V.; Ploug, H.; Kuypers, M. M. M. *Sci. Rep.* **2018**, *8* (1), 1−13.
(150) Berthelot, H.; Duhamel, S.; L'Helguen, S.; Maguer, J. F.; Wang, S.; Cetinić, I.; Cassar, N. *ISME J.* **2019**, *13* (3), 651−662.
(151) Dekas, A. E.; Parada, A. E.; Mayali, X.; Fuhrman, J. A.; Wollard, J.; Weber, P. K.; Pett-Ridge, J. *Front. Microbiol.* **2019**, *10*, 2682.
(152) Jakubowski, N.; Koellensperger, G.; Theiner, S.; Loehr, K.; Mueller, L. *J. Anal. At. Spectrom.* **2020**, *35*, 1784−1813.
(153) Yu, X.; He, M.; Chen, B.; Hu, B. *Anal. Chim. Acta* **2020**, *1137*, 191−207.
(154) Löhr, K.; Traub, H.; Wanka, A. J.; Panne, U.; Jakubowski, N. *J. Anal. At. Spectrom.* **2018**, *33* (9), 1579−1587.
(155) Löhr, K.; Borovinskaya, O.; Tourniaire, G.; Panne, U.; Jakubowski, N. *Anal. Chem.* **2019**, *91* (18), 11520−11528.

https://dx.doi.org/10.1021/acs.analchem.0c04361
Anal. Chem. 2021, 93, 41−71

(156) Zheng, L. N.; Sang, Y. B.; Luo, R. P.; Wang, B.; Yi, F. T.; Wang, M.; Feng, W. Y. *J. Anal. At. Spectrom.* **2019**, *34* (5), 915−921.
(157) Pisonero, J.; Bouzas-Ramos, D.; Traub, H.; Cappella, B.; Alvarez-Llamas, C.; Richter, S.; Mayo, J. C.; Costa-Fernandez, J. M.; Bordel, N.; Jakubowski, N. *J. Anal. At. Spectrom.* **2019**, *34* (4), 655−663.
(158) Bandura, D. R.; Baranov, V. I.; Ornatsky, O. I.; Antonov, A.; Kinach, R.; Lou, X.; Pavlov, S.; Vorobiev, S.; Dick, J. E.; Tanner, S. D. *Anal. Chem.* **2009**, *81* (16), 6813−6822.
(159) López-Serrano Oliver, A.; Haase, A.; Peddinghaus, A.; Wittke, D.; Jakubowski, N.; Luch, A.; Grützkau, A.; Baumgart, S. *Anal. Chem.* **2019**, *91* (18), 11514−11519.
(160) Yao, H.; Zhao, H.; Zhao, X.; Pan, X.; Feng, J.; Xu, F.; Zhang, S.; Zhang, X. *Anal. Chem.* **2019**, *91* (15), 9777−9783.
(161) Bouzekri, A.; Esch, A.; Ornatsky, O. *FEBS Open Bio* **2019**, *9*, 1652−1669.
(162) Van Malderen, S. J. M.; Van Acker, T.; Laforce, B.; De Bruyne, M.; de Rycke, R.; Asaoka, T.; Vincze, L.; Vanhaecke, F. *Anal. Bioanal. Chem.* **2019**, *411* (19), 4849−4859.
(163) Cao, Y.; Feng, J.; Tang, L.; Yu, C.; Mo, G.; Deng, B. *Talanta* **2020**, *206*, 120174.
(164) Theiner, S.; Schweikert, A.; Van Malderen, S. J. M.; Schoeberl, A.; Neumayer, S.; Jilma, P.; Peyrl, A.; Koellensperger, G. *Anal. Chem.* **2019**, *91* (13), 8207−8212.
(165) Good, Z.; Borges, L.; Vivanco Gonzalez, N.; Sahaf, B.; Samusik, N.; Tibshirani, R.; Nolan, G. P.; Bendall, S. C. *Nat. Biotechnol.* **2019**, *37* (3), 259−266.
(166) Van Acker, T.; Buckle, T.; Van Malderen, S. J. M.; van Willigen, D. M.; van Unen, V.; van Leeuwen, F. W. B.; Vanhaecke, F. *Anal. Chim. Acta* **2019**, *1074*, 43−53.
(167) Huang, Q.; Mao, S.; Khan, M.; Lin, J. M. *Analyst* **2019**, *144* (3), 808−823.
(168) He, M.; Chen, B.; Wang, H.; Hu, B. *Appl. Spectrosc. Rev.* **2019**, *54* (3), 250−263.
(169) Dusny, C.; Grünberger, A. *Curr. Opin. Biotechnol.* **2020**, *63*, 26−33.
(170) Tavakoli, H.; Zhou, W.; Ma, L.; Perez, S.; Ibarra, A.; Xu, F.; Zhan, S.; Li, X. J. *TrAC, Trends Anal. Chem.* **2019**, *117*, 13−26.
(171) Xu, X.; Wang, J.; Wu, L.; Guo, J.; Song, Y.; Tian, T.; Wang, W.; Zhu, Z.; Yang, C. *Small* **2020**, *16* (9), 1903905.
(172) Cama, J.; Voliotis, M.; Metz, J.; Smith, A.; Iannucci, J.; Keyser, U. F.; Tsaneva-Atanasova, K.; Pagliara, S. *Lab Chip* **2020**, *20* (15), 2765−2775.
(173) Lee, B.; Jeong, S. G.; Jin, S. H.; Mishra, R.; Peter, M.; Lee, C. S.; Lee, S. S. *Lab Chip* **2020**, *20* (15), 2646−2655.
(174) Stratz, S.; Verboket, P. E.; Hasler, K.; Dittrich, P. S. *Electrophoresis* **2018**, *39* (3), 540−547.
(175) Zhang, C.; Tu, H. L.; Jia, G.; Mukhtar, T.; Taylor, V.; Rzhetsky, A.; Tay, S. *Sci. Adv.* **2019**, *5* (4), eaav7959.
(176) Fatsis-Kavalopoulos, N.; O'Callaghan, P.; Xie, B.; Hernández Vera, R.; Idevall-Hagren, O.; Kreuger, J. *Lab Chip* **2019**, *19* (6), 1071−1081.
(177) Lee, D.-H.; Li, X.; Ma, N.; Digman, M. A.; Lee, A. P. *Lab Chip* **2018**, *18* (9), 1349−1358.
(178) Lee, D. H.; Li, X.; Jiang, A.; Lee, A. P. *Biomicrofluidics* **2018**, *12*, 054104.
(179) Yun, C. K.; Hwang, J. W.; Kwak, T. J.; Chang, W. J.; Ha, S.; Han, K.; Lee, S.; Choi, Y. S. *Lab Chip* **2019**, *19* (4), 580−588.
(180) Liu, Y.; Ren, D.; Ling, X.; Liang, W.; Li, J.; You, Z.; Yalikun, Y.; Tanaka, Y. *Sensors* **2018**, *18* (11), 3672.
(181) He, C. K.; Chen, Y. W.; Wang, S. H.; Hsu, C. H. *Lab Chip* **2019**, *19* (8), 1370−1377.
(182) Chiang, Y. Y.; Teng, Y. C.; Su, Z. Y.; Hsueh, H. Y.; Tu, K. H. *Sens. Actuators, B* **2020**, *312* (March), 127966.
(183) Pei, H.; Li, L.; Wang, Y.; Sheng, R.; Wang, Y.; Xie, S.; Shui, L.; Si, H.; Tang, B. *Anal. Chem.* **2019**, *91* (17), 11078−11084.
(184) Kwon, T.; Yao, R.; Hamel, J. F. P.; Han, J. *Lab Chip* **2018**, *18* (18), 2826−2837.
(185) Babahosseini, H.; Misteli, T.; Devoe, D. L. *Lab Chip* **2019**, *19* (3), 493−502.
(186) Yu, Z.; Boehm, C. R.; Hibberd, J. M.; Abell, C.; Haseloff, J.; Burgess, S. J.; Reyna-Llorens, I. *PLoS One* **2018**, *13* (5), No. e0196810.
(187) Shen, R.; Liu, P.; Zhang, Y.; Yu, Z.; Chen, X.; Zhou, L.; Nie, B.; Zaczek, A.; Chen, J.; Liu, J. *Anal. Chem.* **2018**, *90* (7), 4478−4484.
(188) Segaliny, A. I.; Li, G.; Kong, L.; Ren, C.; Chen, X.; Wang, J. K.; Baltimore, D.; Wu, G.; Zhao, W. *Lab Chip* **2018**, *18* (24), 3733−3749.
(189) Guo, X. L.; Wei, Y.; Lou, Q.; Zhu, Y.; Fang, Q. *Anal. Chem.* **2018**, *90* (9), 5810−5817.
(190) Wu, Y.; Ren, Y.; Tao, Y.; Hou, L.; Jiang, H. *Anal. Chem.* **2018**, *90* (19), 11461−11469.
(191) Li, M.; Anand, R. K. *Chem. Sci.* **2019**, *10* (5), 1506−1513.
(192) Qin, Y.; Wu, L.; Schneider, T.; Yen, G. S.; Wang, J.; Xu, S.; Li, M.; Paguirigan, A. L.; Smith, J. L.; Radich, J. P.; Anand, R. K.; Chiu, D. T. *Angew. Chem., Int. Ed.* **2018**, *57* (35), 11378−11383.
(193) Wang, K.; Zhou, W.; Lin, Z.; Cai, F.; Li, F.; Wu, J.; Meng, L.; Niu, L.; Zheng, H. *Sens. Actuators, B* **2018**, *258*, 1174−1183.
(194) Nitta, N.; Sugimura, T.; Isozaki, A.; Mikami, H.; Hiraki, K.; Sakuma, S.; Iino, T.; Arai, F.; Endo, T.; Fujiwaki, Y.; Fukuzawa, H.; Hase, M.; Hayakawa, T.; Hiramatsu, K.; Hoshino, Y.; Inaba, M.; Ito, T.; Karakawa, H.; Kasai, Y.; Koizumi, K.; Lee, S. W.; Lei, C.; Li, M.; Maeno, T.; Matsusaka, S.; Murakami, D.; Nakagawa, A.; Oguchi, Y.; Oikawa, M.; Ota, T.; Shiba, K.; Shintaku, H.; Shirasaki, Y.; Suga, K.; Suzuki, Y.; Suzuki, N.; Tanaka, Y.; Tezuka, H.; Toyokawa, C.; Yalikun, Y.; Yamada, M.; Yamagishi, M.; Yamano, T.; Yasumoto, A.; Yatomi, Y.; Yazawa, M.; Di Carlo, D.; Hosokawa, Y.; Uemura, S.; Ozeki, Y.; Goda, K. *Cell* **2018**, *175* (1), 266−276.E13.
(195) Isozaki, A.; Mikami, H.; Hiramatsu, K.; Sakuma, S.; Kasai, Y.; Iino, T.; Yamano, T.; Yasumoto, A.; Oguchi, Y.; Suzuki, N.; Shirasaki, Y.; Endo, T.; Ito, T.; Hiraki, K.; Yamada, M.; Matsusaka, S.; Hayakawa, T.; Fukuzawa, H.; Yatomi, Y.; Arai, F.; Di Carlo, D.; Nakagawa, A.; Hoshino, Y.; Hosokawa, Y.; Uemura, S.; Sugimura, T.; Ozeki, Y.; Nitta, N.; Goda, K. *Nat. Protoc.* **2019**, *14* (8), 2370−2415.
(196) Matuła, K.; Rivello, F.; Huck, W. T. S. *Adv. Biosyst.* **2020**, *4* (1), 1900188.
(197) Xu, X.; Zhang, Q.; Song, J.; Ruan, Q.; Ruan, W.; Chen, Y.; Yang, J.; Zhang, X.; Song, Y.; Zhu, Z.; Yang, C. *Anal. Chem.* **2020**, *92* (12), 8599−8606.
(198) Kim, S. C.; Clark, I. C.; Shahi, P.; Abate, A. R. *Anal. Chem.* **2018**, *90* (2), 1273−1279.
(199) Sarma, M.; Lee, J.; Ma, S.; Li, S.; Lu, C. *Lab Chip* **2019**, *19* (7), 1247−1256.
(200) Bioč anin, M.; Bues, J.; Dainese, R.; Amstad, E.; Deplancke, B. *Lab Chip* **2019**, *19* (9), 1610−1620.
(201) Cheng, Y. H.; Chen, Y. C.; Lin, E.; Brien, R.; Jung, S.; Chen, Y. T.; Lee, W.; Hao, Z.; Sahoo, S.; Min Kang, H.; Cong, J.; Burness, M.; Nagrath, S. S.; Wicha, M.; Yoon, E. *Nat. Commun.* **2019**, *10* (1), 2163.
(202) Marie, R.; Pødenphant, M.; Koprowska, K.; Bærlocher, L.; Vulders, R. C. M.; Wilding, J.; Ashley, N.; McGowan, S. J.; Van Strijp, D.; Van Hemert, F.; Olesen, T.; Agersnap, N.; Bilenberg, B.; Sabatel, C.; Schira, J.; Kristensen, A.; Bodmer, W.; Van Der Zaag, P. J.; Mir, K. U. *Lab Chip* **2018**, *18* (13), 1891−1902.
(203) Bounab, Y.; Eyer, K.; Dixneuf, S.; Rybczynska, M.; Chauvel, C.; Mistretta, M.; Tran, T.; Aymerich, N.; Chenon, G.; Llitjos, J. F.; Venet, F.; Monneret, G.; Gillespie, I. A.; Cortez, P.; Moucadel, V.; Pachot, A.; Troesch, A.; Leissner, P.; Textoris, J.; Bibette, J.; Guyard, C.; Baudry, J.; Griffiths, A. D.; Védrine, C. *Nat. Protoc.* **2020**, *15*, 2920−2955.
(204) Gérard, A.; Woolfe, A.; Mottet, G.; Reichen, M.; Castrillon, C.; Menrath, V.; Ellouze, S.; Poitou, A.; Doineau, R.; Briseno-Roa, L.; Canales-Herrerias, P.; Mary, P.; Rose, G.; Ortega, C.; Delincé, M.; Essono, S.; Jia, B.; Iannascoli, B.; Richard-Le Goff, O.; Kumar, R.; Stewart, S. N.; Pousse, Y.; Shen, B.; Grosselin, K.; Saudemont, B.; Sautel-Caillé, A.; Godina, A.; McNamara, S.; Eyer, K.; Millot, G. A.;

https://dx.doi.org/10.1021/acs.analchem.0c04361
Anal. Chem. 2021, 93, 41−71

Baudry, J.; England, P.; Nizak, C.; Jensen, A.; Griffiths, A. D.; Bruhns, P.; Brenan, C. *Nat. Biotechnol.* **2020**, *38* (6), 715−721.
(205) Herrera, V.; Hsu, S. C. J.; Rahim, M. K.; Chen, C.; Nguyen, L.; Liu, W. F.; Haun, J. B. *Analyst* **2019**, *144* (3), 980−989.
(206) Nakao, T.; Kazoe, Y.; Mori, E.; Morikawa, K.; Fukasawa, T.; Yoshizaki, A.; Kitamori, T. *Analyst* **2019**, *144* (24), 7200−7208.
(207) Sibbitts, J.; Culbertson, C. T. *Anal. Methods* **2020**, *12*, 4665−4673.
(208) Li, X.; Soler, M.; Szydzik, C.; Khoshmanesh, K.; Schmidt, J.; Coukos, G.; Mitchell, A.; Altug, H. *Small* **2018**, *14* (26), 1800698.
(209) Sun, D.; Cao, F.; Xu, W.; Chen, Q.; Shi, W.; Xu, S. *Anal. Chem.* **2019**, *91* (3), 2551−2558.
(210) Sun, D.; Cao, F.; Cong, L.; Xu, W.; Chen, Q.; Shi, W.; Xu, S. *Lab Chip* **2019**, *19* (2), 335−342.
(211) Zhang, Y.; Wang, Z.; Wu, L.; Zong, S.; Yun, B.; Cui, Y. *Small* **2018**, *14* (20), 1704433.
(212) Huang, Q.; Mao, S.; Khan, M.; Li, W.; Zhang, Q.; Lin, J. M. *Chem. Sci.* **2020**, *11* (1), 253−256.
(213) Zhou, Y.; Chen, Z.; Zeng, J.; Zhang, J.; Yu, D.; Zhang, B.; Yan, X.; Yang, L.; Wang, Q. *Anal. Chem.* **2020**, *92* (7), 5286−5293.

https://dx.doi.org/10.1021/acs.analchem.0c04361
Anal. Chem. 2021, 93, 41−71